Micro-electromechanical Structural Design and Optimization of Vertical Cavity Photonic Devices with Wide Continuous Tuning

genehmigte Dissertation zur Erlangung des akademischen Grades eines

Doktor der Ingenieurwissenschaften (Dr.-Ing.)
im Fachbereich Elektrotechnik/Informatik
der Universität Kassel

vorgelegt von

Dipl.-Ing. Edwin Omondi Ataro, B.Tech., M.Sc.(Elec. Eng.)

Kassel, im Februar 2005

Betreuer: Prof. Dr. Hartmut Hillmer

Prüfungskommission   Prof. Dr. Hartmut Hillmer   (1. Gutachter)
                      Prof. Dr. Wolf-Jürgen Becker   (2. Gutachter)
                      Prof. Dr. Jürgen Schmid   (Beisitzer)
                      Prof. Dr. Albert Zündorf   (Beisitzer)

Tag der mündlichen Prüfung: 21.02.2005

DOCTORAL DISSERTATION

Edwin Ataro

Micro-electromechanical Structural Design and Optimization of Vertical Cavity Photonic Devices with Wide Continuous Tuning

Kassel, 2005

UNIKASSEL
VERSITÄT

Table of Contents

List of Figures

List of Tables

Acknowledgements

My heartfelt gratitude goes to my advisor and supervisor Prof. Dr. Hillmer for offering me the chance to carry out this work in his research group, for the kind material and moral support that extended well beyond just academic endeavours and pursuits, for his keen interest in my progress and welfare, and for being such an inspiration and a great reservoir of prolific ideas and valuable tips. The great confidence he bestowed in me kept me going at all times.

I owe many thanks to Dr. Conny Prott, in whose team I worked for almost the entire duration of my stay in Kassel, for her help, patience and tolerance.

This work would not have been what it is without the collaboration, cooperation and many useful inputs from my colleagues Amer Tarraf, Sören Irmer, Friedhard Römer, Dietmar Gutermuth and Ina Wensch as well as Dr. Jürgen Daleiden. I deeply respect and admire their vast experience, expertise and unique abilities. As for Ina and Dietmar, I keep wondering: Weren't we siblings in a previous lifetime? The help I got from Heike Schröter-Hohmann and Ina Kommalein is also deeply appreciated.

Prof. Dr. Kassing and all the other members of the institute (IMA) provided a wonderful working atmosphere. Thank you all.

I am deeply indebted to my friend Dr. Edward Wasige and to Prof. Dr. Kompa. Their initiatives and efforts landed me at the University of Kassel.

My sincere appreciations go to my friends Dr. George Kamucha, Ochieng' Abuya and Tobias Odhiambo for their subtle, but priceless contributions.

My family was, as always, my greatest pillar of strength. Many special thanks to my wife Loise, for her steadfast support, encouragement and the endless endurance. My lovely daughters Valentine and Sandra probably kept wondering why some grown-ups also have to be in school. The puzzle will, hopefully, fall into place some day. Just the thought of them fired up the determination. My father and ailing mother tried their best to cheer me on and to shield me from their suffering. May Providence pay back.

The funding from the German research foundation, DFG and the ministry of education

and research, BMBF is gratefully acknowledged. Finally, all the contributions from the many not named above is not forgotten, but greatly appreciated.

E. O. Ataro

Kassel, February 2005

Abstract

This dissertation covers the design and optimisation aspects of microelectromechanical tunable vertical cavity devices using the finite element method (FEM). The main emphasis of the work was on the electromechanical structural design and optimisation of multiple air-gap tunable DBR-based vertical cavity photonic devices with wide continuous tuning. A multi-membrane InP/air Fabry-Pérot optical filter is presented and comprehensively analysed. In this work, a systematic structural design procedure which provides clear guidelines in the design process is proposed. An accurate analytical electromechanical model for the devices has been derived. This can be an invaluable tool in providing a quick insight at beginning of design phase. With the use of the FEM program, the effect of the non-linear stress stiffening has been widely investigated and its effect on the extension of the mechanical travel range of the device actuation demonstrated. It was also interesting to deduce from the calculations that regardless of the device structural configuration, normalised deflection-voltage characteristic profile remains invariable. The distortion of the actuated membrane is known to have often severe consequences on the performance of MOEMS devices. This work shows how the choice of structural design dimensions affect the membrane distortion. One difficulty encountered in the FEM mathematical model calculations of these devices with 3D models is the huge demand on the computing resources where 3D models are concerned. In this work a very accurate 2D software method based on the FEMLAB software that is faster and requires much less computing resources was implemented. This tool has been applied in the design and design optimisation of various features of the investigated devices. Further, it has been used in investigating the effects of scaling of the tunable devices. In a situation where a desire exists to tailor-scale a device such that the resulting device replicates the tuning characteristics of the original, it is hereby demonstrated that this can be achieved in a simple, predictable and reliable way. For calculations that could not be carried out with the 2D approximation software tool, the standard FEM setups built into FEMLAB were applied. Calculations involving micromachined structures with in-plane residual stress that results in changed rigidity and

out-of-plane deformations required a modification of the standard methods to incorporate stress. This enabled the exploration of the nature and effect of residual biaxial and gradient stress in the devices and a more accurate prediction of the tuning behaviour of devices with residual stress as seen when compared with measurements.

Deutsche Zusammenfassung

Das Hauptziel dieser Arbeit war, das elektromechanische Design und die Designoptimierung von durchstimmbaren optischen multimembranbasierten Bauelementen, mit vertikal orientierten Kavitäten basierend auf der Finite Element Methode (FEM), mit folgenden Zielen durchzuführen:

- Die Bauelemente genau zu charakterisieren, um einen tieferen Einblick in ihr elektromechanisches Verhalten zu erhalten. Im Vordergrund stand dabei die Ermittlung des Einflusses der verschiedenen strukturellen Konfigurationen auf das Durchstimmungsverhalten.

- Den Einfluss der axialen und gradienten Verspannung auf das Durchstimmungsverhalten zu untersuchen und quantitativ zu bestimmen, sowie die Genauigkeit der theoretischen Modelle mit Hilfe der experimentellen Messungen zu überprüfen.

- Den Effekt des sog. "Down-scaling" auf die dynamischen Eigenschaften der Bauelemente zu untersuchen, um damit Informationen über die Vor- und Nachteile der Skalierung zu erhalten.

Zu diesen Kernthemen werden im Rahmen der vorliegenden Dissertation neue und sehr nützliche Ergebnisse präsentiert. Zahlreiche elektromechanische Modelle sind in der bisher erschienenen Literatur zu finden. Unter Berücksichtigung der nicht-linearen Kraftkopplung und der Deformation eignen sich diese Modelle jedoch meistens nur für einfache regelmäßige Geometrien wie Balken und quadratische oder kreisförmige Membrane. Die Berechnung für beliebige komplexe Strukturen würde damit sehr aufwendig bis nahezu unmöglich sein. Die Methoden, die in dieser Arbeit vorgeschlagen und verwendet werden, sind jedoch durchaus auch für derartige Geometrien geeignet. Die FEM ist ein relativ altes numerisches Analysewerkzeug, das allerdings bisher häufig wegen seinem enormen Bedarf an Computerressourcen besonders für Berechnungen, die viele Freiheitsgrade

erfordern, gemieden wurde. Aufgrund der rasanten Steigerung der Verarbeitungsperformance gewöhnlicher Tischrechner in den letzten Jahren, sind diese Betrachtungen jedoch nach und nach irrelevant geworden. Die Finitelemente Modellierungssoftware stellt im Moment eine attraktive und dabei vergleichsweise ökonomische Wahl für die hier beschriebene Art der Arbeit dar. Außerdem kann die Anwendung der innovativen Problemvereinfachungen das Ressourcennachfrageproblem[1] weiter vermindern. Ein solcher Fall wird in Kapitel 3 erläutert. Das dort dargestellte elektromechanische quasi-3D Modell kann allgemein für die Modellierung dünner Strukturen angewendet werden, indem man diese als 2D-Objekte betrachtet und die dritte Dimension eine konstante Größe (z.B. die Schichtdicke) oder eine Größe, welche eine mathematische Funktion der 1. und 2. Raumrichtung oder der Zeit, usw. ist. Diese Annahme verringert drastisch die Berechnungszeit sowie den erforderlichen Arbeitsspeicherbedarf. Die Ergebnisse der quasi-3D Methode stimmte exakt mit den Ergebnissen der Standardvergleichtests überein. Zusätzlich wird in Anhang C ein Nachweis zur Genauigkeit der Annahmen für die in dieser Arbeit benutzten Ableitung der elektromechanischen Koppelung gegeben. Der Vergleich der Resultate von einem vollständig gekoppelten, selbstkonsistenten, elektrostatisch-mechanischen Modell und dem in dieser Arbeit dargestellten Modell liefert einen Unterschied von weniger als 1%.

Die analytischen "closed-form"-Modelle (abgeleitet von den FEM-Berechnungen) führten sogar schneller zum Ergebnis und waren dabei sehr genau, weil sie nur als einfache mathematische Formeln eingeführt werden mussten und dabei das FEM Berechnungsverfahren (d.h. geometrische Strukturdefinition, "Mesh"-erzeugung und Berechnung) nicht benötigt wird. Solche Modelle sind nützlich um schnell einen klaren Einblick, sowohl in der Designanfangsphase, als auch in einigen Fällen im Verlauf des gesamten Designprozesses zu erhalten. Diese Dissertation stellt auch ein systematisches Designverfahren für die Ermittlung der Strukturmaße vor, die auf gegebenen Spezifikationen basieren. Das Verfahren hilft einige Grenzwerte, z.B. Mindestmembranedurchmesser und Länge der Verbindungsbrücken, zu definieren, die auf stichhaltigen, physikalischen und technologischen Betrachtungen basieren und ermöglicht dem Bauelementdesigner, das Design zum ersten Mal mit sehr hoher Genauigkeit durchzuführen und dadurch unerwünschte und unnötige Versuchszyklen zu vermeiden.

---

[1]Die Größe des Arbeitsspeichers sowie die Prozessorgeschwindigkeit spielen eine entscheidende Rolle in FEM. Selbst kleinere Problemstellungen erfordern u.U. Arbeitsspeicher in der Größenordnung von 1 Gigabyte und ein schnellen Prozessor.

Mit den oben erwähnten Methoden und Modellen wurden einige Designoptimierungsstudien durchgeführt, deren Resultate weitreichende und nützliche Erkenntnisse erbringen. Zuerst wurden Durchstimmungseigenschaften, d.h. die mechanische Ablenkung in Abhängigkeit von der Spannung für verschiedene strukturelle Konfigurationen und geometrische Maße im Bereich zwischen dem spannungslosen Zustand und dem "Pull-in" Punkt ermittelt, die anschließende Normierung der Durchstimmungskurven im Bezug auf ihre korrespondirende Pull-in-Ablenkung und -Spannung zeigte, dass alle resultierenden Kurven praktisch identisch sind. Das heißt, das die normierte Relation zwischen Ablenkung und Spannung ein unveränderliches Profil hat. Daraus ergibt sich, dass die elektromechanische Durchstimmung für jede mögliche Struktur, innerhalb einer gegebenen Kategorie von Bauelementen, ausreichend durch die Pull-in-Ablenkung und -Spannung definiert wird. Dieses trägt dazu bei, die Designarbeit und -analyse erheblich zu vereinfachen.

Die zweite Beobachtung, war, dass die mit Hilfe der FEM errechnete mechanische Durchstimmungsstrecke, mehr als ein Drittel der Kavitätslänge beträgt. Dieses Wert wird in der Literatur allgemein angetroffen und ist das Ergebnis der einfachen analytischen Berechnungen. Es zeigte sich, dass der Betrag der Änderung von der Strukturgeometrie abhängt und dem durch die Verspannung hervorgerufenen versteifenden Effekt zugeschrieben wird. Die Strukturen mit größerer Versteifung ermöglichen eine stärkere Auslenkung der Membran. Der Gewinn beträgt bis zu mehr als 30% gegenüber dem Ergebnis der einfachen Analyseverfahren. Dieses Wissen kann für das genauere Systemdesign genutzt werden.

Die Deformation der Membranflächen, der in dieser Arbeit dargestellten Bauelementformen, ist ein unerwünschter, jedoch manchmal unvermeidbarer Effekt. Es zeigt sich aber, dass die Wahl der Größe der Membran im Verhältnis zur Länge der Verbindungsbrücken und die Wahl der strukturellen Konfigurationen (2, 3 oder 4 Verbindungsbrücken) den Grad der Membrandeformation, im Falle der Aktuation beeinflusst. Für die korrekte optische Wirkungsweise der Bauelemente ist in der Regel die Beibehaltung einer optisch ebenen Oberfläche sehr wichtig, es sei denn, gekrümmte Oberflächen sind ausdrücklich erwünscht.

Die Einbeziehung des Einflusses von axialen Verspannungen und Gradientenverspannungen in die Berechnungen erforderte die Änderung der Standardimplementierung des 3D Mechanikberechnungsmodus, der mit der benutzten FEM Software geliefert wurde. Weil diese Verspannung eine verhältnismäßig große Dehnung verursacht, konnten genauere Resultate erreicht werden, indem ein großes Deformationsmodell verwendet wur-

de, bei dem die Dehnungen nach Green-Lagrange Art - anstatt normaler elastischer Verformungen - betrachtet werden. Die Genauigkeit des Modells wurde mit einfachen Balkenmodellen validiert und die Resultate mit Literaturwerten verglichen. Dabei basieren die Literaturwerte auf verschiedenen Simulationsmethoden. Die Ergebnisse dieser Studie zeigten einen großen Einfluss der Verspannung auf die Durchstimmungseigenschaften der untersuchten Bauelemente. Ferner stimmte die Ergebnisse der theoretischen Modellrechnung mit den experimentellen Resultaten sehr gut überein. Ein Beispiel solch eines Vergleichs wird am Ende von Kapitel 4 gegeben.

Die Skalierungsuntersuchungen bilden den letzten Teil der Schlüsselergebnisse dieser Arbeit. Das Ziel war es, eine Methode zu entwickeln, die es erlaubt ein skaliertes Bauelement zu studieren, das die gleichen mechanischen Durchstimmungsverhalten wie die Vorlage hat, um damit den Einfluss der Skalierung z.B. auf die Stabilität des Bauelements zu untersuchen. Eine neuartige Skalierungstechnik wurde abgeleitet und verwendet. Die Ergebnisse belegen, dass das daraus resultierende, skalierte Bauelement fast genau die gleiche mechanische Durchstimmung wie das unskalierte zeigt. Die Vorteile des "Downscaling" drücken sich jedoch in verbesserter Schaltungsgeschwindigkeit und Stabilität aus. Die Verbesserung der Stabilität wurden anhand der Änderungen in den Eigenfrequenzen, der Übergangsfunktion und der Impulsantwort auf einen mechanischen Stoß beurteilt. Es ist zur Zeit leider noch schwierig herunterskalierte Bauelemente mit Membrandicken in dem sub-100nm Bereich zu realisieren. Die Lösung dieses Problems ist Gegenstand jedoch der aktuellen Forschung. Sobald dieses zuverlässig und kosteneffektiv gelingt, ist es an der Zeit, die Vorteile des "Down-scaling", wie höhere Produktionsrate von mehr Bauelementen pro Produktionsdurchlauf sowie stabileren Bauelementen mit längeren Lebenszeiten aufgrund geringer Materiellenermüdung, usw., produktiv zu nutzen.

Chapter 1

Introduction

1.1 The bandwidth challenge in telecom networks

Many of the telecommunication networks existing today were designed using models that assumed that an individual needed to use a telecom channel for just a few minutes per hour at the most. These models did not take into account the amount of traffic generated by the internet, fax, voice, video, cable TV (CATV) and data transmission that did not exist then. The bandwidth capacity required now to satisfy consumer needs is enormous, and still rising. Appendix A contains information on the current estimates of internet usage statistics in the world in general and in Kenya and Germany in particular [1]. The population penetration rates are an indication that the untapped potential demand is staggering. The average user growth rate is more than 125% with some regions registering well over 200% in the last four years.

The fibre optic telecom technology offers virtually unlimited bandwidth potential and is widely considered as the ultimate solution to deliver all forms of broadband access including the so called last mile which is at the moment still dominated by the twisted pair copper wire (TPW). The first fibre optic telecom system was installed in 1977 by AT&T and GTE (now Verizon Communications). From that time on, optical fibres have steadily overtaken the TPW especially in undersea, long-haul networks (hundreds to thousands of kilometres) and metropolitan area networks (MANs) (tens to hundreds of kilometres). Local optical access networks such as Fibre-to-the-home (FTTH) are in comparison still in their early deployment stages [2, 3, 4, 5, 6].

As a result of the explosive growth in bandwidth demand, telecom carriers and service providers are faced with capacity exhaustion in the fibre networks. Another challenge for

carriers is the integration of diverse information formats in just one physical infrastructure at competitive costs. Usually email, video and multimedia information is carried as Internet protocol (IP), data over asynchronous transfer mode (ATM) and voice over synchronous optical network (SONET) used in North America or synchronous digital hierarchy (SDH) in international networks.

Three solutions can be proposed to resolve this capacity crisis [6, 7, 8];

- to install new optical fibres - an expensive option that will not necessarily solve the integration problem,

- to use smaller time slots in the time division multiplexing (TDM) process e.g. instead of using the OC-192 standard (10 Gbit/s) use OC-768 (40 Gbit/s). This solution calls for more expensive higher frequency devices and components,

- to use dense wavelength division multiplexing (DWDM). This technique assigns incoming optical signals to specific wavelengths ("colours") within a designated bandwidth followed by simultaneous transmission of the resulting signals through one optical fibre. "Dense" refers to the ability to support 8 or more wavelengths within a single band. DWDM enables the expansion of existing network capacity 80 times or more [7, 9]. To better visualise how this technique works, consider a highway where a lane is analogous to an optical DWDM channel. In the absence of DWDM, only one lane is used and more capacity is obtained by moving faster. With DWDM technique, many lanes are opened, which opens a new capacity dimension in terms of wavelength. In addition different kinds of vehicles, analogous to different formats (IP, ATM, SONET/SDH, etc) are allowed. The great advantages of DWDM are that it is a high performance technique that allows a much more efficient use the existing fibre network capacity, is protocol transparent, easy to install, functionally simple, robust, has high flexibility in network planning and is highly scalable. The mind-boggling potential of DWDM has already severally been demonstrated. Bell Labs reported 2.56 Tbit/s (64 channels x 40Gbit/s) over 4000km [10], Alcatel and NEC have reported 10.2 Tbit/s (256 channels x 42.7Gbit/s) over 100km [11] and 10.92 Tbit/ (273 channels x 40Gbit/s) over 115km [12], respectively. This kind of transmission implies a total throughput in one optical fibre of about 80 million simultaneous two-way telephone calls! In the latest developments the Deutsche Telekom and France Telecom working under the umbrella of the TOPRATE (Terabit/s Optical Transmission Systems based on Ultra-high Channel Bitrate) project have reported successfully transmitting 8 channels x 170GBit/s

over 430 km of standard single-mode optical fibre [13]. Even more promising is the fact that the bandwidth in just the 1.5μm band of each of the existing single-mode fibres is over 25THz [4].

1.2 The optical network and components

The ultimate goal in photonics is to take the optical technology to the edges of the networks - to individual homes and desktops and even further to the inside of the fastest processor systems [2, 4]. The now ordinary desktop computers with 3 GHz clock speeds and 32 bit data-bus have the potential capacity for data transfer at 96 Gbit/s. These are connected to the fast backbone network through the "fast" links such as asymmetric digital subscriber lines (ADSL) and other techniques operating in the low Mbit/s range at best. DWDM is therefore just the first step on the road to full optical networking. A major bottleneck in achieving this goal has been the non-availability of versatile cost-effective, high performance optical devices and components such as optical filters, tunable lasers - which is the photonic equivalent of a frequency synthesizer in electronics, optical converters, optical amplifiers, etc. Optical filters are found in optical multiplexers (MUX) and demultiplexers (DEMUX), optical add/drop multiplexers (OADM), WDM couplers and band splitters [14, 15]. They are also employed in gain equalisation and dispersion compensation [16, 17]. The emergence of fully optical network components such as reconfigurable optical add/drop multiplexers (ROADM) [6] and optical cross connectors (OXC) [18] will enable the elimination of optical-electrical-optical (OEO) conversion leading to dynamic wavelength provisioning in reconfigurable transparent optical networks offering more flexibility, robustness and higher capacity. Transparent here implies the absence of OEO conversion. The diagram of Fig. 1.1 is a simplified schematic of a DWDM network. Optical filters are applied in practically all of the components shown. The optical filter is therefore one of the key devices in the control of light in photonics technology. The microelectromechanical system (MEMS) technology has emerged as one of the technologies of choice in the fabrication of high performance optical filters in use today and for a promising future [5, 19, 20]. In general, dynamic MEMS-based optical components are now considered the panacea for achieving enhanced operational efficiency and economy in advanced optical networks, as well as in high volume production [14].
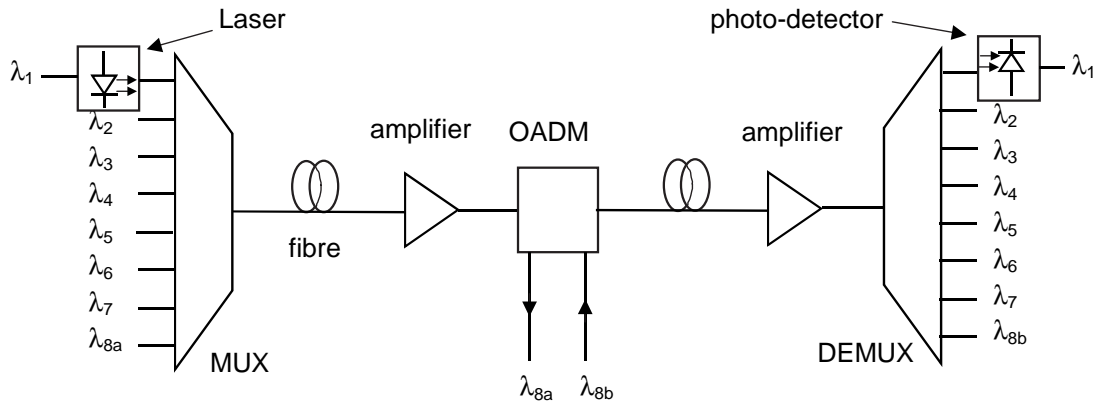
Fig. 1.1: Simplified schematic of a DWDM network. Optical filters are applied in practically all the components shown. Electrical signal is converted to optical signal by the laser and vice versa by the photo-detector.

1.3 MEMS tunable optical filters

MEMS tunable filters are a key solution in providing agile functionality in optical systems [21]. MEMS devices have the inherent advantages of speed, reliability, small size and low power consumption. Besides, when actuation is involved, the deflections are small hence relatively less material fatigue exists and longer lifetimes are possible[14]. Micromachined MEMS filters have unique attributes that meet the stringent requirements in optical communication systems. These attributes include; environmental stability, thermal stability, superior optical properties (low insertion loss, wide and flat bandpass, steep slopes, good isolation, small chromatic dispersion, small polarisation dependent loss, high rejection ratio), modularity and scalability. In addition they work in either transmission or reflection modes, realising either bandpass or band-reject functions and also offer tunability [14, 17].

Perhaps the most promising design for many micromachined MEMS tunable devices is the vertical cavity configuration. A vertical cavity device consists of an optical cavity sandwiched between two reflectors. Within a finite spectral stop-band width or finite spectral gain profile, a given cavity length supports, preferentially, a single Fabry-Pérot (FP) optical mode. Changing the cavity length by varying the position of the reflectors relative to each other enables the tuning action. Apart from vertical cavity optical filters [22, 23, 24, 25, 26, 27], this has been applied in vertical cavity surface emitting lasers (VCSEL) [28, 29, 30, 31, 32], vertical cavity semiconductor optical amplifiers (VCSOA) [33, 34, 35], vertical cavity optical detectors (VCOD) [35, 36], resonant (vertical) cavity

light emitting diodes (RCLED) [37, 38, 39], and vertical cavity modulators [40] among others. The enabling fabrication technology here is surface micromachining. Some of the major advantages of surface micromachined vertical cavity device technology are; possibility to produce large 2D arrays of devices in single runs thereby drastically reducing cost per device, on-wafer testing is possible eliminating the need for cleaving which results in added costs and risk of reduction in yield, easier packaging, higher coupling efficiency of the devices to optical fibre, the light emitting devices have circular beams that are better for coupling and for very short cavities they tend to be inherently single mode.

Although the surface micromachining technology is mature to a large extend, a few challenges still remain to be tackled. One of this is the precise control of the device dimensions. The layer fabrication processes such as molecular beam epitaxy (MBE) and chemical vapour deposition (CVD) produce very precise thicknesses. However, minute variations in dimensions in the order of nanometres can render a whole production run useless for the intended purposes. These can also result from the etching processes used. Various techniques have been applied to solve this kind of problem [41].

The second major challenge is the production of environmentally stable high purity layers devoid of contaminants that cause residual stress, increase scattering loss and absorption resulting in high insertion loss and out-of-plane deformations that often adversely influence the device behaviour. The influence of residual stress on the electromechanical tuning characteristics of vertical cavity MEMS tunable structures constitutes a major part of this work.

Besides the FP filter described above, other top optical filtration technologies are the array waveguide grating (AWG) [42] and the fibre Bragg grating (FBG) [43, 44]. Others are the tilt interference filter (TIF) [45], the linear variable filter (LVF) [46], the Mach-Zehnder interferometer (MZI) [47] and the diffraction grating (DG) [48]. Recently introduced technologies include ladder-type structure [49], ferro-fluid-based filter [50], apodised sampled grating (ASG) [51] and tunable FP polymer filters [52]. An interesting InP-based horizontal design with a potentially very wide tunability has recently been proposed [53]. It remains to be seen if this will be realised with the current state of the art in micromachining technology. Table 1.1 is a summarised comparison of important filter characteristics for the various technologies [21, 54].

Technology ⤳	FP	TIF	LVF	FBG	MZI	DG
Insertion loss	good	modest	modest	excellent	high	high
Flat-top	no	close	yes	yes	close	close
Rejection	poor	modest	good	modest	poor	good
Low chrom. dispersion	poor	modest	good	poor	modest	good
Size	good	modest	good	modest	good	poor
Speed	good	modest	poor	poor	excellent	modest
Multiport rejection	modest	modest	modest	good	good	good
price	modest	low	modest	high	modest	modest

Table 1.1: Qualitative comparison of important filter characteristics of various optical filter technologies [21].

1.4 Other possible applications

The range of possible application of vertical cavity devices extends well beyond optical communications. It is by no means intended here to give an exhaustive list of all the possible areas of application, but just to highlight a few.

Some of the major areas of application of the filters are in spectral photometry, medical diagnostics, chemical analysis, calorimetry and astronomy. In photometry they can be applied in separating light into the respective primary colours for further processing. Blood chemistry analysis is a possibility in medical diagnostics. In chemical analysis they can be used for fluorescent microscopy, liquid chromatography and gas monitoring. Finally in astronomy, they can be used to filter out chosen bands of light in search of particular elements [16, 50].

The filter design of a vertical resonant cavity sandwiched between two reflectors is itself used in realising the other vertical cavity devices. The additional feature in the other devices is the inclusion of some opto-active material in the cavity. These other devices in themselves embody a host of applications.

1.5 The aims and scope of this work

The main aim of this work was to carry out the electromechanical design and design optimisation of tunable multi-membrane vertical cavity optical filter structures, such as shown in Fig. 1.2, using finite element analysis (FEA) with the following goals:

- to accurately characterise the devices in order to provide a deeper insight into their
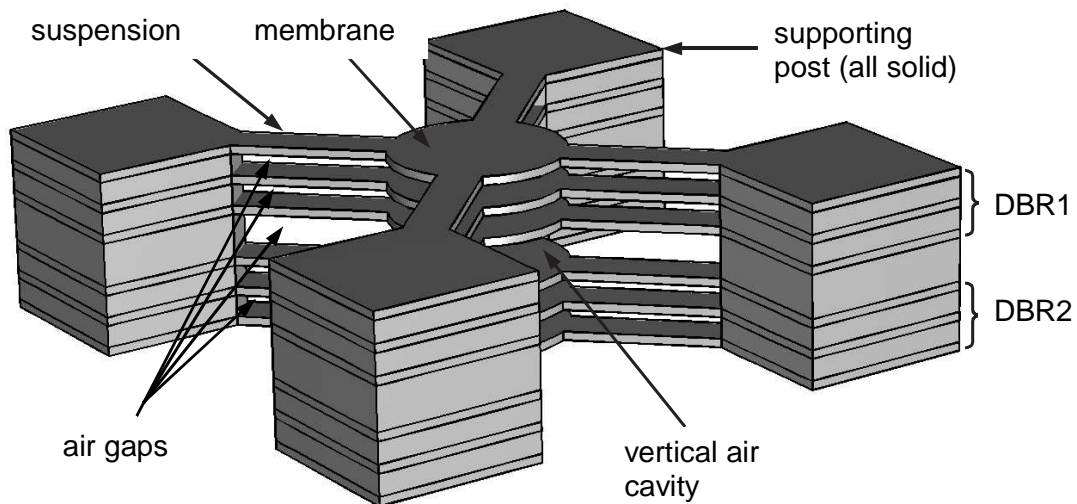
Fig. 1.2: Structural set-up of a tunable multi-membrane vertical air cavity optical filter structure showing circular membranes supported by 4 suspensions each. The suspensions are in turn mounted on supporting posts. The air cavity is situated between two distributed Bragg reflectors (DBRs). Note: vertical dimensions are exaggerated for clarity.

electromechanical behaviour, especially the effect of various dimensional configurations on the device tuning.

- to investigate and quantify the influence of residual axial and gradient stress on device tuning and to verify the accuracy of the theoretical models with experimental measurements.

- to investigate the effect of down-scaling on the dynamic characteristics of the devices in order to glean some information on advantages/disadvantages accruing from scaling.

Chapter 2 presents the fundamental principles of the filter function. Numerous simple models generated from Matlab^{TM} programs and finite element analysis are used to explain the principle of operation of the filter device.

In chapter 3, both the 2D and 3D electrostatics-mechanics coupled models developed for the analyses are presented. This is followed by the development of analytical closed-form expressions for membrane stiffness derived from FEA computations. The models constructed from the closed-form expressions show extremely good agreement with the FEA calculations. Detailed step by step structural design guidelines are presented followed by an illustrative design example. Finally, the chapter closes with results of an

analysis of the effect of variation of geometrical dimensions on tuning and pull-in point of various configurations of the tunable filter structures.

Chapter 4 opens with an explanation of the nature of residual axial and gradient stress as well as the sources thereof. Both the 3D and analytical models of chapter 3 are accordingly modified to include the effect of residual stress. These are then used to determine the influence of the stress on the out-of-plane deformation of the unactuated structures as well as on the electromechanical tuning behaviour. Comparison of model output with experimental measurements are presented showing very good agreement.

A derived tailored scaling technique is presented in chapter 5 with which an electrostatically tunable membrane device can be down-scaled (or up-scaled if so desired) in such a way that the resulting device exactly replicates the mechanical tuning characteristic of the original. Comparison is made of the device transient response to a step actuation voltage input before and after down-scaling. A second comparison examines the response to a mechanical shock impulse. The results reveal huge gains made on the device performance stability and dynamic response by down-scaling.

Finally, chapter 6 concludes this work with a concise summary and a few suggestions for future work in this field.

Chapter 2

Essential theoretical fundamentals

2.1 Theory of Fabry-Pérot filter with distributed Bragg reflectors

An electrical resonator such as a parallel inductor-capacitor circuit allows an electrical oscillation only at the resonant frequency f_0 determined by the values of the components within a narrow bandwidth around f_0. Such a circuit stores energy at this frequency and also acts as a filter at the same frequency.

An optical resonator is the optical counterpart, storing energy or filtering optical waves only at certain frequencies and wavelengths. The Fabry-Pérot etalon can be used as an optical resonator or filter [55, 56, 57].

2.1.1 The Fabry-Pérot etalon

A Fabry-Pérot etalon [58] is an optical interferometer in which an optical beam undergoes multiple reflections between two flat parallel reflecting surfaces and whose resulting optical transmission (or reflection) is periodic in frequency. The simplest etalons are uncoated plane-parallel solid material where the optical transmission or reflection are completely determined by the length L between the parallel surfaces and the refractive index n of the material. This is the solid etalon. Then there is the air-gap etalon formed by two surfaces with the cavity formed by an air-filled space between the surfaces. In the following analysis it is shown that the etalon can be both a resonator and a reflector at a given frequency depending on the cavity length. The combination of both the resonator and the reflecting function by appropriately stacking several etalons results in the distributed Bragg reflector
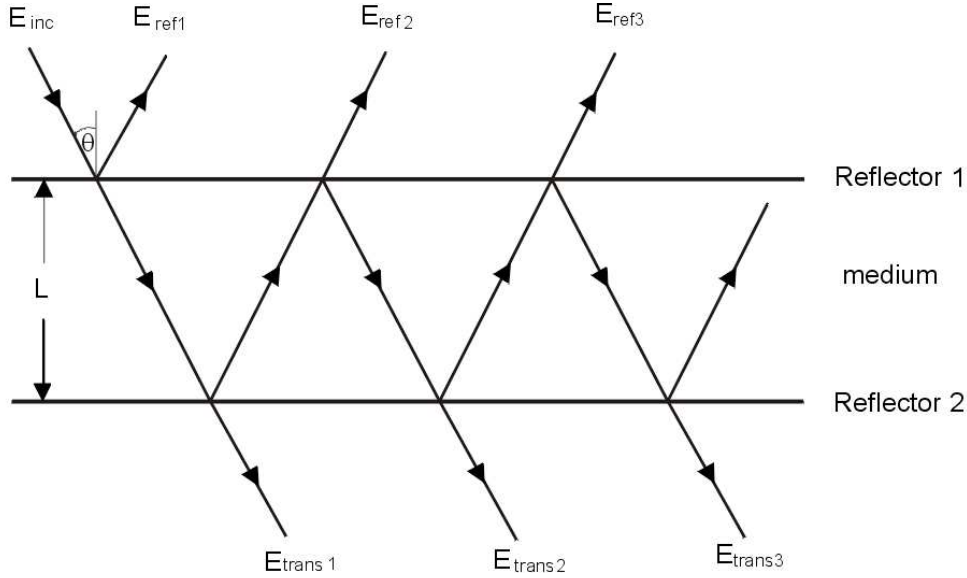
Fig. 2.1: Schematic of a Fabry-Pérot etalon depicted by two parallel reflectors with a medium of refractive index *n* in between. An electromagnetic wave is incident at the first reflector surface at an angle θ.

(DBR) filter, the key subject of this thesis. In Fig. 2.1 is a Fabry-Pérot etalon with two flat parallel reflectors with power reflection coefficients given by R_1 and R_2 , and power transmission coefficients by T_1 and T_2, respectively. The losses caused by scattering on the reflector surfaces and by absorption in the reflector material are represented by A_1 and A_2, respectively. Scattering means that the energy from a propagating electromagnetic wave is redirected as secondary waves in various directions away from the original direction while absorption is the loss in the power in the wave due to conversion to other forms of energy e.g. structural vibrations and excitation of electrons to higher energy levels. From the law of conservation of energy, $R_1 + T_1 + A_1 = 1$ and similarly for the second reflector.

If the electric field of the incident electromagnetic wave has an amplitude E_{inc}, the amplitude of the reflected wave from the first interface is E_{ref1}, while the partially transmitted amplitude of the second interface is E_{trans1}. The multiple transmitted waves differ in phase due to the optical path lengths traversed by each wave. The optical phase acquired by the monochromatic plane wave with a free space wavelength λ and frequency f on one round trip through the etalon is given by

$$2\hat{\delta} = 2\frac{2\pi f}{c_0} nL cos\theta \tag{2.1}$$

The angle θ is the angle of incidence of the wave on the etalon surface. It is shown

grossly exaggerated in Fig. 2.1, but assumed to be very small ($\theta \approx 0°$) for the analysis. Taking the complex reflection and transmission coefficients of the wave as r_1, r_2 and t_1, t_2, respectively, (where $R_1 = |r_1^2|$ and $T_1 = |t_1^2|$), α as the absorption coefficient of the wave field amplitude as it propagates through the material, the amplitude of the first transmitted wave is

$$E_{trans1} = t_1 t_2 e^{-\alpha L} e^{-j\hat{\delta}} E_{inc} \tag{2.2}$$

The remaining part of the wave is reflected back and forth in the cavity, with each reflection, the wave is partially coupled out of the resonator. The transmitted output of the m*th* round-trip is given by

$$E_{trans\,m} = t_1 t_2 e^{-\alpha L} e^{-j\hat{\delta}} (r_1 r_2)^m e^{-2m\alpha L} e^{-j2m\hat{\delta}} E_{inc} \qquad m = 0, 1, ..., \infty \tag{2.3}$$

The total transmitted field results from the superposition of all the transmitted parts i.e.

$$E_{trans} = t_1 t_2 e^{-\alpha L} e^{-j\hat{\delta}} E_{inc} \sum_{m=0}^{\infty} (r_1 r_2 e^{-2\alpha L} e^{-j2\hat{\delta}})^m \tag{2.4}$$

which simplifies to

$$\frac{E_{trans}}{E_{inc}} = t_1 t_2 e^{-\alpha L} e^{-j\hat{\delta}} \frac{1}{1 - \left(r_1 r_2 e^{-2\alpha L} e^{-j2\hat{\delta}} \right)} \tag{2.5}$$

The total device power transmission coefficient T_{tot} is given by

$$T_{tot} = \frac{E_{trans} E_{trans}^*}{E_{inc} E_{inc}^*} = \frac{(1 - R_1 - A_1)(1 - R_2 - A_2)e^{-2\alpha L}}{(1 - \sqrt{R_1 R_2} e^{-2\alpha L})^2} \frac{1}{1 + \frac{4\sqrt{R_1 R_2} e^{-2\alpha L}}{(1 - \sqrt{R_1 R_2} e^{-2\alpha L})^2} sin^2 \hat{\delta}} \tag{2.6}$$

Using a similar analysis for the reflection properties, the total device power reflection coefficient can be shown to be

$$R_{tot} = \frac{(\sqrt{R_1} - \sqrt{R_2}.(1 - A_1)e^{-2\alpha L})^2 + 4\sqrt{R_1 R_2}(1 - A_1)e^{-2\alpha L} sin^2 \hat{\delta}}{\left(1 - \sqrt{R_1 R_2} e^{-2\alpha L} \right)^2 + 4\sqrt{R_1 R_2} e^{-2\alpha L} sin^2 \hat{\delta}} \tag{2.7}$$

A simple program was implemented to plot the power transmission and reflection coefficients in Eqn. (2.6) and (2.7) above. The results are hereby presented in section 2.1.3.

Both the power transmission and reflection coefficients above are observed to be periodic functions dependent on frequency f and thickness of the cavity L with resonant

frequencies f_m occurring at

$$
\begin{aligned}
\hat{\delta}_m &= m\pi, \qquad m = 0, 1, 2, ... \\
\frac{2\pi f_m}{c_0} nLcos\theta &= m\pi \\
f_m &= \frac{mc_0}{2nLcos\theta}
\end{aligned}
\tag{2.8}
$$

2.1.2   Some important etalon parameters

With the knowledge of the location of the maximum transmission peaks, the spectral interval between the peaks can be determined in terms of frequency or wavelength. This peak-to-peak interval is known as the Free Spectral Range (FSR).

$$
\begin{aligned}
FSR &= \Delta f = f_{m+1} - f_m \\
&= \frac{c_0}{2nLcos\theta} \quad (frequency) \\
&= \frac{\lambda^2}{2nLcos\theta} \quad (length)
\end{aligned}
\tag{2.9}
$$

(see appendix B for derivation of last part)

The above relationship implies that at a fixed angle of incidence (normally taken to be $0°$) the FSR of an ideal etalon is constant and inversely dependent on the optical path length (OPL) nL.

The separation between the points on either side of a maximum where the intensity has fallen to half the maximum value is called the full width at half maximum (FWHM). The third important parameter is the sharpness of the peaks. This is quantified by the ratio of the FSR to the FWHM. The parameter assigned to this is the finesse F.

To deduce the expressions for and the relationship between these parameters, consider a symmetrical system in which $R_1 = R_2 = R$, $T_1 = T_2 = T$ and $A_1 = A_2 = A$. Equation (2.6) above can therefore be rewritten as

$$
T = T_{max} \frac{1}{1 + \frac{4\sqrt{R_1 R_2}e^{-2\alpha L}}{(1 - \sqrt{R_1 R_2}e^{-2\alpha L})^2} sin^2\hat{\delta}}
\tag{2.10}
$$

where

$$
T_{max} = \frac{(1 - R - A)^2 e^{-2\alpha L}}{(1 - Re^{-2\alpha L})^2}
$$

For the mth peak, the intensity is half its maximum value at $\hat{\delta} = m\pi \pm \hat{\delta}_{1/2}$ and $\frac{T}{T_{max}} = \frac{1}{2}$.

This implies that

$$\hat{\delta}_{1/2} = sin^{-1}\left(\frac{4Re^{-2\alpha L}}{(1 - Re^{-2\alpha L})^2}\right)^{-1/2} \tag{2.11}$$

for large value of reflectance R

$$\hat{\delta}_{1/2} \approx \left(\frac{4Re^{-2\alpha L}}{(1 - Re^{-2\alpha L})^2}\right)^{-1/2} \tag{2.12}$$

Since the separation of adjacent peaks correspond to a change in phase of π in $\hat{\delta}$, the finesse is then

$$F = \frac{\pi}{2\hat{\delta}_{1/2}} = \frac{\pi}{2}\left(\frac{4Re^{-2\alpha L}}{(1 - Re^{-2\alpha L})^2}\right)^{1/2} = \frac{\pi\sqrt{R}e^{-2\alpha L}}{(1 - Re^{-2\alpha L})} \tag{2.13}$$

further

$$F = \frac{\pi}{\Delta\hat{\delta}} = \frac{\pi}{\hat{\delta}_{1/2} - \hat{\delta}_{-1/2}} = \frac{\pi}{\pi(\frac{2nLcos\theta}{c_0})(f_{1/2} - f_{-1/2})} = \frac{FSR}{FWHM} \tag{2.14}$$

2.1.3   Etalon characteristics

In the following the effect of various etalon parameters on its characteristics are investigated. The results below are derived for InP with a refractive index taken to be fixed at 3.15, i.e. dispersion is neglected, and a reference wavelength $\lambda = 1500$nm in free space (frequency $f_0 = 2e14$ Hz).

Figure 2.2 is a plot of the transmission characteristics for a lossless etalon ($A = 0$, $\alpha = 0$) with a thickness of $\lambda/2$ for various reflectance values. The plot shows the periodic nature in the variation with frequency. A higher reflectance results in a smaller FWHM, and a correspondingly higher finesse. The influence of A and α are seen in figures 2.3 and 2.4. Both have the effect of reducing the maximum transmission, hence an increase in FWHM. The transmission characteristics of a $\lambda/2$ thick etalon is plotted alongside that of a $\lambda/4$ thick etalon in Fig. 2.5. Note that at the reference frequency of 200 THz, the former has maximum transmission whereas the latter has minimum transmission. In general, from Eqn. (2.1) and (2.10) the maximum transmission will occur at the reference wavelength for an OPL of $nL = m\lambda/2$. Conversely, minimum transmission will occur for an OPL of $nL = (2m + 1)\lambda/4$ with $m = 0, 1, 2, ...$ The important point to note here therefore is that at the reference wavelength, the $\lambda/2$ etalon (or multiples thereof) acts as a resonator, whereas the $\lambda/4$ acts as a reflector. Another observation to make is that the FSR for the thinner etalon is larger than that of the thicker one as predicted in Eqn. (2.9). In applying the etalon principle to the design of optical devices for use in WDM systems,
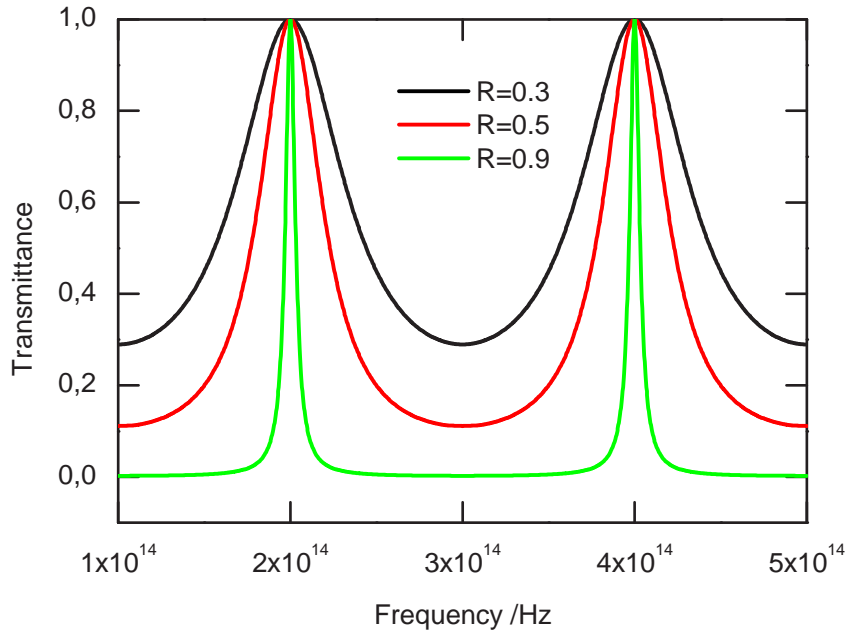
Fig. 2.2: Spectral transmittance of a lossless Fabry-Pérot etalon ($A = 0$, $\alpha = 0$) with a thickness of $\lambda/2$ for three reflectance R values.

the characteristics considered above are of utmost importance as they determine the cross-talk (or selectivity) between the neighbouring channels. Lower crosstalk is obtained for smaller FWHM, higher finesse and larger FSR.

2.1.4 DBR theory

A DBR is basically an arrangement of stacked $\lambda/4$ etalons made from materials of different refractive indices. It was demonstrated in the last section that a $\lambda/4$ etalon behaves as a reflector.

The basic theory behind the DBR is that an optical beam traversing an optical grating is scattered by each grating plane. If the Bragg condition is satisfied the contribution of the reflected beam from each plane add constructively in the backward direction to form a reflected beam with the centre frequency defined by the grating period Λ. The Bragg condition was derived by the physicist Sir W. H. Bragg and his son Sir W. L. Bragg in 1913 [59] to explain why crystals appear to reflect X-ray beams only at certain
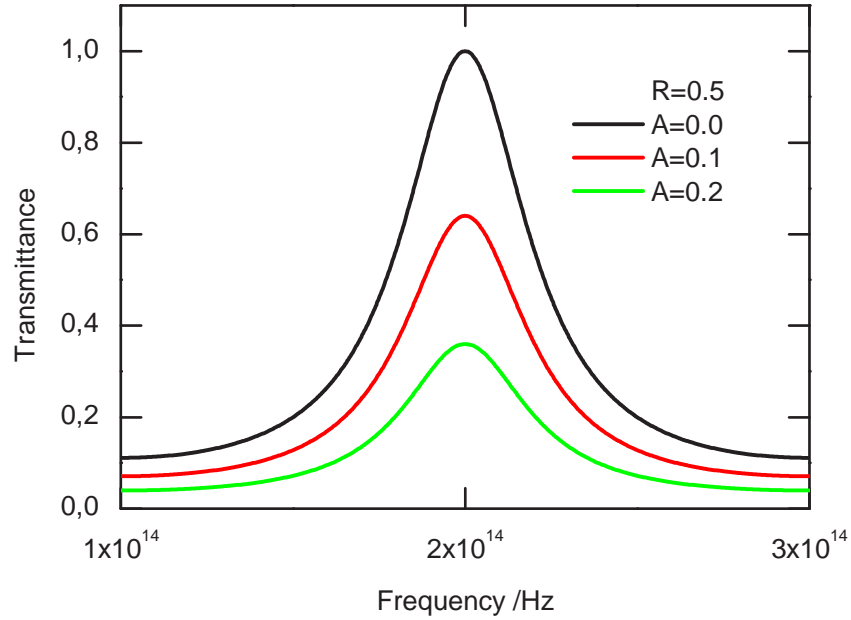
Fig. 2.3: Spectral transmittance of a Fabry-Pérot etalon with a reflectance $R = 0.5$ and varying loss factor factor A.

angles of incidence. The result was a direct evidence for the periodic nature of the atomic structure of crystals, which had already been postulated much earlier. The diagram of Fig. 2.6 illustrates this principle. The DBR is considered as a periodic arrangement of two materials with refractive indices n_1 and n_2, respectively, where $n_1 < n_2$. The incident beam is treated as a steam of coherent waves, two of which, A and B, are shown. These waves are reflected at O and O' to become A' and B', respectively. If A' and B' are in phase, they interfere constructively, thereby constituting a diffracted beam. The optical path difference between A' and B' is $PO'Q (= 2\Lambda\cos\theta)$. For diffraction to take place, this must be a whole wavelength in the medium i.e.

$$2\,\Lambda\,cos\theta = \lambda/n_{eff} \tag{2.15}$$

where n_{eff} is the effective refractive index of the grating.

The above relation in Eqn. (2.15) is known as the Bragg Law (or the Bragg condition).
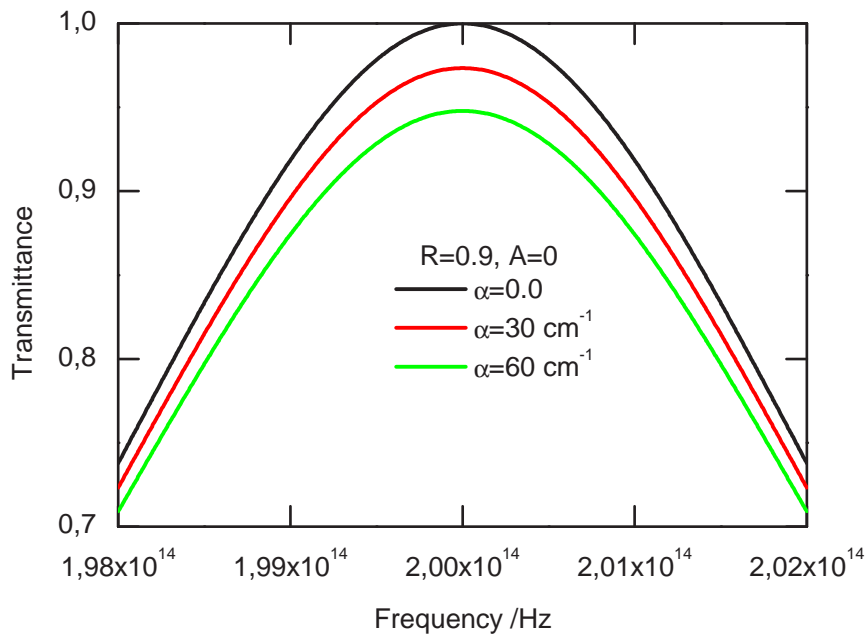
Fig. 2.4: Spectral transmittance of a Fabry-Pérot etalon with a reflectance $R = 0.5$, loss factor factor $A = 0$ and varying absorption coefficient.

2.2 Advanced numerical modelling tools

The above shown DBR grating can no longer be analysed by the simple relations derived for the etalon in the previous section. A lot of theoretical work has been reported on the optical analysis especially the prediction of the reflectivity of such a grating as a function of wavelength (or frequency). These mostly fall into two categories; the transfer function (or transmission) matrix method [60] and the coupled mode theory [61, 62].

2.2.1 Transmission matrix method

In this method the Bragg grating is treated as an alternating stratified medium. The transfer function of each medium is represented by a matrix. The product of all the matrices across the cascaded medium gives the overall transfer function. When the grating is periodic, a closed form solution for the reflectivity can be obtained, otherwise it is obtained numerically [63].
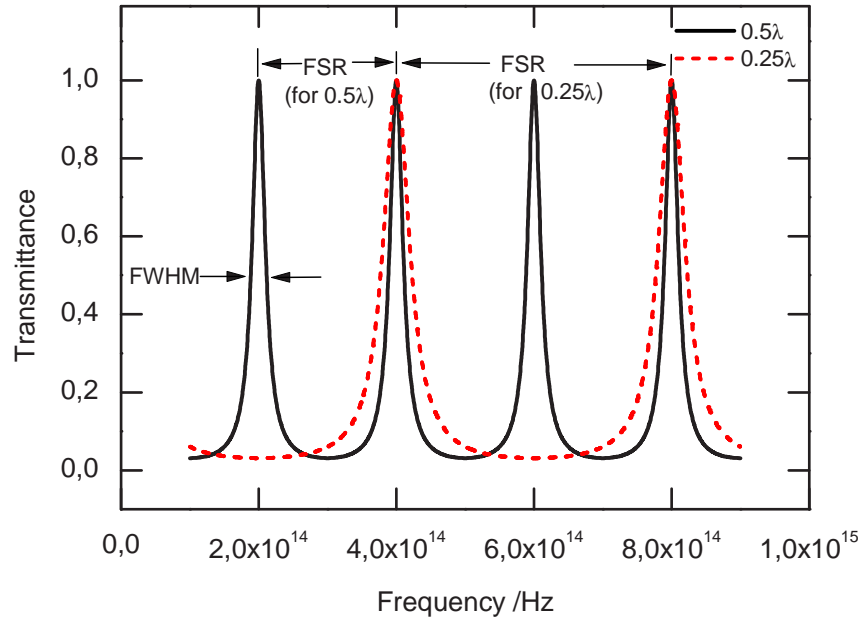
Fig. 2.5: Spectral transmittance of a half-λ and quarter-λ lossless Fabry-Pérot etalons with reflectance $R = 0.7$.

2.2.2 Coupled mode theory

In coupled mode theory, the forward and reverse travelling waves in a perturbed waveguide structure are coupled through the coupling coefficient $\kappa(\lambda)$. This coefficient is determined from the Fourier analysis of the refractive index variation with the structural length. For a periodic structure of length l, the reflectance R can be expressed as

$R = tanh^2(\kappa(\lambda), l)$

Other methods have been applied, however, it is not the aim here to make an exhaustive list of all the available methods, rather to demonstrate the use of the FEM in solving opto-electronic device design problems such as considered here.

2.2.3 The Finite Element Method

A simple description of the FEM would be that it is a method where a structure is split into several fragments (finite elements). The behaviour of each element is then represented
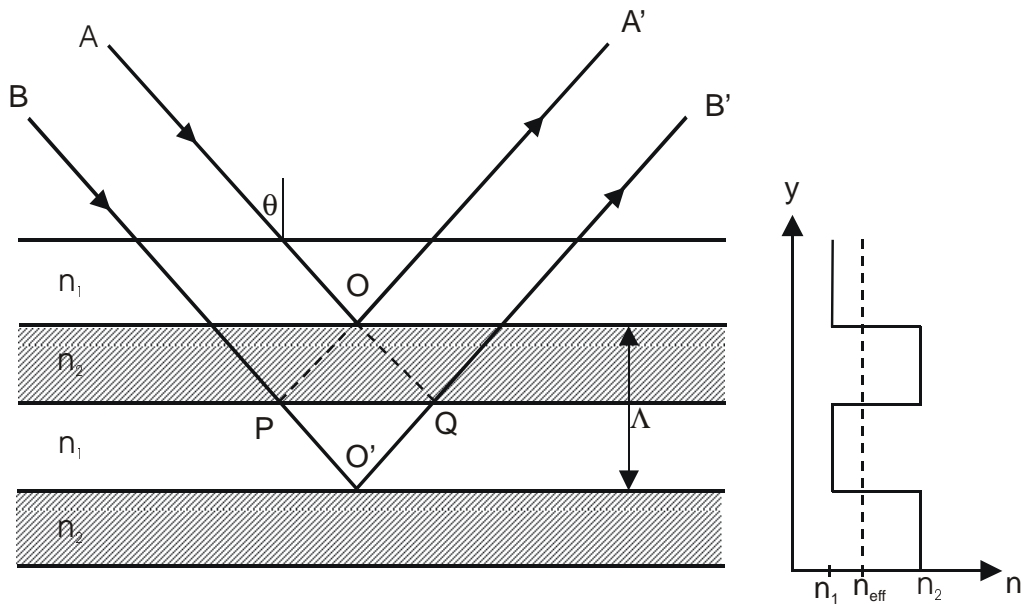
Fig. 2.6: Periodic stack arrangement of two materials with refractive indices n_1 and n_2 with $n_1 < n_2$ forming a distributed Bragg grating. A wave incident at an angle θ is shown diffracted by the grating.

using simple equation. Finally, all the elements are reconnected together. The resulting simultaneous algebraic equations (often in thousands) are then solved with the use of a computer. The result is the FEM output for the entire structure.

A more technical description is that the FEM is a piecewise polynomial interpolation. That is, over an element, a field quantity such as an electric field is interpolated from values of field quantity at nodes (element vertices). By connecting the elements together, the field quantity is interpolated over the entire structure in a piecewise manner by as many polynomial expressions as there are elements [64].

The power of the FEM lies in its flexibility. The structure is usually divided into triangular elements for 2D problems and tetrahedral elements for 3D problems (other polygons are used in other FEM software). The structure analysed may therefore have an arbitrary shape and loads, with hardly any restrictions. There is also the freedom to express material properties in many different ways; isotropic, anisotropic, orthotropic, and as arbitrary functions of space, time or even as arbitrary functions of the dependent variables. One drawback of FEM has been the high demand on the computational resources, especially CPU time and temporary storage (RAM). This problem is however becoming less significant with the advent of more powerful desktop computers and highly efficient solvers.

2.2.3.1 Modelling based on partial differential equations

A differential equation is one that expresses a function and its derivatives. Phenomena with several independent variables demand the use of partial differential equations (PDEs) as opposed to ordinary differential equations (ODEs) with just one independent variable, e.g. time. Many natural phenomena e.g. heat transfer, wave propagation, acoustics and even financial models are fully modelled with PDEs. One commercial software tool with the ability to solve complex PDE-based problems is FEMLAB. It enables almost any PDE to be directly implemented into it. These enables the simulation of many natural phenomena. In addition, several phenomena can be coupled through their PDEs in what is termed multi-physics.

In FEMLAB, three forms of PDE implementation are possible:

Coefficient form – for linear or almost linear PDEs

General form – for non-linear PDEs

Weak form – for more flexibility

The coefficient mode has been widely used for the cases presented in this work. The following is a brief outline of the implementation of a PDE in the coefficient form mode. For more details on this and the other two modes, the reader is referred to [65].

2.2.3.2 Implementing PDEs in coefficient form in FEMLAB

PDEs with more than one dependent variable can be implemented in FEMLAB. Consider an unknown function on the computational domain denoted by a single dependent variable u. The solution of its PDE yields its value. The coefficient form PDE formulation is as follows

$$-\nabla \cdot (-\hat{c}\nabla u - \hat{\alpha} u + \gamma) + \beta \cdot \nabla u + au = \hat{f} \qquad in\ \Omega \qquad (2.16)$$

$$\mathbf{n} \cdot (\hat{c}\nabla u + \hat{\alpha} u - \gamma) + qu = \hat{g} - h^T \hat{\mu} \qquad in\ \partial\Omega \qquad (2.17)$$

$$hu = r \qquad in\ \partial\Omega \qquad (2.18)$$

where

Ω is the computational domain –the union of all domains,

$\partial\Omega$ is the domain boundary, and

$\mathbf{n}$ is the outward unit normal vector on $\partial\Omega$.

Equation (2.16) is the PDE that must be satisfied in Ω. Equations (2.17) and (2.18) are the boundary conditions and must be satisfied on $\partial\Omega$. Eqn. (2.17) is the generalised

Neumann (mixed, natural or robin) boundary conditions, Eqn. (2.18) is the Dirichlet (essential) boundary conditions which normally represents constraints.

Although the PDE formulation can model all sorts of phenomena, the terminology used for the coefficients are borrowed from the field of continuum mechanics and mass transfer:

c is diffusion coefficient, $\hat{\alpha}$ conservative flux coefficient, β convection coefficient, a absorption coefficient, γ conservative flux source term, $\hat{f}$ source term, q boundary absorption coefficient, $\hat{g}$ boundary source term and $\hat{\mu}$ Lagrange multiplier.

To solve the PDE in FEMLAB, the values for the coefficients must be specified either in the graphical user interface or in a script file. The script file has the great advantage of flexibility. These coefficients can also be functions of spatial coordinates or other variables, e.g. time. A PDE is said to be linear when the coefficients are constants or depend only on the spatial coordinates and non-linear if they depend on u or its derivatives.

Time dependent problems

The time dependent PDE is similar to Eqn. (2.16) except it has an extra time derivative added

$$d_a \frac{\partial u}{\partial t} + \nabla \cdot (-\hat{c}\nabla u - \hat{\alpha}u + \gamma) + \beta \cdot \nabla u + au = \hat{f} \qquad in \ \Omega \qquad (2.19)$$

where d_a is the mass transfer coefficient.

Wave equation

The time dependent PDE in Eqn. (2.19) has a first order term. However, it is common to have second order time derivatives when describing wave phenomena as follows

$$d_a \frac{\partial^2 u}{\partial t^2} + \nabla \cdot (-\hat{c}\nabla u - \hat{\alpha}u + \gamma) + \beta \cdot \nabla u + au = \hat{f} \qquad in \ \Omega \qquad (2.20)$$

This is realised in FEMLAB using the "wave extension mode" where a new variable $\dot{u} = \partial u / \partial t$ is introduced. The equation above then becomes

$$d_a \frac{\partial \dot{u}}{\partial t} + \nabla \cdot (-\hat{c}\nabla u - \hat{\alpha}u + \gamma) + \beta \cdot \nabla u + au = \hat{f} \qquad in \ \Omega \qquad (2.21)$$

Solution of eigenvalue problems

Eigenvalue problems are solved in FEMLAB by use of the Eqn. (2.19) above by replacing the time derivative with $-\lambda_e u$ (where λ_e is the eigenvalue) and setting the source terms to zero ie;

$$-\lambda_e d_a u + \nabla \cdot (-\hat{c}\nabla u - \hat{\alpha}u) + \beta \cdot \nabla u + au \quad = \quad 0 \qquad in \; \Omega \tag{2.22}$$

$$\mathbf{n} \cdot (\hat{c}\nabla u + \hat{\alpha}u) + qu \quad = \quad -h^T \hat{\mu} \qquad in \; \partial\Omega \tag{2.23}$$

$$hu \quad = \quad 0 \qquad in \; \partial\Omega \tag{2.24}$$

2.3 Governing relations for analysis in photonics

2.3.1 General formulation

The PDEs and other relations needed for the analysis of optical characteristics of the devices in this work are derived from the Maxwell equations. The analysis below covers only as much as is essential for understanding the problem at hand. More comprehensive treatment of this topic is found in numerous excellent textbooks [66, 67].

Consider an electromagnetic wave with an electric field $\mathbf{E}$ and magnetic field $\mathbf{H}$ propagating in an isotropic medium with relative permittivity ϵ_r, relative permeability μ_r and conductivity σ. Assuming no charge density in the material, the following PDE characterises this propagation

$$\nabla^2 \mathbf{E} = \epsilon\mu \frac{\partial^2 \mathbf{E}}{\partial t^2} + \mu\sigma \frac{\partial \mathbf{E}}{\partial t} \tag{2.25}$$

where $\epsilon = \epsilon_r \epsilon_0$ and $\mu = \mu_r \mu_0$, and ϵ_0, μ_0 are permittivity and permeability of free space, respectively.

A similar relation holds for the magnetic field $\mathbf{H}$.

If the E-field is a plane-polarised, plane-harmonic wave, the E-field for the wave assumed to be propagating along z-axis with velocity υ can be represented as follows:

$$\mathbf{E} = E_0 e^{j\omega(t-z/\upsilon)} \tag{2.26}$$

If the wave has a non-zero phase φ at the temporal and spatial origin, then

$$\mathbf{E} = E_0 e^{j\varphi} e^{j\omega(t-z/\upsilon)} \tag{2.27}$$

where $E_0 e^{j\varphi}$ is the complex vector amplitude and $|E_0|e^{j\varphi}$ the scalar amplitude.

Substituting (2.26) into (2.25) results in

$$\frac{\omega^2}{\upsilon^2} = \omega^2 \epsilon \mu - j\omega\mu\sigma \tag{2.28}$$

If the material is a vacuum, $\sigma = 0$ and $\upsilon = c_0$, the velocity of light in a vacuum. Therefore,

$$\frac{1}{c_0^2} = \epsilon_0 \mu_0 \tag{2.29}$$

Dividing (2.28) by (2.29) yields

$$\frac{c_0^2}{\upsilon^2} = \frac{\epsilon\mu}{\epsilon_0\mu_0} - j\frac{\mu\sigma}{\omega\epsilon_0\mu_0} \tag{2.30}$$

It is immediately recognised from Eqn. (2.17) that c_0/υ is a refractive index –normally referred to as the complex refractive index $\bar{n}$, where

$$\bar{n}^2 = \epsilon_r\mu_r - j\frac{\mu_r\sigma}{\omega\epsilon_0} \tag{2.31}$$
$$\bar{n} = n - j\kappa \tag{2.32}$$

n is the refractive index and κ represents a damping factor known as the extinction coefficient.

By substituting for ω in equation Eqn. (2.26) with $\omega = 2\pi c_0/\lambda_0$ where λ_0 is the wavelength in free space, we get

$$\mathbf{E} = E_0 e^{j[\omega t - (2\pi\bar{n}/\lambda_0)z]} \tag{2.33}$$

Using (2.32) we obtain

$$\mathbf{E} = E_0 e^{-(2\pi\kappa/\lambda_0)z} e^{j[\omega t - (2\pi\bar{n}/\lambda_0)z]} \tag{2.34}$$

It is clear from Eqn. (2.34) how κ affects the amplitude of the wave in the medium. At a distance $z = \lambda_0/(2\pi\kappa)$, the wave amplitude will fall to $1/e$ of the initial value. The amplitude decays more rapidly for small λ and large κ.

Substituting (2.33) into (2.25) gives the Helmholtz PDE,

$$-\nabla^2\mathbf{E} - \bar{n}^2 k_0^2\mathbf{E} = 0 \tag{2.35}$$

or using (2.32), resulting in

$$-\nabla \times \left(\frac{1}{\mu}\nabla \times \mathbf{E}\right) - \left(\epsilon_r - j\frac{\sigma}{\omega\epsilon_0}\right)k_0^2\mathbf{E} = 0 \tag{2.36}$$

where $k_0 = \omega/c_0$ is the wave number (propagation constant) in free space.

In eigenvalue problems, the eigenvalue λ_e is equal to k_0^2.

2.3.2   PDE formulation for transverse electric (TE) waves

A wave with only one electric component in the y-direction and magnetic field components in the y-z plane is considered and described as

$$\mathbf{E}(x,z,t) = E_y(x,z)\mathbf{e}_y e^{j\omega t} \tag{2.37}$$

$$\mathbf{H}(x,z,t) = (H_y(x,z)\mathbf{e}_y + H_z(x,z)\mathbf{e}_z)e^{j\omega t} \tag{2.38}$$
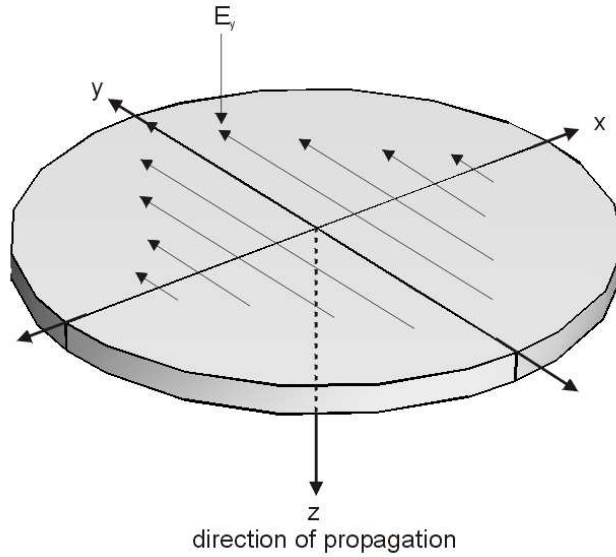
Fig. 2.7: Illustration of the electric field component of a plane polarised TE wave incident on the structure boundary.

The electric field, such as shown incident on the structure boundary in Fig. 2.7, can further be expressed as

$$\mathbf{E} \quad = \quad (0, E_y e^{j\omega t}, 0) \tag{2.39}$$

$$Real\,\mathbf{E} \quad = \quad (0, E_y cos\omega t, 0) \tag{2.40}$$

Hence, the wave propagating through the material is modelled using the scalar equation for the transverse electric field component E_y by applying (2.35) or (2.36) as

$$-\nabla^2 E_y - \bar{n}^2 k_0^2 E_y = 0 \tag{2.41}$$

or

$$-\nabla \times \left(\frac{1}{\mu}\nabla \times E_y\right) - \left(\epsilon_r - j\frac{\sigma}{\omega\epsilon_0}\right)k_0^2 E_y = 0 \tag{2.42}$$

FEMLAB allows for the implementation of such a model in 1D, 2D and 3D. In 1D only the maximum amplitude of the input field is given in the program i.e.

$$Real\,\mathbf{E} = (0, E_{0y}cos\omega t, 0) \tag{2.43}$$

For 2D and 3D implementation, the incident field can be further described in a more elaborate manner. For instance, a TE10 input field is described as follows

$$Real\,\mathbf{E} = (0, E_{0y}sin\frac{\pi}{a}x \cdot cos\omega t, 0) \tag{2.44}$$

where the entrance boundary has an origin at $x = 0$, and the width of the boundary is a.

2.3.3   Boundary conditions

Appropriate boundary conditions are an essential part of FEM simulations. Several types of boundaries can be specified for an electromagnetic problem in FEMLAB. Most of the boundary types namely electric field, magnetic field, surface current, low-reflecting, matched, impedance, transition and continuity can be defined directly by appropriately assigned values of coefficients of Eqn. (2.17) and (2.18). Some advanced types are specially implemented elements only available in the electromagnetic module of the software. These are the perfect magnetic conductor (PMC) and perfect electric conductor (PEC).

From (2.41) the boundary condition is expressed as

$$\mathbf{n} \cdot (\nabla E_y) + jkE_y = 2jkE_{0y}sin\frac{\pi}{a}x \cdot cos\omega t \tag{2.45}$$

and $k = 2\pi/(\lambda/\bar{n})$ is the propagation constant in material.

The factor $2jkE_{0y}sin\frac{\pi}{a}x \cdot cos\omega t$ is the driving force that represents the incoming planar wave. This assumes that the entrance boundary is on the plane $z = 0$. If not, then a more general form of the equation is needed i.e.

$$\mathbf{n} \cdot (\nabla E_y) + jkE_y = 2jke^{-jkz} \cdot E_{0y}sin\frac{\pi}{a}x \cdot cos\omega t \tag{2.46}$$

For an absorbing boundary (low reflecting) without a driving force, the RHS of Eqn. (2.45) is equated to zero.

2.3.4 Material properties

In most cases simple constants sufficiently describe the material properties. In cases where higher precision is demanded, dependence of material properties on parameters such as geometry, orientation in space, time, frequency, prevailing field conditions, e.t.c., must be taken into account. Materials when considered in terms of their electromagnetic properties can be roughly classified into five groups viz.; "simple", inhomogenous, anisotropic, non-linear and dispersive materials. "Simple" materials have constant properties. In inhomogenous materials, the properties vary with space coordinates. The field relations in anisotropic materials at a point depend on the direction of propagation. Usually a 3D tensor is needed to describe an anisotropic property. An anisotropic material is said to be reciprocal if its tensor is symmetric. Uniaxially anisotropic materials have two of the diagonal entries equal. A material is biaxially anisotropic if none of the elements have the same value. The variation of a material property with a field quantity is referred to as non-linearity. Hysteresis is a kind of non-linearity which in addition takes the history of the field distribution into account. Lastly, the phenomenon where the velocity of the wave (or refractive index) changes with the wavelength (see Eqn. (2.32)) is classified as dispersion.

2.3.5 The perfectly matched layer

The perfectly matched layer (PML) technique, first introduced by Berenger [68], is a popular method for truncating unbounded domains for wave propagation problems [69, 70, 71, 72]. The PML absorbs the electromagnetic waves without reflection from the vacuum-layer interface. In the PML domain and boundaries, nonphysical material properties are

introduced to attenuate the incident wave so that there is no reflection from the PML, mimicking the situation in an open unbounded space to give more realistic results.

The PML considered here obeys the Maxwell equations. The governing conditions for the PML are derived from the following assumptions for the PML region[70]:

$$\nabla \cdot [\epsilon]\mathbf{E} = 0 \tag{2.47}$$

$$\nabla \cdot [\mu]\mathbf{H} = 0 \tag{2.48}$$

$$\nabla \times \mathbf{E} = j\omega[\mu]\mathbf{H} - [\sigma_M]\mathbf{H} \tag{2.49}$$

$$\nabla \times \mathbf{H} = j\omega[\epsilon]\mathbf{E} - [\sigma_E]\mathbf{E} \tag{2.50}$$

where $[\mu]$ and $[\epsilon]$ are the effective permeability and permittivity of the PML region, respectively. The PML is assumed to be a diagonal anisotropic medium whose permeability and permittivity can be represented by the following tensors:

$$[\mu] = \mu_0 \begin{pmatrix} \mu_x + \frac{\sigma_M^x}{j\omega} & 0 & 0 \\ 0 & \mu_y + \frac{\sigma_M^y}{j\omega} & 0 \\ 0 & 0 & \mu_z + \frac{\sigma_M^z}{j\omega} \end{pmatrix} \tag{2.51}$$

and

$$[\epsilon] = \epsilon_0 \begin{pmatrix} \epsilon_x + \frac{\sigma_E^x}{j\omega} & 0 & 0 \\ 0 & \epsilon_y + \frac{\sigma_E^y}{j\omega} & 0 \\ 0 & 0 & \epsilon_z + \frac{\sigma_E^z}{j\omega} \end{pmatrix} \tag{2.52}$$

Figure 2.8 portrays a plane wave incident on the boundary between a vacuum and the PML.

For convenience let the tensors be

$$\frac{[\epsilon]}{\epsilon_0} = \frac{[\mu]}{\mu_0} = \begin{pmatrix} a & 0 & 0 \\ 0 & b & 0 \\ 0 & 0 & c \end{pmatrix} \tag{2.53}$$

An arbitrary polarised plane wave can be decomposed into a linear combination of transverse electric (TE) and transverse magnetic (TM) modes. In the TE case, the incident, reflected and transmitted fields can be expressed as follows;
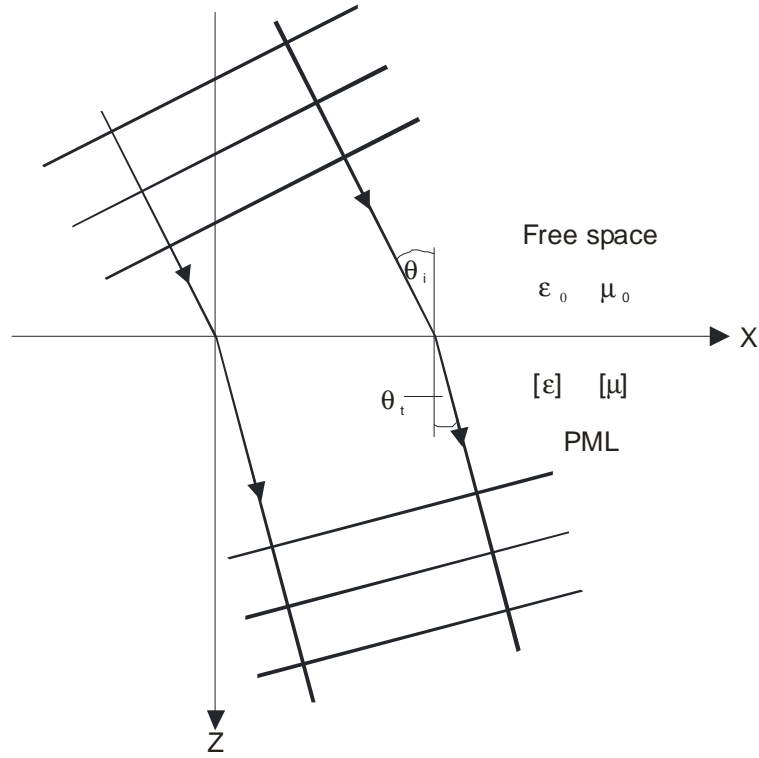
Fig. 2.8: Interaction of a plane wave at free space-PML boundary.

$$\mathbf{E}_i \;=\; E_{inc}\,\mathbf{e}_y\,e^{-jk_0(sin\theta_i x+cos\theta_i z)} \tag{2.54}$$

$$\mathbf{E}_r \;=\; R^{TE}E_{inc}\,\mathbf{e}_y\,e^{-jk_0(sin\theta_i x-cos\theta_i z)} \tag{2.55}$$

$$\mathbf{E}_t \;=\; T^{TE}E_{inc}\,\mathbf{e}_y\,e^{-jk_0(\sqrt{bc}sin\theta_t x+\sqrt{ab}cos\theta_t z)} \tag{2.56}$$

where R^{TE} and T^{TE} are the reflection and transmission coefficients, respectively. In this lossless interface, the following must hold true for continuity of the electric field and phase respectively

$$1 + R^{TE} \;=\; T^{TE} \tag{2.57}$$

$$\sqrt{bc}\,sin\theta_t \;=\; sin\theta_i \tag{2.58}$$

and continuity of the x-component of the magnetic field yields [70]

$$cos\theta_i - R^{TE}cos\theta_i = T^{TE}\sqrt{\frac{b}{a}}cos\theta_t \tag{2.59}$$

and finally, solving for R^{TE} gives;

$$R^{TE} = \frac{cos\theta_i - \sqrt{\frac{b}{a}}cos\theta_t}{cos\theta_i + \sqrt{\frac{b}{a}}cos\theta_t} \tag{2.60}$$

The same procedure can be used to derived the TM case.

To obtain zero reflection at the interface, we set $bc = 1$ in Eqn. (2.58) and $a = b$ in Eqn. (2.60). This leads to $a = b = 1/c = \alpha - j\beta$. The complex values for permittivity and permeability imply lossy material as shown in section 2.3.1. Equation (2.56) suggests that the wavelength in the material will be determined by α and the attenuation by β. For a reflection-free interface in the xy-plane,

$$[\epsilon_r] = [\mu_r] = \begin{pmatrix} \alpha - j\beta & 0 & 0 \\ 0 & \alpha - j\beta & 0 \\ 0 & 0 & 1/(\alpha - j\beta) \end{pmatrix} \tag{2.61}$$

One attractive feature of the PML as a boundary condition is that it provides a reflection-free interface for the outgoing wave at all incident angles in addition to preserving the sparse nature of the FEM matrix.

The optimum values of α and β are best determined empirically. They depend on the direction of the wave and the position of the PML layer (at face, edge or corner). In 2D and 3D problems, the permittivity and permeability tensors are different for different directions. Edges and corners have special tensors. For an edge in the z-direction, for instance, the values of $[\epsilon_r]$ and $[\mu_r]$ should be chosen so that $[\epsilon_r] = [\mu_r] = [\mu_r]_x \times [\mu_r]_y$. For corners, the $[\epsilon_r]$ and $[\mu_r]$ will be the product of the tensors in all the three coordinate directions.

To keep the model used in this work simple, the wave was damped along the expected direction of propagation. A PML thickness of at least 10% of the wavelength was enough to produce sufficient damping. The effect is clearly discernible in the results that follow.

2.4 Basics of the Fabry-Pérot DBR filter

2.4.1 Filter structure

The filters considered in this work are based on the Fabry-Pérot interferometer of Fig. 2.1 that consists of a $\lambda/2$ cavity sandwiched between two reflectors. The reflectors adopted for this work consist of InP/air DBRs with several periods as explained in section 2.1.4. This popular "quarter- half-quarter" design was first introduced by Geffcken in 1939 [73, 74] and has been widely applied in implementing vertical cavity devices as outlined in chapter 1. Presented in the following are the justification for the choice of the reflectors, and examples of the reflectance and transmission characteristics for the reflectors and for the resulting filter. The illustrations of the principle of operation presented in this section are based on a simplified FEM model that does not include dispersion and spectrally varying absorption. These can however be included by considering the wavelength dependence of the complex refractive index: the real part $real[\bar{n}(\lambda)]$ related to the dispersion and the imaginary part $im[\bar{n}(\lambda)]$ to the extinction coefficient according to Eqn. (2.32). Further, just one mode is considered for the illustration. Other modal responses can be introduced by appropriately modifying Eqn. (2.45). The emphasis of this thesis, however, is on the mechanical properties of the Fabry-Perot optical filter. Figures 2.9 to 2.15 illustrate the optical basics derived from the simplified FEM model and are not intended to be quantitatively precise in all details. For a detailed study on the optical properties of the filter using more refined methods the reader is referred to [75].

2.4.2 Choice of DBR grating configuration

Optical devices designed for use in WDM systems should have very small linewidths (FWHM) (<1nm) for optimum performance (high channel selectivity). It was shown in Eqn. (2.13) and (2.14) that to obtain a small FWHM, very high mirror reflectance is required. It has been shown that the reflectance of DBRs is a function of the refractive index contrast of the materials used and the number of grating periods [76, 77, 78]. The higher the refractive index contrast and the larger the number of the grating periods, the higher the reflectivity. Figure 2.9 depicts the results of FEM model calculations of the reflectance of two InP/air DBRs, one with two periods and the second with three periods. The three period grating gives a sufficiently high enough reflectance (>99%) to be used in a FP filter. The power density distribution in the two DBRs for a stop-band frequency is given in Fig. 2.10. The comparison of the electric field and power distribution in the

figures gives a clear visual evidence of the superior reflectance of the the 3-period grating.

2.4.3   DBR Fabry-Pérot filter characteristics

The 3-period DBR reflector in the preceding section is chosen for the realisation of a "quarter- half-quarter" Fabry-Pérot filter. The filter consists of two InP/air DBRs separated by a $\lambda/2$ resonant vertical air micro-cavity. Each of the DBRs made up of $\lambda/4$ layers as shown in Figure 2.12. In practice, the DBRs consist of circularly shaped InP membranes supported by 2, 3 or 4 suspensions, as shown in chapter 2. Figure 2.11 shows the transmission and reflection spectra of the filter. The narrow filter "window" (resonance) is clearly observed in the both sets of spectra. The diagram of Fig. 2.12 is the result of the FEM calculation showing the Electric field profile and the power density distribution in and around the filter at a stop-band wavelength (1400nm). Figure 2.13 is the field and power distribution at the "window" wavelength and Fig. 2.14 the field and power distribution at a frequency beyond the stop-band (2000nm).

2.4.4   Filter tuning concept

Tuning is achieved by varying the length of the cavity between the two reflectors. This has the effect of varying the "window" wavelength as depicted in Fig 2.15. This mechanical variation of the filter cavity can be achieved basically in two ways; thermally and electrostatically. The later concept is explored in depth in the later chapters. The implication here is that if this filter is placed in a channel with several separate wavelengths only one wavelength will be transmitted (selected) at a time. This is a highly attractive concept for WDM where compact optical devices with the ability to provide and redirect wavelengths as traffic demands are needed.

2.4.5   Mechanical tuning efficiency

Figure 2.15 shows the effect of cavity length change on the reflectance characteristics of the InP/air DBR Fabry Pérot filter. The cavity length is changed by ±50nm from the original length. This causes the resonant wavelength to change to 1497.5nm and 1587.5nm respectively. The total mechanical change in the cavity length of 100nm causes a change in the resonant wavelength of 90nm. The ratio of the two defines the mechanical tuning efficiency, which is 0.9 in this case.
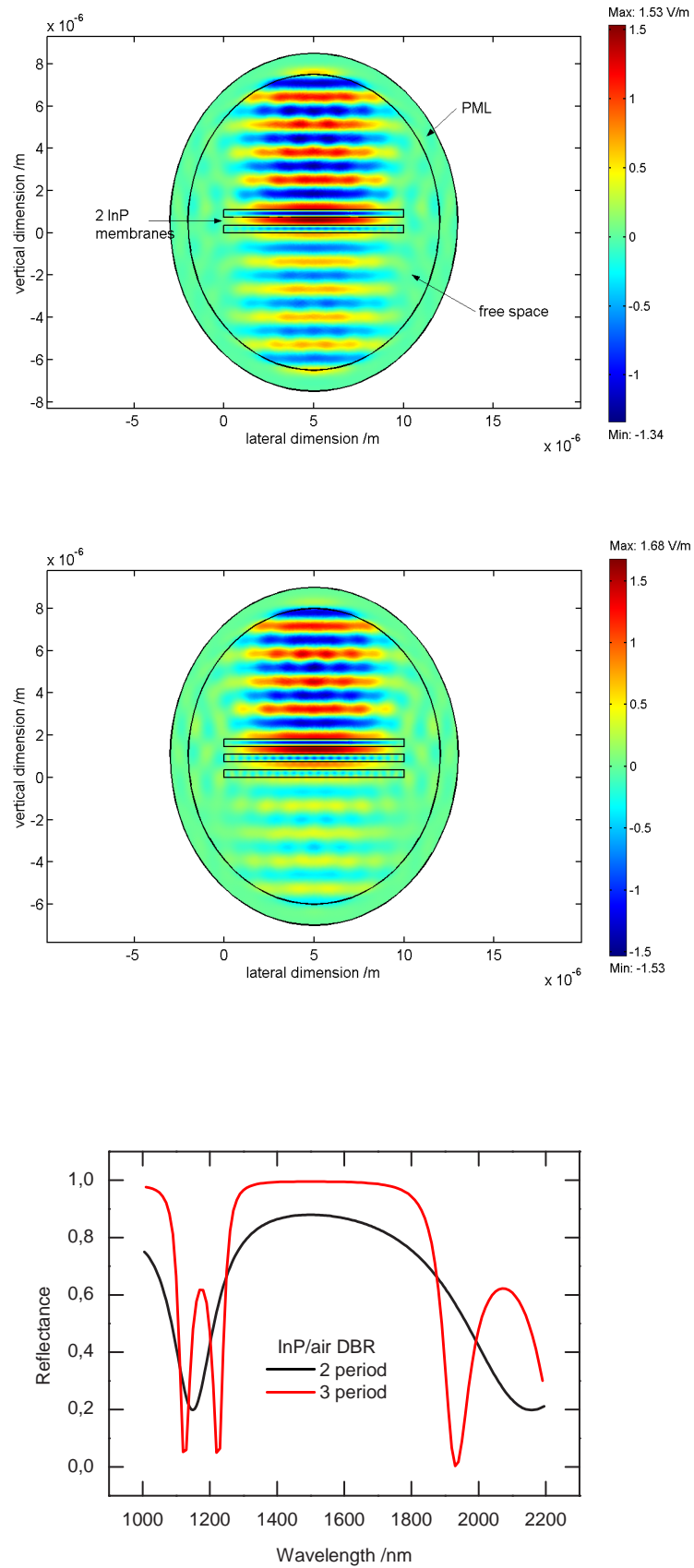
Fig. 2.9: Optical principle of the FP filter: Electric field distribution for a 2 period DBR (top) and a 3 period DBR (middle) at a stop-band frequency. Reflection spectrum (bottom).
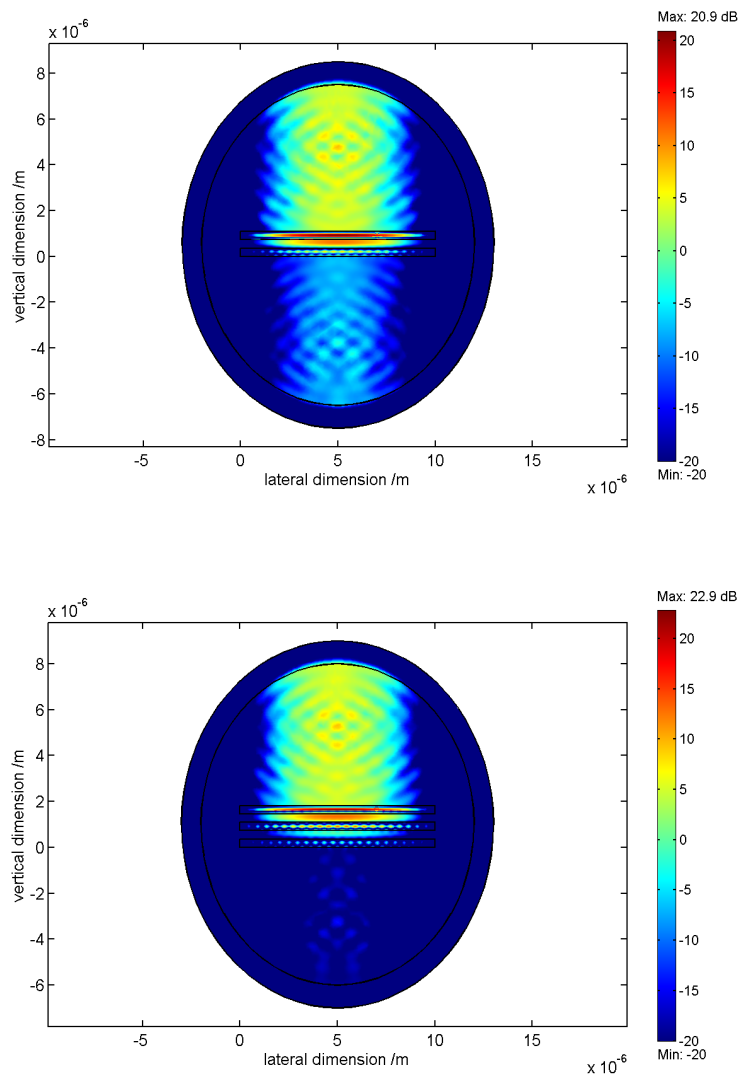
Fig. 2.10: Optical principle of the FP filter: Power distribution for 2 and 3 period DBR at a stop-band frequency.
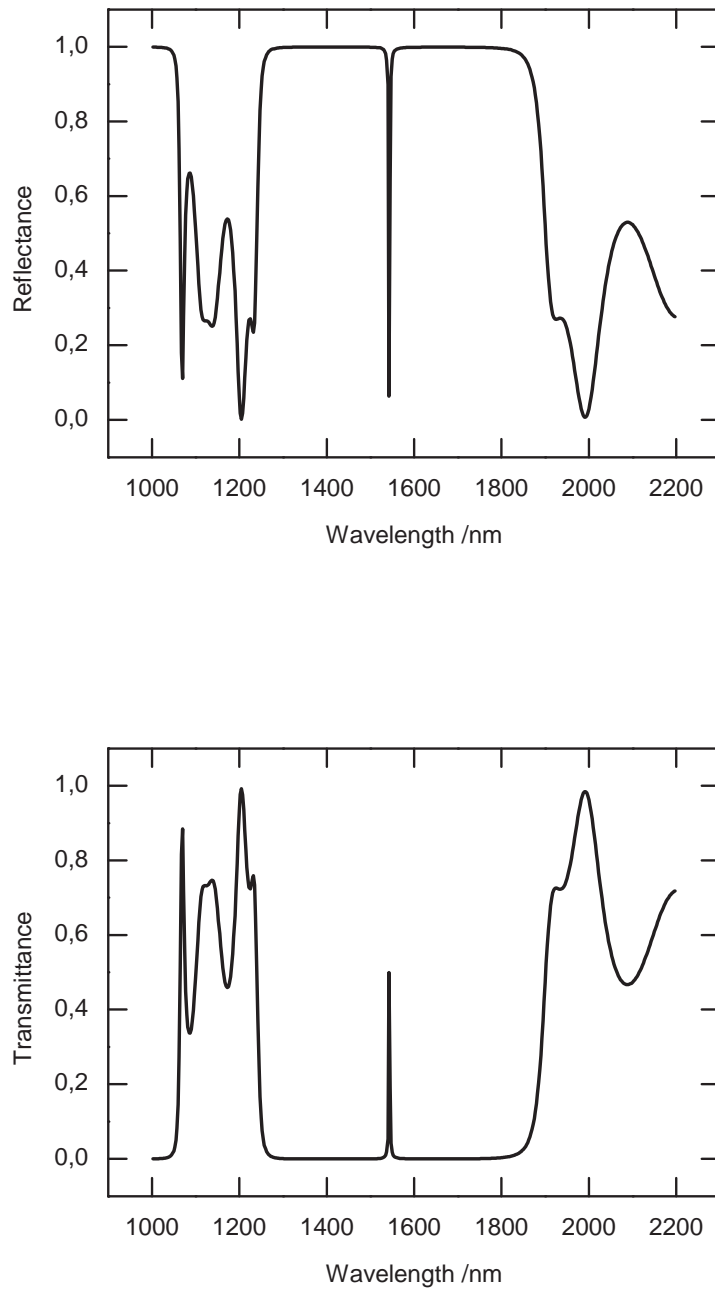
Fig. 2.11: Optical principle of the FP filter: Filter reflectance and transmittance characteristics.
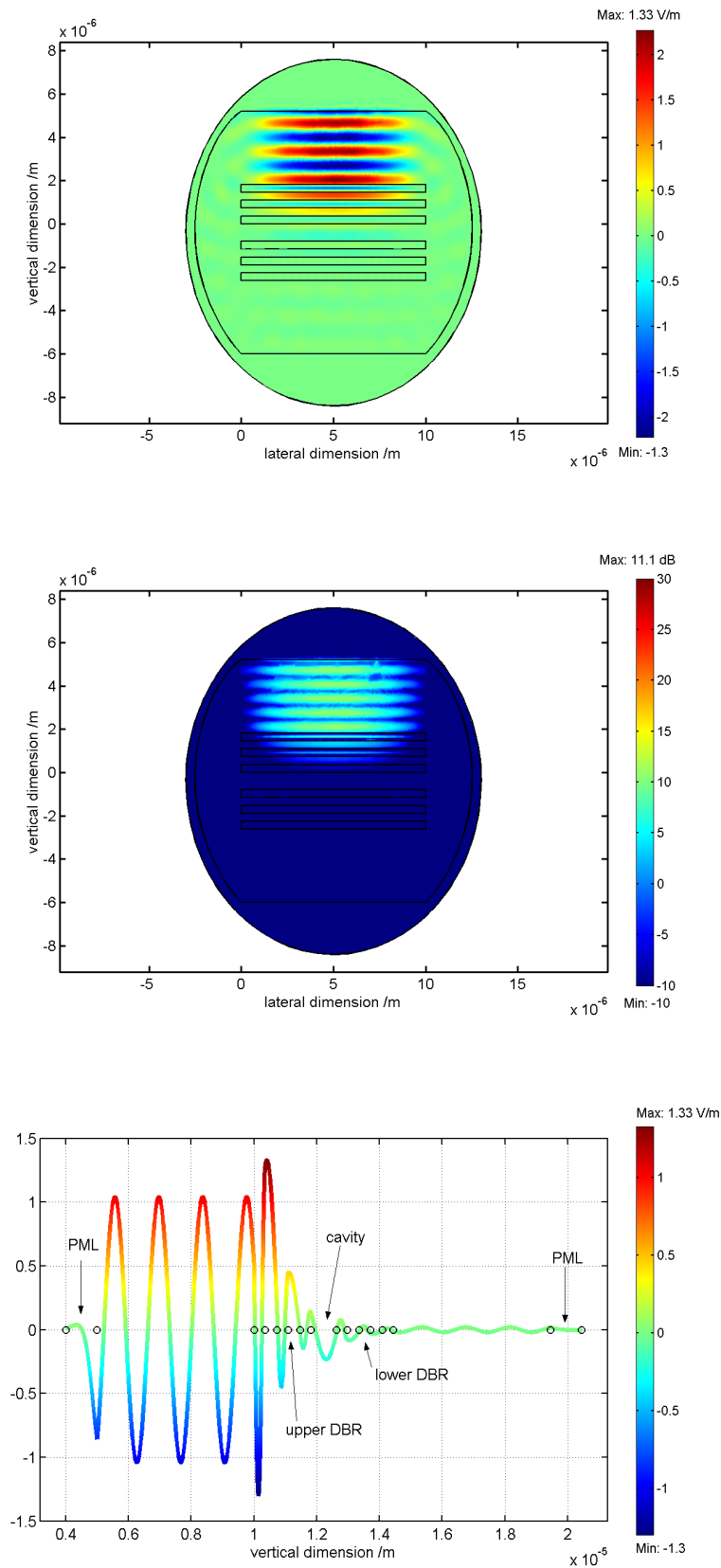
Fig. 2.12: Optical principle of the FP filter: Electric field distribution (top) and power distribution (middle), below is a 1D electric field distribution, all for a stop-band wavelength of 1400nm.
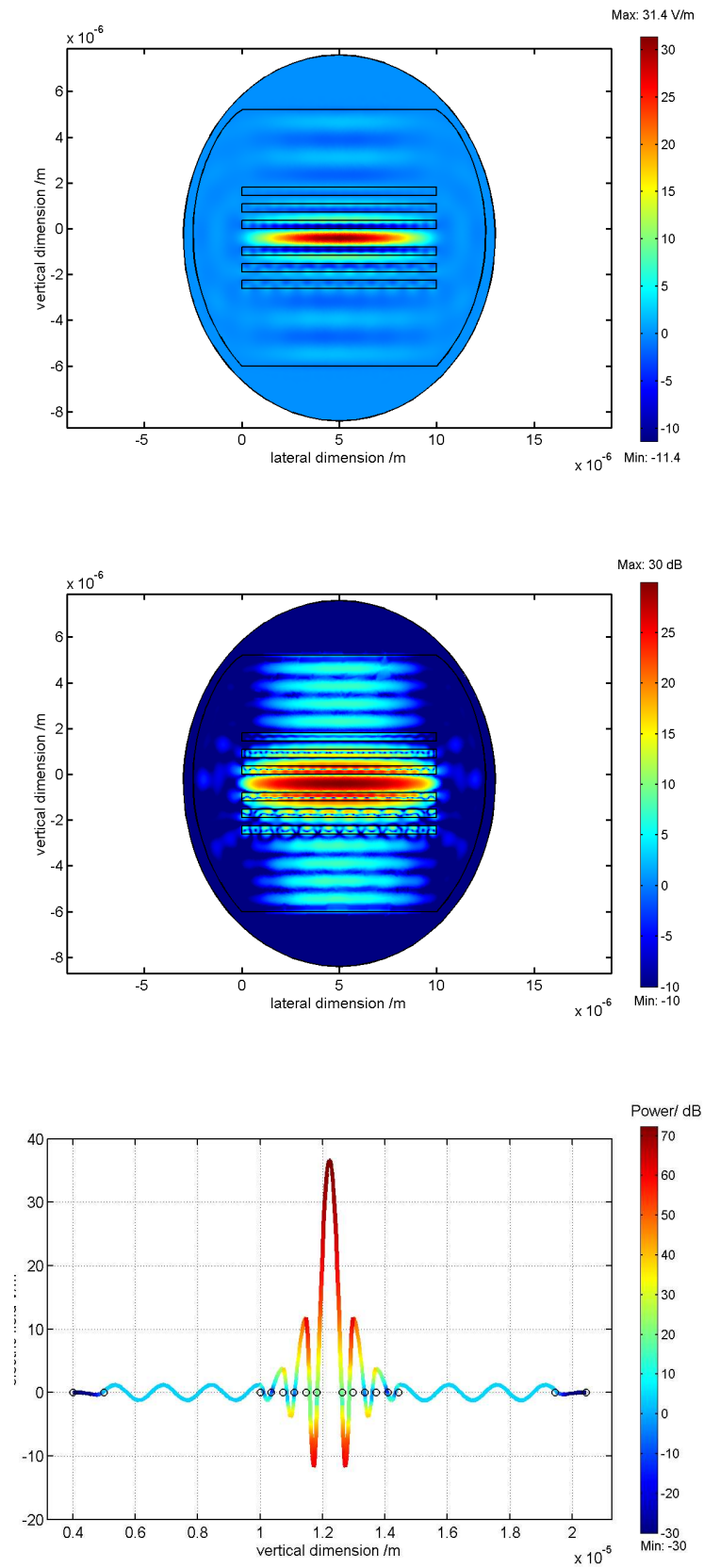
Fig. 2.13: Optical principle of the FP filter: Electric field distribution (top) and power distribution (middle), below is a 1D E-field and power distribution, all for the resonant wavelength.
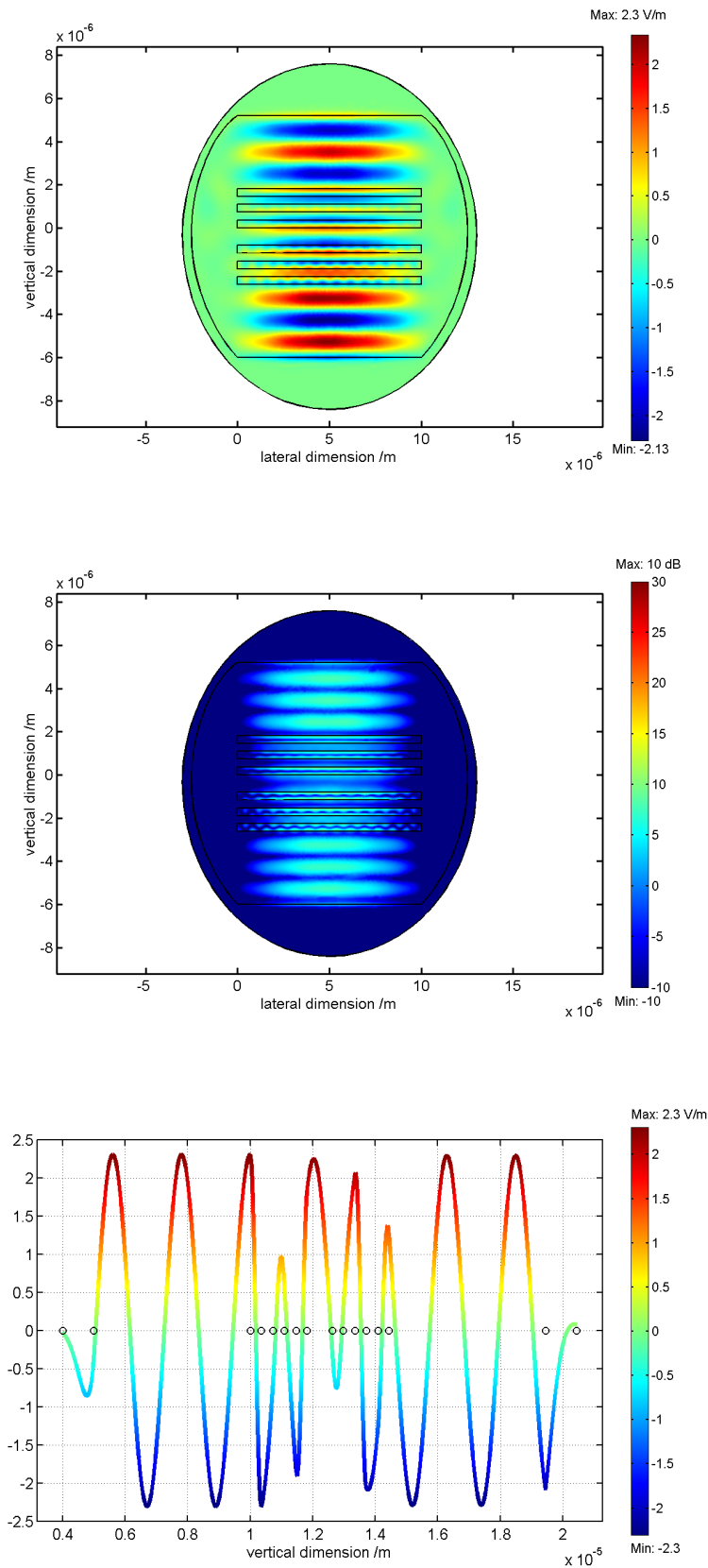
Fig. 2.14: Optical principle of the FP filter: Electric field (top) and power (middle) distribution, below is a 1D electric field distribution, all for a pass-band wavelength of 2200nm.
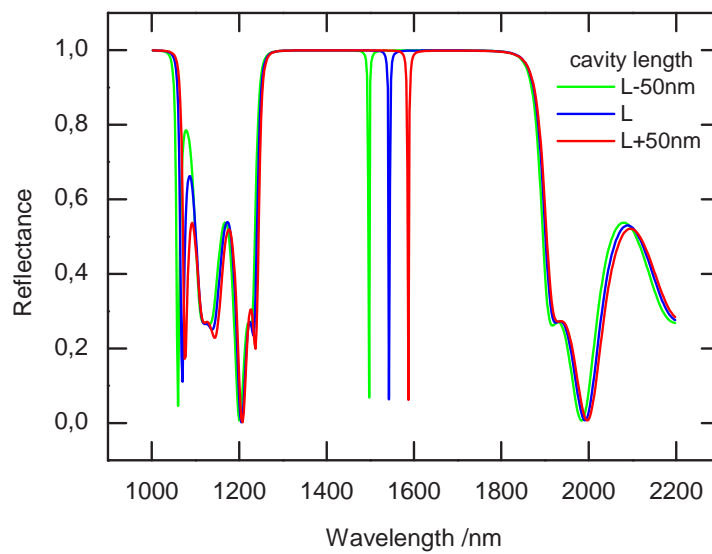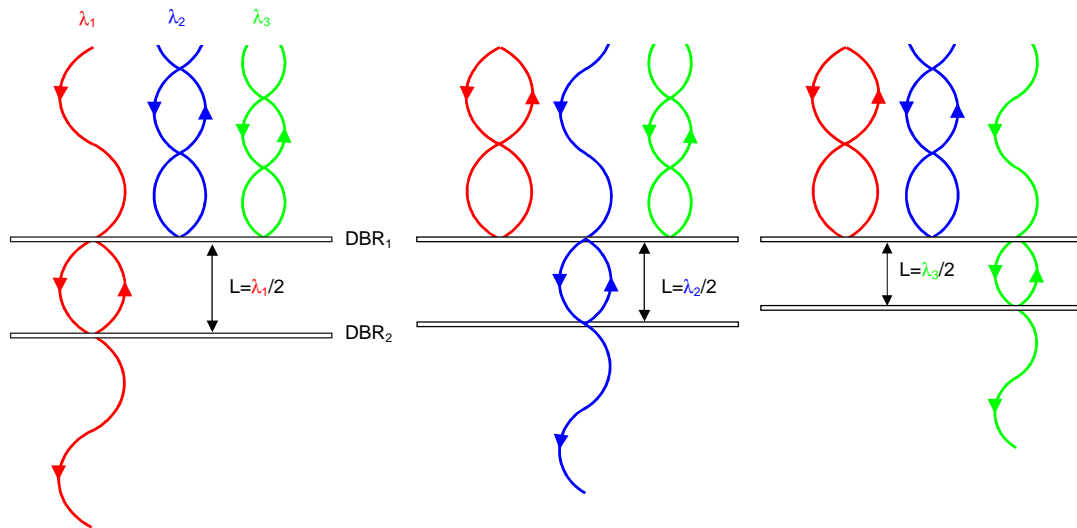
Fig. 2.15: Top: Schematic illustration of optical filtering concept showing three incident waves of different wavelengths λ_1, λ_2 and λ_3 as the cavity length changes from $\lambda_1/2$, to $\lambda_2/2$ and $\lambda_3/2$. Since the intuitive illustration of the principle is envisaged, the diagram does not include the phase-jumps at the interfaces. Bottom: Sample spectral tuning characteristics.

Chapter 3

Electromechanical model calculations

The tunable optical filters so far described are electrostatically actuated. In order to characterise and better understand the electromechanical tuning behaviour, a coupled structural mechanics-electrostatic model is needed. In this chapter, two such models are presented and used. One includes the full 3D structural mechanics model, which is naturally the best choice where applicable. However, there are certain cases where the 3D model fails to work in FEM, for instance, when the structures considered have very high aspect ratios (plate-like). In these cases several plate theories exist to overcome such bottlenecks. Examples of such theories are the Mindlin, Kirchoff-Love, Plane-stress, Plane-strain, von Karman and Higher order theories [79]. The basic idea of all plate theories is to reduce 3D elastic theory problems to 2D approximations. This reduction is accomplished by integrating out one of the dimensions - usually the thickness, which is then treated as a constant. In this work, the 2D Mindlin plate theory was used. Both the 2D and the 3D models used are described below. Each model is based on sound numerical quasi-static self-consistent computation of the membrane deformation under the combined effect of assumed linear elastic forces and and non-linear electrostatic forces. It is also demonstrated that both the models agree extremely well within the framework of application here. Alongside these, an analytic model is developed in addition to a systematic and comprehensive structural design procedure. The model, in combination with the procedure, leads to a quick and clear insight into the device performance at the start of the design phase. Finally at the end of the chapter, the results of the device deflection-voltage characteristics and stress stiffening effect are presented and analysed.

3.1   3D Structural Mechanics model

The 3D simulation of the electrostatic actuation of the filter membranes is based on a structural mechanics model in which the equilibrium equations for displacements, stresses, and strains in a material are solved [80]. The relationship between stress and strain in a material is described by Hooke's law. Using Hooke's law, all stress and strain components can be derived once the derivatives of the deformations have been obtained. To do this, the balance of force is formulated in terms of the deformation components.

The symmetric stress matrix below is the total description of the stress condition at a point.

σ_i are the stress components, τ_i the shear stresses

$$\sigma = \begin{bmatrix} \sigma_x & \tau_{xy} & \tau_{zx} \\ \tau_{xy} & \sigma_y & \tau_{yz} \\ \tau_{zx} & \tau_{yz} & \sigma_z \end{bmatrix}. \tag{3.1}$$

The relation between the different components are governed by the balance of force equations (static equilibrium condition);

$$\begin{aligned} -\frac{\partial \sigma_x}{\partial x} - \frac{\partial \tau_{xy}}{\partial y} - \frac{\partial \tau_{zx}}{\partial z} &= K_x \\ -\frac{\partial \tau_{xy}}{\partial x} - \frac{\partial \sigma_y}{\partial y} - \frac{\partial \tau_{yz}}{\partial z} &= K_y \\ -\frac{\partial \tau_{zx}}{\partial x} - \frac{\partial \tau_{yz}}{\partial y} - \frac{\partial \sigma_z}{\partial z} &= K_z \end{aligned} \tag{3.2}$$

K denotes volume (body) forces - analogous to gravitational force. Using compact notation

$$\nabla \cdot \sigma = \mathbf{K} \tag{3.3}$$

The strain conditions can be completely described in terms of the deformation com-

ponents u, v and w and their derivatives. The strain and shear strains are:

$$
\begin{aligned}
\varepsilon_x &= \frac{\partial u}{\partial x} \\[2mm]
\varepsilon_y &= \frac{\partial v}{\partial y} \\[2mm]
\varepsilon_z &= \frac{\partial w}{\partial z} \\[2mm]
\varepsilon_{xy} &= \frac{\gamma_{xy}}{2} = \frac{1}{2}\left(\frac{\partial u}{\partial y} + \frac{\partial v}{\partial x}\right) \\[2mm]
\varepsilon_{yz} &= \frac{\gamma_{yz}}{2} = \frac{1}{2}\left(\frac{\partial v}{\partial z} + \frac{\partial w}{\partial y}\right) \\[2mm]
\varepsilon_{zx} &= \frac{\gamma_{zx}}{2} = \frac{1}{2}\left(\frac{\partial w}{\partial x} + \frac{\partial u}{\partial z}\right)
\end{aligned}
\tag{3.4}
$$

For elastic materials there exists an unambiguous relation between the stress and the strain in the material. This is the Hooke's law which under the assumption of isotropic and isothermal condition relates the stresses and the strain by;

$$
\begin{aligned}
\varepsilon_x &= \frac{1}{E}[\sigma_x - \nu(\sigma_y + \sigma_z)] \\[2mm]
\varepsilon_y &= \frac{1}{E}[\sigma_y - \nu(\sigma_x + \sigma_z)] \\[2mm]
\varepsilon_z &= \frac{1}{E}[\sigma_z - \nu(\sigma_x + \sigma_y)] \\[2mm]
\varepsilon_{xy} &= \frac{1}{2G}\sigma_{xy} \\[2mm]
\varepsilon_{yz} &= \frac{1}{2G}\sigma_{yz} \\[2mm]
\varepsilon_{zx} &= \frac{1}{2G}\sigma_{zx}
\end{aligned}
\tag{3.5}
$$

alternatively,

$$
\begin{aligned}
\sigma_x &= \frac{E}{1+\nu}\left(\varepsilon_x + \frac{\nu}{1-2\nu}\left(\varepsilon_x + \varepsilon_y + \varepsilon_z\right)\right) \\
\sigma_y &= \frac{E}{1+\nu}\left(\varepsilon_y + \frac{\nu}{1-2\nu}\left(\varepsilon_x + \varepsilon_y + \varepsilon_z\right)\right) \\
\sigma_z &= \frac{E}{1+\nu}\left(\varepsilon_z + \frac{\nu}{1-2\nu}\left(\varepsilon_x + \varepsilon_y + \varepsilon_z\right)\right) \\
\tau_{xy} &= G\gamma_{xy} \\
\tau_{yz} &= G\gamma_{yz} \\
\tau_{zx} &= G\gamma_{zx}
\end{aligned}
\tag{3.6}
$$

In matrix form

$$
\begin{bmatrix} \sigma_x \\ \sigma_y \\ \sigma_z \\ \tau_{xy} \\ \tau_{yz} \\ \tau_{zx} \end{bmatrix} = \hat{D} \begin{bmatrix} \varepsilon_x \\ \varepsilon_y \\ \varepsilon_z \\ \gamma_{xy} \\ \gamma_{yz} \\ \gamma_{zx} \end{bmatrix}, \quad \hat{D} = \frac{E}{(1+\nu)(1-2\nu)} \begin{bmatrix} 1-\nu & \nu & \nu & 0 & 0 & 0 \\ \nu & 1-\nu & \nu & 0 & 0 & 0 \\ \nu & \nu & 1-\nu & 0 & 0 & 0 \\ 0 & 0 & 0 & \frac{1-2\nu}{2} & 0 & 0 \\ 0 & 0 & 0 & 0 & \frac{1-2\nu}{2} & 0 \\ 0 & 0 & 0 & 0 & 0 & \frac{1-2\nu}{2} \end{bmatrix}
$$

Now formulating the balance of force equations in terms the deformation components, the following system of three equations known as the Navier's equations is obtained;

$$
-\sum_j \left[\frac{\partial}{\partial x_j} G \left(\frac{\partial u_i}{\partial x_j} + \frac{\partial u_j}{\partial x_i} \right) + \frac{\partial}{\partial x_i} \left(\mu_L \frac{\partial u_j}{\partial x_j} \right) \right] = K_i
\tag{3.7}
$$

where E is the Young's modulus, ν Poisson's ratio, $G = \frac{1}{2}\left(\frac{E}{1+\nu}\right)$ is the shear modulus and $\mu_L = \frac{E\nu}{(1+\nu)(1-2\nu)}$, usually referred to as Lamé constant.

In case of small deformations and time dependency the equilibrium conditions are;

$$
\begin{aligned}
\rho\frac{\partial^2 u}{\partial t^2} - \frac{\partial \sigma_x}{\partial x} - \frac{\partial \tau_{xy}}{\partial y} - \frac{\partial \tau_{zx}}{\partial z} &= K_x \\
\rho\frac{\partial^2 v}{\partial t^2} - \frac{\partial \tau_{xy}}{\partial x} - \frac{\partial \sigma_y}{\partial y} - \frac{\partial \tau_{yz}}{\partial z} &= K_y \\
\rho\frac{\partial^2 w}{\partial t^2} - \frac{\partial \tau_{zx}}{\partial x} - \frac{\partial \tau_{yz}}{\partial y} - \frac{\partial \sigma_z}{\partial z} &= K_z
\end{aligned}
\tag{3.8}
$$

and the corresponding formulation of Navier's equations are

$$\rho\frac{\partial^2 u_i}{\partial t^2} - \sum_j \left[\frac{\partial}{\partial x_j} G \left(\frac{\partial u_i}{\partial x_j} + \frac{\partial u_j}{\partial x_i} \right) + \frac{\partial}{\partial x_i} \left(\mu_L \frac{\partial u_j}{\partial x_j} \right) \right] = K_i \tag{3.9}$$

In compact notation

$$\rho\frac{\partial^2 \mathbf{u}}{\partial t^2} - \nabla \cdot \hat{c}\nabla\mathbf{u} = \mathbf{K} \tag{3.10}$$

where $\hat{c}$ is a tensor defined as follows;

$$\hat{c} = \begin{bmatrix} \begin{bmatrix} D_{11} & 0 & 0 \\ 0 & D_{44} & 0 \\ 0 & 0 & D_{66} \end{bmatrix} & \begin{bmatrix} 0 & D_{13} & 0 \\ D_{44} & 0 & 0 \\ 0 & 0 & 0 \end{bmatrix} & \begin{bmatrix} 0 & 0 & D_{13} \\ 0 & 0 & 0 \\ D_{66} & 0 & 0 \end{bmatrix} \\ \begin{bmatrix} 0 & D_{44} & 0 \\ D_{21} & 0 & 0 \\ 0 & 0 & 0 \end{bmatrix} & \begin{bmatrix} D_{44} & 0 & 0 \\ 0 & D_{22} & 0 \\ 0 & 0 & D_{55} \end{bmatrix} & \begin{bmatrix} 0 & 0 & 0 \\ 0 & 0 & D_{23} \\ 0 & D_{55} & 0 \end{bmatrix} \\ \begin{bmatrix} 0 & 0 & D_{66} \\ 0 & 0 & 0 \\ D_{31} & 0 & 0 \end{bmatrix} & \begin{bmatrix} 0 & 0 & 0 \\ 0 & 0 & D_{55} \\ 0 & D_{32} & 0 \end{bmatrix} & \begin{bmatrix} D_{66} & 0 & 0 \\ 0 & D_{55} & 0 \\ 0 & 0 & D_{33} \end{bmatrix} \end{bmatrix}$$

alternatively,

$$\hat{c} = \begin{bmatrix} \begin{bmatrix} 2G + \mu_L & 0 & 0 \\ 0 & G & 0 \\ 0 & 0 & G \end{bmatrix} & \begin{bmatrix} 0 & \mu_L & 0 \\ G & 0 & 0 \\ 0 & 0 & 0 \end{bmatrix} & \begin{bmatrix} 0 & 0 & \mu_L \\ 0 & 0 & 0 \\ G & 0 & 0 \end{bmatrix} \\ \begin{bmatrix} 0 & G & 0 \\ \mu_L & 0 & 0 \\ 0 & 0 & 0 \end{bmatrix} & \begin{bmatrix} G & 0 & 0 \\ 0 & 2G + \mu_L & 0 \\ 0 & 0 & G \end{bmatrix} & \begin{bmatrix} 0 & 0 & 0 \\ 0 & 0 & \mu_L \\ 0 & G & 0 \end{bmatrix} \\ \begin{bmatrix} 0 & 0 & G \\ 0 & 0 & 0 \\ \mu_L & 0 & 0 \end{bmatrix} & \begin{bmatrix} 0 & 0 & 0 \\ 0 & 0 & G \\ 0 & \mu_L & 0 \end{bmatrix} & \begin{bmatrix} G & 0 & 0 \\ 0 & G & 0 \\ 0 & 0 & 2G + \mu_L \end{bmatrix} \end{bmatrix}$$

The PDE in Eqn. (3.10) is what is solved with the aid of the FEM to obtain the stresses, strains and the displacements resulting from the applied forces.

3.2 Electrostatic coupling

The force needed for actuation in the structural mechanics model above is obtained electrostatically. This concept of an actuator, i.e. a transducer that can convert some form of energy (electrical, thermal, etc) into mechanical energy is central to micro-electro-mechanical systems (MEMS). The most basic MEMS actuator is the parallel-plate electrostatic actuator. In this analysis, an important simplifying assumption is made: That the electric field is uniform between the plates of the actuator (filter membranes) and zero outside. Strictly speaking, the electric field has a non-zero curl at the edges, violating Maxwell's equation. This assumption can lead to loss of accuracy in cases where one of the plates is much larger that the other or if the second plate is an infinite ground. In such cases compensating correction factors for the force have been worked out to correct this fringing loss [81]. In the cases considered here, both membranes are wide and of identical size and shape with a relatively small separation, hence the assumption should not cause any significant loss in accuracy.

The uniform field between the membranes has a magnitude:

$$E = \frac{Q}{\varepsilon_0 A} \tag{3.11}$$

where Q is the charge on each membrane, A the area of the membrane and ε_0 the permittivity of free space.

The field creates an electrostatic force f_{es} that attracts the membranes to each other. The magnitude of f_{es} on each membrane is

$$
\begin{aligned}
f_{es} &= \frac{QE}{2} \\
&= \frac{\varepsilon_0 A V^2}{2g^2}
\end{aligned}
\tag{3.12}
$$

where g is the separation between the membranes and V the applied voltage.

Assuming the two membranes of the filter to be on two concurrent x-y planes in the cartesian space, the separation is in the z-direction, i.e. $g(z)$. The filter deflection is not uniform throughout the span of the membrane structure. It is maximum at the centre and progressively reduces to zero at the supporting posts as shown in Fig. 3.1. The force equation can therefore be rewritten as a force per unit area p at a point z where there is an arbitrary deflection δ as follows:
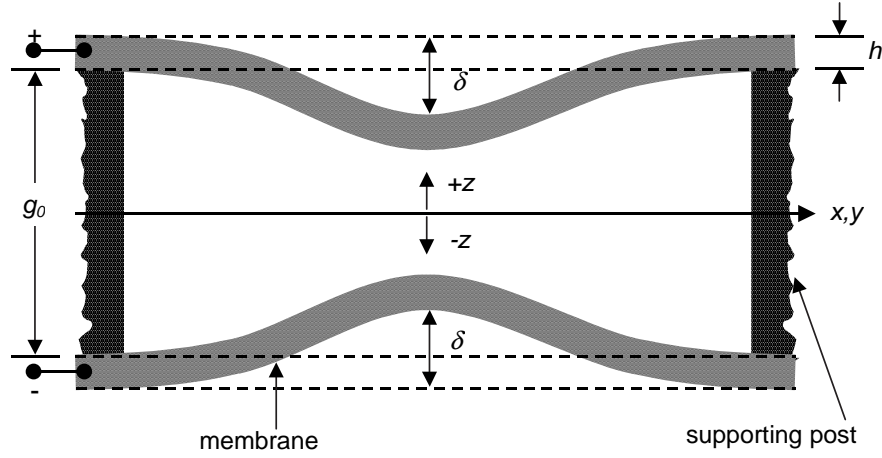
Fig. 3.1: Illustration of membrane deflection showing the two innermost membranes each deflected by an amount δ at the centre along the z-axis. Before actuation the membranes lie on parallel cartesian xy planes.

$$
\begin{aligned}
p(z) &= \frac{\varepsilon_0 V^2}{2g(z)^2} \\
&= \frac{\varepsilon_0 V^2}{2(g_0 - 2\delta)^2}
\end{aligned}
\tag{3.13}
$$

the initial separation being designated by g_0. If the plane $z = 0$ lies exactly in between the two membranes

$$
\begin{aligned}
p(z) &= \frac{\varepsilon_0 V^2}{2(2z)^2} \\
&= \frac{\varepsilon_0 V^2}{8z^2}
\end{aligned}
\tag{3.14}
$$

Considering the symmetry in the problem is important in the FEM calculations in that only one part of the symmetrical equivalents needs to be considered, saving on hardware resource requirements and computation time.

In this 3D model, the electrostatic force is introduced as a boundary condition. This is based on the fact that the charges of opposite polarity causing this force will be concentrated on the facing (inner) surfaces of the membranes. There are two types of boundary conditions used in this model. Those used to specify loads as a force per area p_x, p_y and p_z and those used to specify constraints x-, y-, and z-displacements. The electrostatic force

is introduced as load boundary condition viz.,

$$
\begin{aligned}
p_x &= (\mathbf{n} \cdot \sigma)_x \\
p_y &= (\mathbf{n} \cdot \sigma)_y \\
p_z &= (\mathbf{n} \cdot \sigma)_z
\end{aligned}
$$

σ symbolises the stress components, and $\mathbf{n}$ the normal vector.

In the cases considered here, p_x and p_y are equal to zero, which means there are no applied lateral forces, and

$$
p_z = (\mathbf{n} \cdot \sigma)_z = \frac{\varepsilon_0 V^2}{8z^2} \tag{3.15}
$$

A validation of the accuracy of the electrostatic coupling technique and assumptions described above is presented in appendix C. The same will be applied in the following section.

3.3   The 2D Mindlin Theory Model

In one part of this study, the membrane thickness was scaled down to a point where the 3D model described above did not work anymore. A 2D treatment was therefore required in this case. The Mindlin plate theory [79, 82] was applied. Strictly speaking, the word "membrane" is used in this work in the loose sense of the word meaning a thin object. This is in conformity with previous literature in this field. For small deflections, thin plate theory is said to be dominated by elastic resistance of the plate bending. In contrast, deflection in membrane theory is dominated by stress in the membrane. In the case here, small deflections and negligible amounts of in-plane stress were initially assumed, later the effect of residual stress is studied. The Mindlin plate model approximates the transversal displacement and the bending rotations of the transverse normals to the plate by a system of eight partial differential equations known as the Mindlin equations. The equations are appealing because they are of lower order than the classical biharmonic plate equation, allow the computation of shear strains and admit the thickness of the plate as a parameter. This enables the implementation of the solution as a 2-dimensional problem, resulting in accurate and faster solutions requiring less computing resources as

compared to the full 3-D elasticity calculations. Mindlin's theory gives the displacement at (x, y, z) as $\mathbf{u} = z\Psi(x, y, t) + w(x, y, t)\mathbf{e}_z$, where (x, y) is the 2-D position on the central plane of the plate, z is the transverse coordinate, with $z = 0$ the center plane of the plate, $\Psi = (\psi_x, \psi_y)$ is the in-plane vector of rotations and w the transverse displacement. The governing equations of motion are expressed in terms of stress resultants as follows [79]:

$$\frac{\partial M_x}{\partial x} + \frac{\partial M_{xy}}{\partial y} - Q_x = \frac{\rho h^3}{12} \frac{\partial^2 \psi_x}{\partial t^2} \tag{3.16}$$

$$\frac{\partial M_{xy}}{\partial x} + \frac{\partial M_y}{\partial y} - Q_y = \frac{\rho h^3}{12} \frac{\partial^2 \psi_y}{\partial t^2} \tag{3.17}$$

$$\frac{\partial Q_x}{\partial x} + \frac{\partial Q_y}{\partial y} + p(w) = \rho h \frac{\partial^2 w}{\partial t^2} \tag{3.18}$$

where ρ is the plate material density, h the plate thickness and $p(w)$ the external electrostatic loading on the plate. The bending moments per unit length of plate M_x, M_y, and M_{xy}, and the transverse shear forces per unit length Q_x and Q_y are defined as

$$M_x = D\left(\frac{\partial \psi_x}{\partial x} + v\frac{\partial \psi_y}{\partial y}\right) \tag{3.19}$$

$$M_y = D\left(\frac{\partial \psi_y}{\partial y} + v\frac{\partial \psi_x}{\partial x}\right) \tag{3.20}$$

$$M_{xy} = \frac{1}{2}D(1 - v)\left(\frac{\partial \psi_x}{\partial y} + v\frac{\partial \psi_y}{\partial x}\right) \tag{3.21}$$

$$Q_x = \kappa^2 Gh\left(\frac{\partial w}{\partial x} + \psi_x\right) \tag{3.22}$$

$$Q_y = \kappa^2 Gh\left(\frac{\partial w}{\partial y} + \psi_y\right) \tag{3.23}$$

where

$$D = \frac{Eh^3}{12(1 - v^2)}$$

is the flexural rigidity, and κ^2 the shear correction factor that compensates for the non-uniform shear stress in the plate [83]. The electrostatic force (per unit area) acting on the membrane is a distributed force that depends non-linearly on the membrane deflection according to Eqn. (3.13). By substituting the set of equations (3.19)-(3.23) into (3.16)-

(3.18) the following are obtained

$$\frac{D}{2}\left\{(1-\nu)\nabla^2\psi + (1+\nu)\nabla\nabla\cdot\psi\right\} - \kappa^2 Gh(\psi + \nabla w) = \frac{\rho h^3}{12}\frac{\partial^2\psi}{\partial t^2}, \tag{3.24}$$

$$\kappa^2 Gh(\nabla^2 w + \nabla\cdot\psi) + p(z) = \rho h\frac{\partial^2 w}{\partial t^2} \tag{3.25}$$

The above equations (3.13), (3.24) and (3.25) are implemented as quasi-static and time-dependent coefficient forms in FEMLAB. The results of the implementation are in very good agreement with standard benchmarks [84, 85]. In addition to determining the plate displacement resulting from an applied electrostatic force, the implementation enables modal analysis to determine the eigen-frequencies, the mode shapes, as well as the temporal response resulting from electrostatic actuation or a gravitational shock impulse impinging on the structures as will be demonstrated in chapter 5.

The structure is defined in the software as a two dimensional geometry with the thickness h plugged into the equation system as a constant parameter as shown in the equations above. If so desired, it is possible to specify an arbitrary thickness variation as long as it can be described in terms of the lateral space coordinates of the membrane. The boundary conditions used at the suspension-supporting post interface are of the clamped type. Otherwise all the rest of the boundaries are set free.

3.4 Analytical Model Development

The two inner membranes of the air-gap filter considered are modelled here using a lumped spring model as shown in the diagram in Fig. 3.2. A quantitative closed-form model for the spring constant is developed based on the dimensions and material properties of the membranes. The phrase "closed-form" is used here to describe an empirical fit to simulated data from FEM calculations using a theoretically derived functional form.

Closed-form equations are very useful in design in that they provide an often simple and quick insight at the beginning of the design phase without using computer resource demanding methods. In this work, the closed-form model is applicable in determining the structural device dimensions at the design phase based on the laid out desired specifications and in predicting the tuning range of the device. Numerous models abound in the literature where the authors have presented closed-form models for electrostatic actuation [81, 86, 87, 88, 89, 90, 91, 92, 33]. These models are mostly for the closed-

form expressions for the pull-in voltage of beams and other regular geometries such as circular membranes. Three factors distinguish our structures from these as follows: The filter structures considered here have beam-like suspensions but with a centre circular membrane. Secondly, the width of the structures are much bigger ($\gg$ 5 times) than the thickness so that the structures are treated as plates with flexural rigidity instead of simply as beams with a modulus of elasticity. Lastly, two parallel, wide, identical structures separated by a relatively small gap are considered in this work as opposed to one beam or plate against an infinite ground in most of the cited cases. In our case, the fringing effect is rendered negligible and does not call for a correction factor in the model. The pull-in voltage is important in this work in so far as determining the maximum tuning range of the device. For normal use of the tunable filter, the operation must steer clear of the pull-in point, otherwise catastrophic consequences can follow.

3.4.1 The model

Consider one of two membranes shown in Fig. 3.2, each with a mass m and characterised by an effective linear spring constant k_{eff} and a damping factor c. The motion of this system is characterised by a single degree of freedom $u = u(t)$, governed by Newton's law $f(t) = m\ddot{u}$. The force $f(t)$ is an externally applied "forcing function" that is time dependent. The viscous damper resists the velocity $\dot{u}$ with a force $c\dot{u}$. A compact description of the model would be that it is system where an externally applied force $f(t)$ is resisted by the sum of of three internal forces; the stiffness force $k_{eff}u$, damping force $c\dot{u}$ and inertial force $m\ddot{u}$. Newton's law yields.

$$f(t) = k_{eff}u + c\dot{u} + m\ddot{u} \tag{3.26}$$

Further, if the mass vibrates with a simple harmonic motion described by $u = \bar{u}\sin\omega t$, where u is the instantaneous amplitude of the motion, $\bar{u}$ the maximum amplitude and ω the natural angular frequency of the vibration, it can easily be shown that the undamped ω is

$$\omega = \sqrt{\frac{k_{eff}}{m}} \tag{3.27}$$

And if a damping c is considered, then

$$\omega = \omega_0\sqrt{1 - \zeta^2} \tag{3.28}$$
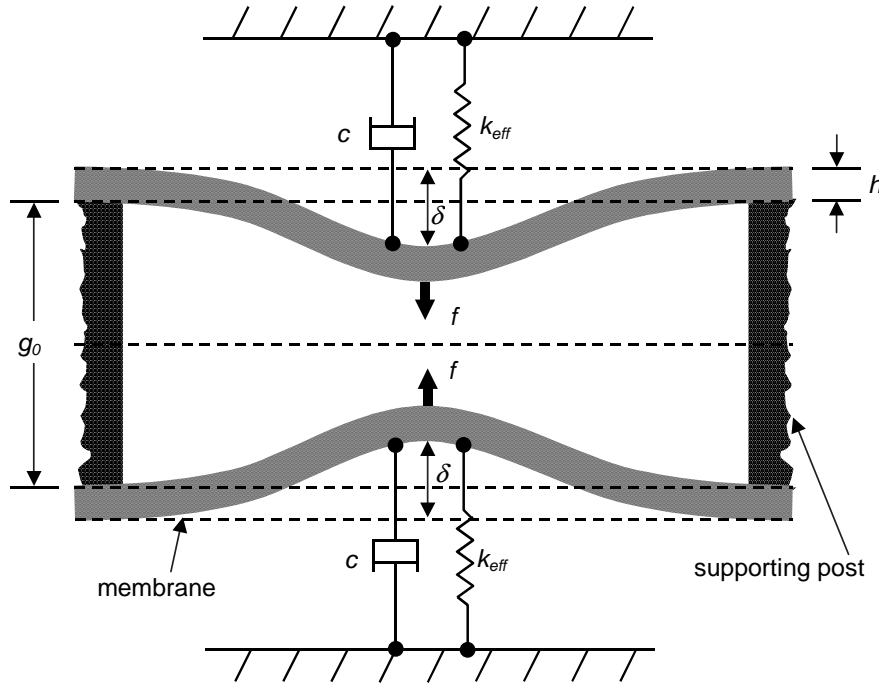
Fig. 3.2: Electro-mechanical model of the tunable filter system characterised by an effective linear spring constant k_{eff}, a damping factor c and an applied force f.

where ω_0 is the undamped natural frequency, ζ is the damping ratio given by $\zeta = c/c_{cr}$, c_{cr} is the critical damping factor determined as $c_{cr} = 2m\omega = 2\sqrt{k_{eff}\,m}$. Most models presented in the literature ignore the damping since the most important factor considered is the quasi-static response of the devices. However the influence of the damping is very important when considering the switching speed of devices or in the resonant frequency of resonators. Air damping is most profound as structures get smaller [93] hence an analysis of length scale air-damping effect is essential in determining the critical conditions under which a resonator might need to be vacuum encapsulated [94, 95]. Thus damping can be both friend and foe. In a switching situation, a certain amount of damping can cut down undesirable ringing in the system, but too much would cause longer switching times. For resonators the natural frequency can be severely shifted. In a previous study, we have demonstrated how the structural scaling affects the response time and transient behaviour of a tunable device in a low damping situation [96]. More about this is found in chapter 5.

3.4.2   Actual structure of the devices

The geometrical design configuration chosen for the devices consists of two DBRs separated by a resonant air micro-cavity. The DBRs consist of circularly-shaped membranes supported by 2, 3, or 4 suspensions. The suspensions are in turn mounted on supporting posts. Figure 3.3 depicts a scanning electron micrograph (SEM) of such a structure with 4 suspensions whereas Fig. 3.4 illustrates closer details of the membranes, suspensions and supporting posts of one DBR.
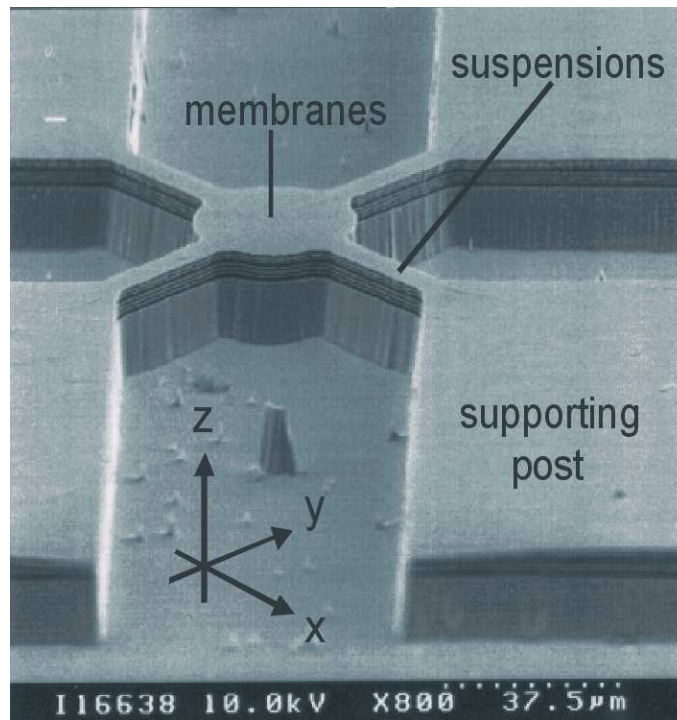
Fig. 3.3: Scanning electron micrograph of a multiple air gap filter with 30μm diameter membranes supported by four 30μm suspension sets which are in turn attached to four supporting posts (*xy*-plane is parallel to the wafer plane)[courtesy of J. Daleiden].

3.4.3   Determination of k_{eff}

The effective spring constant of a cantilever or a beam (bridge) structure with no in-built initial stress is known to have the functional form

$$k_{eff} \propto \frac{Eh^3\text{w}}{l^3} \qquad\qquad (3.29)$$
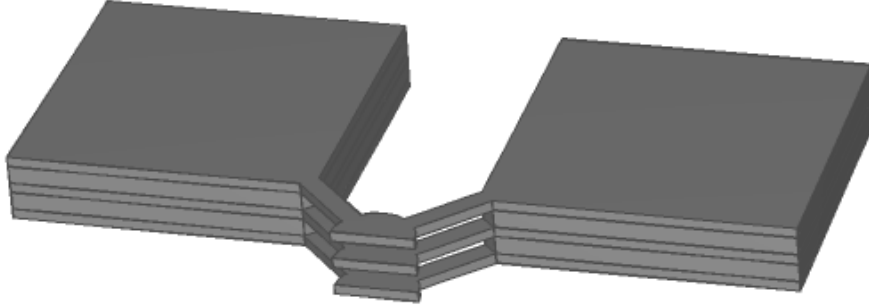
Fig. 3.4: Cutaway illustration showing close-up details of one DBR in the air-gap filter of Fig. 3.3 showing membranes, suspensions and supporting posts.

Extending this to the membrane problem, the effective spring constant can be taken to be of the form

$$k_{eff} = C_1 \frac{D\text{w}}{l^3} \tag{3.30}$$

where C_1 is a constant of proportionality, w and l the width and length of the structure, respectively and D the flexural rigidity of the membrane.

Applying Eqn. (3.27) above

$$\omega = \sqrt{C_1 \frac{D\text{w}}{l^3 m}} \tag{3.31}$$

First to be considered is the two suspension structure of Fig. 3.5. The overall effect of the added circular part to a beam structure of length $2(l + r)$ is to increase the stiffness and reduce the natural frequency, resulting in an effective decrease in the length. The effective length is taken to be

$$2l + \text{w}(1 + C_2\xi)$$

where $\xi = \frac{r - \text{w}/2}{\text{w}/2}$ and the constant C_2 determines the amount by which the addition of the circular membrane influences the stiffness of the beam structure without the circular membrane (i.e. when $r = \text{w}/2$).

The total area of the structure is given by

$$A_2 = 2(l + r)\text{w} + 2r^2 \cos^{-1}(\frac{\text{w}}{2r}) - \text{w} \sqrt{r^2 - \frac{\text{w}^2}{4}}$$

and mass $m = \rho h A_2$

$$\therefore \omega = \sqrt{C_1 \frac{Dw}{(2l + w(1 + C_2\xi))^3 \rho h A_2}}. \tag{3.32}$$

The values of C_1 and C_2 are obtained by fitting eigenvalues generated from FEM calculations. Similar derivations were carried out for 3- and 4- suspension structures. The results are summarised in Table 3.1
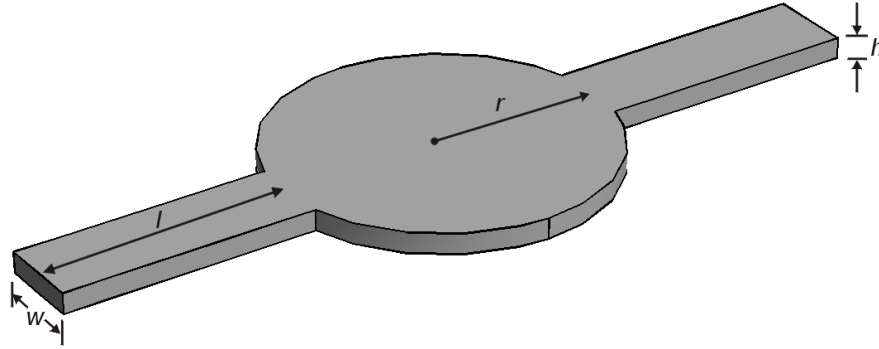
Fig. 3.5: Structural configuration and dimensional parameters of a two-suspension membrane indicating membrane radius r, suspension length l, suspension width w and membrane thickness h.

3.4.4 Determination of range of stable operation

Now consider the coupled electro-mechanical system in quasi-static equilibrium ($\dot{u} = \ddot{u} = 0$) with a deflection $u = \delta$,

$$
\begin{aligned}
f_{mechanical} &= f_{electrostatic} \\
k_{eff}\delta &= \frac{\varepsilon_0 V^2 A}{8(\frac{g_0}{2} - \delta)^2}
\end{aligned} \tag{3.33}
$$

No. of Suspensions	k_{eff}
2	$47\frac{Dw}{(2l+w(1+0.87\xi))^3}$
3	$72\frac{Dw}{(2l+w(1+0.26\xi))^3}$
4	$108\frac{Dw}{(2l+w(1+0.67\xi))^3}$

Table 3.1: Effective spring constants for 2- 3- and 4- suspension filter configurations.

Rearranging this equation results in

$$8k_{eff}\delta(\frac{g_0}{2} - \delta)^2 - \varepsilon_0 V^2 A = 0 \tag{3.34}$$

This is a third order polynomial in δ, which implies that for every value of V, there exist three values of δ i.e. three equilibria for each V. Solving Eqn. (3.34) with the aid of a Matlab program for one of the structures, the plot in Fig. 3.6 was obtained.
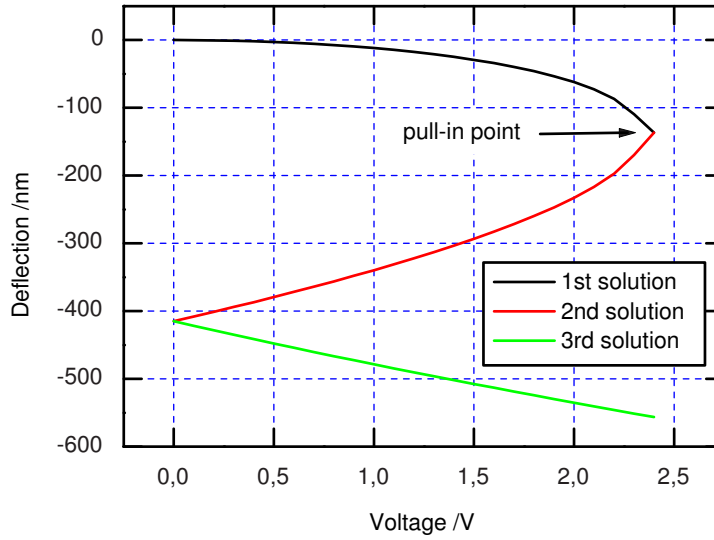
Fig. 3.6: Calculated voltage vs deflection characteristics for a $3\lambda/4$ InP filter membrane with four $40\mu m$ long, $10\mu m$ wide suspensions and a $40\mu m$ diameter membrane.

The lower part of the plot, however, portrays unstable equilibrium (2nd and 3rd solutions). This can be seen from the following by analysing the net force;

$$f_{net} = k_{eff}\delta - \frac{\varepsilon_0 V^2 A}{8(\frac{g_0}{2} - \delta)^2} \tag{3.35}$$

Differentiating with respect to δ

$$\partial f_{net} = \left. \frac{\partial f_{net}}{\partial \delta} \right|_V \partial \delta$$

$$= \left(k_{eff} - \frac{\varepsilon_0 V^2 A}{4(\frac{g_0}{2} - \delta)^3} \right) \partial \delta \tag{3.36}$$

Stability requires that $\partial f_{net} < 0$. The edge of the stable region is defined by $\frac{\partial f_{net}}{\partial \delta} = 0$ which yields

$$\delta_{PI} = g_0/6 \tag{3.37}$$

The maximum voltage for stable operation is therefore given by

$$V_{PI} = \left. \sqrt{\frac{8\delta k_{eff}}{A\varepsilon} \left(\frac{g_0}{2} - \delta \right)} \right|_{\delta = g_0/6}$$

$$= \sqrt{\frac{4g_0^3 k_{eff}}{27A\varepsilon}} \tag{3.38}$$

It can also be similarly shown that when only one of the two membranes is actuated against a fixed reference (ground), then

$$V_{PI} = \sqrt{\frac{8g_0^3 k_{eff}}{27A\varepsilon}} \tag{3.39}$$

The voltage V_{PI} is known as the "pull-in" or the "snap-down" voltage. When the voltage is increased beyond this point the membranes are accelerated towards each other, which may result in a possible catastrophic breakdown. Pull-in instability occurs as a result of the fact that the electrostatic force increases non-linearly with decreasing gap, whereas the spring constant force is a linear function of change in gap spacing. Pull-in can, in simple terms, be defined as the voltage at which the restoring spring force no longer balances the attractive electrostatic force. A plot of the forces versus deflection is given in Fig. 3.7.
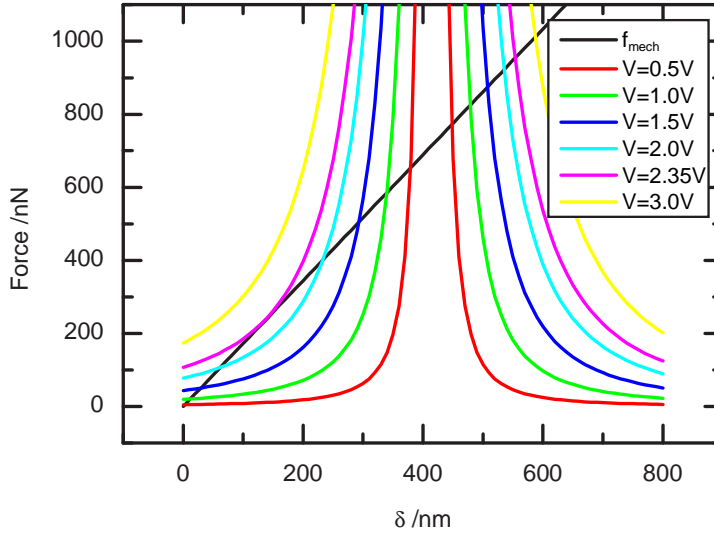
Fig. 3.7: Calculated mechanical and electrostatic forces vs deflection for a $3\lambda/4$ InP filter membrane with four 40μm long, 10μm wide suspensions and a 40μm diameter membrane. Note that when $V = V_{PI} = 2.35$V, there is only one unstable solution on left hand side of plot.

3.5 Choice of material system and geometrical dimensions

3.5.1 Material system

The criterion for the choice of the DBR material was given in section 2.1.4 where the illustration presented was for the InP/air. Other material systems are possible too. The important parameter for the material system is the refractive index contrast, Δn. The larger the Δn, the larger the reflection band for a given wavelength and cavity length. Hence the possible tuning range will also be large. It has also been shown in [73] that given a DBR filter grown on a substrate of refractive index n_s with x layers of $\lambda/4$ thick refractive index (n_2) material and with a cavity length of $m\lambda/2$ consisting of the low refractive index (n_1) material, the finesse of the filter is given by

$$Finesse = \frac{m\pi n_2^{2x}}{4 n_1^{2x-1} n_s} \qquad (3.40)$$

Other material systems that can be used are: SiO_2/Si, Si_3N_4/SiO_2, GaAs/AlAs, e.t.c. A further choice criterion is whether semiconductor or dielectric material system.

The important geometrical design parameters are thickness of the central membrane and suspensions, cavity size (and possible tuning range), diameter of central membrane, and length, width and number of suspensions.

3.5.2 Thickness of the membrane and suspensions

This is automatically determined by the DBRs. In the technological realisation process the layers of the DBRs are grown one on top of the other. Sacrificial layers are used where air gaps are needed. These are eventually etched away. Factors determining the DBR dimensions were given in section 2.4.2. The technological realisation process can also limit the the size of the DBRs. For instance, quarter wavelength thick InP layers are in the order of 100nm for communication wavelengths. Micromachining of such structures is still a challenging technological task, therefore three quarter wavelength thick layers are often used instead.

3.5.3 Cavity length and tuning range

The criterion for the choice of the cavity length was introduced in section 2.1.3. It was deduced that the cavity length for a Fabry-Pérot filter must be a multiple of half the resonant wavelength. It is also seen in Fig. 2.5 that the larger the cavity length the smaller the FSR, which is in many cases not desired. For this work, the cavities used were in the order of half the reference communication wavelength (1.55μm). The length of the cavity also determines the maximum tuning range of a parallel capacitor type electrostatically tuned Fabry-Pérot filter. As was shown in section 3.4.4, the pull-in point occurs at around one third of the cavity length. This implies that the maximum theoretically possible electromechanical tuning range is one third of the cavity length. Other tricks, however, have been devised to extend this range [23, 97, 98, 99, 100].

3.5.4 Diameter of central circular membrane

Two criteria are important for the choice of the diameter of the central circular membrane. One is the size of the input or output coupling point, for instance, to an optical fibre. Different wavelengths have different spot sizes, it is therefore necessary to choose a diameter

of the membrane that is at least the size of the largest spot size. The second is the diffraction loss. The diffraction loss can be intuitively be thought of as the fraction of the optical power that miss the mirror surface. This can be estimated by borrowing from the confocal resonator. For such a resonator with mirrors of diameter d and separated by a distance L, the relevant parameter used to determine the diffraction loss is the Fresnel number given by [101]

$$N_F = \frac{d^2}{4L\lambda} \tag{3.41}$$

The normalised power loss per mirror for the fundamental mode in terms of the Fresnel number is given by

$$\alpha_d = 16\pi^2 N_F e^{-4\pi N_F} \tag{3.42}$$
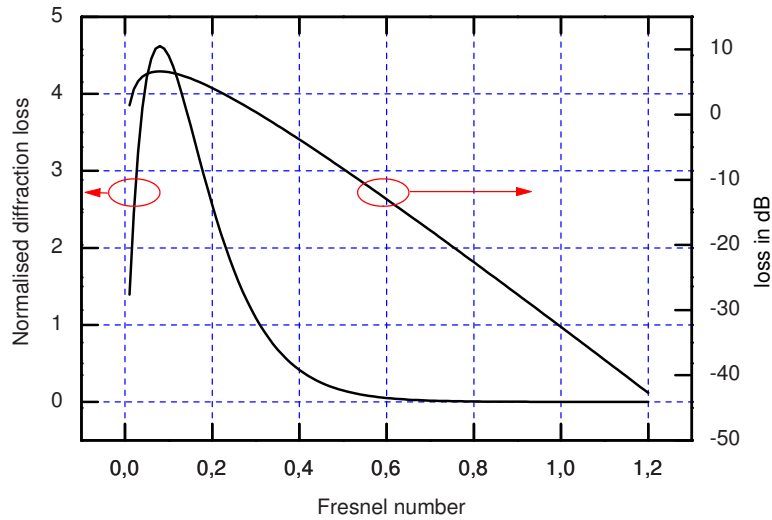
Fig. 3.8: Plot of normalised diffraction loss versus Fresnel number N_F for a confocal mirror for range of N_F between 0 and 1.2.

The plot of Fig. 3.8 shows that a sufficiently small diffraction loss is obtained for values of N_F around 1. Taking N_F as 1, $\alpha_d = 5.507e - 4$ or $-32.59dB$. For this, the minimum membrane diameter will be given from Eqn. (3.41) by

$$d_{min} = 2\sqrt{L\lambda} \tag{3.43}$$

A reasonable approximation for d_{min} can be obtained by using a value of λ located at the upper edge of the stop-band. The width of the stop-band in terms of the reciprocal wavelength is given by [76]

$$\Delta\left(\frac{1}{\lambda_B}\right) = \frac{4}{\pi\lambda_0}\sin^{-1}\left(\frac{n_2 - n_1}{n_2 + n_1}\right) \tag{3.44}$$

where $\Delta\lambda_B$ = stop-band width, λ_0 is the reference wavelength and the band edges occur at

$$\left\{\frac{1}{\lambda_0} \pm \frac{1}{2}\left(\frac{1}{\lambda_B}\right)\right\}^{-1}$$

The upper band edge is therefore given by

$$\begin{aligned}
\left\{\frac{1}{\lambda_0} - \frac{1}{2}\left(\frac{1}{\lambda_B}\right)\right\}^{-1} &= \left\{\frac{1}{\lambda_0} - \frac{2}{\pi\lambda_0}\sin^{-1}\left(\frac{n_2 - n_1}{n_2 + n_1}\right)\right\}^{-1} \\
&= \frac{\pi\lambda_0}{\pi - 2\sin^{-1}\left(\frac{n_2 - n_1}{n_2 + n_1}\right)}
\end{aligned} \tag{3.45}$$

Now combining Eqn. (3.43) and (3.45)

$$d_{min} = 2\sqrt{\frac{L\pi\lambda_0}{\pi - 2\sin^{-1}\left(\frac{n_2 - n_1}{n_2 + n_1}\right)}} \tag{3.46}$$

When $L = n\lambda/2$, $(n = 1, 2, ...)$, the case for FP filter

$$d_{min} = \lambda_0\sqrt{\frac{2\pi n}{\pi - 2\sin^{-1}\left(\frac{n_2 - n_1}{n_2 + n_1}\right)}} \tag{3.47}$$

This equals 2.7μm for a reference wavelength of 1.55μm, $n = 1$ (half lambda cavity), $n_1 = 1$ (air) and $n_2 = 3.15$ (InP). For the cases considered here the membrane diameters were many times larger than this limit. Nevertheless, when scaling is applied it is prudent to bear this in mind. As a side observation Eqn. (3.45) gives the dependence of the stop-band width on the refractive index contrast. For a given reference wavelength, the larger the the contrast, the wider the stop-band.

3.5.5 Length, width and number of suspensions

One has a rather free hand in choosing the filter configuration based on the number of suspensions. However, a few factors are worth noting; the end application requirements, the technological realisation processes and configuration stability and performance. For instance, the two suspension structure is mechanically the least stable. It has been observed in both simulation results (Fig. 3.9) and scanning electron micrographs of such structures that the membranes exhibit severe warping especially when the suspension width is much smaller than the diameter, an effect that is optically not desirable. The three suspension structure is probably the most mechanically stable, having the inherent stability of a three point suspended structure. The membranes in both three and four suspension structures do not exhibit a lot of warping.
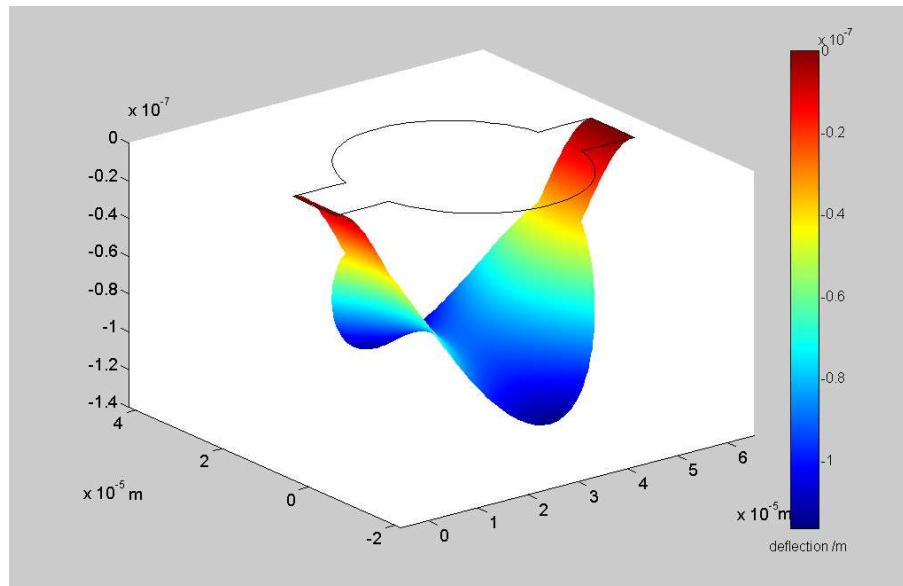
Fig. 3.9: Illustration of the warpage of an actuated 2-suspension structure done using the 2D (Quasi-3D) FEM program. The membrane distortion is more often an undesired effect.

As for the width of the suspensions, the upper limit is the diameter of the central circular membrane. The lower limit should take the technological realisation process, mechanical strength and warpage into account. Too small width suspensions might be difficult or impossible to realise as well as being fragile.

Lastly, after choosing all the above dimensional parameters, the only remaining and very important parameter is the suspension length. The reasonable factor to consider here is the fundamental natural frequency of oscillation. Eqn. (3.32) and Table 3.1 can be

applied in this respect. For a desired chosen frequency bound, the only unknown in the equation will be the suspension length.

Alternatively, a desired pull-in point can be selected as the factor used in determining the suspension length. In this case Eqn. (4.22) would be applied for this purpose.

3.6 A design example

Reference wavelength: λ = 1550nm

Material system: InP/air

Material Parameters: InP [102]; E=6.11e10 MPa, ν = 0.36, ρ=4790 kg/m^3, n = 3.15, n(air)=1

Layer thickness: $3\lambda/4$ (InP), $\lambda/4$ (air)

Cavity length: 830nm

Diameter: d_{min} = 2.7μm from Eqn. (3.47), chosen diameter = 40μm.

Number of suspensions: 4

Suspension width: 10μm (realisable technologically)

Suspension length: For a fundamental natural frequency of 100 MHz or a pull-in voltage of around 2.5V, the suspension length will be of the order of 40μm.

The results of the analytical plot and the 2D and 3D FEM simulations plots are seen in the graph of Fig. 3.10. All three agree extremely well, showing that the analytical model derived can be reliably applied in the design of stress-free devices. A crucial observation here is that the pull-in point is higher than the value predicted by Eqn. (3.37). This is investigated in the following.

3.7 Study of the effect of geometrical dimensions on tuning and pull-in point

The investigation presented below were carried out using the FEM models described earlier on. The 2D and 3D calculations gave identical results. The 2D calculations had the advantage of speed.
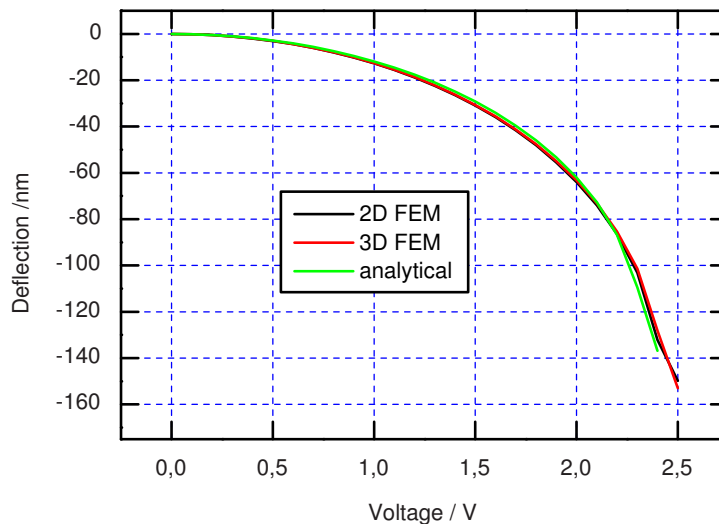
Fig. 3.10: Comparison of the derived analytical function with 2D and 3D FEM output for a $3\lambda/4$ InP filter membrane with four 40μm long, 10μm wide suspensions and a 40μm diameter membrane.

3.7.1 Deflection vs voltage characteristics

In this section is a sampling of the deflection vs voltage characteristics for various configurations of the devices under investigation.

Figure 3.11 gives the results of deflection change with voltage as the number of suspensions is varied, all other geometrical parameters kept constant. It is observed that as the number of suspensions rise, more voltage is needed to produce the same deflection. A rather obvious explanation for this is that the stiffness of the structure increases with the number of suspensions and given that the size of the circular membrane, where most of the deflecting force is concentrated, remains unchanged, there will be less deflection with more suspensions.

Presented in Fig. 3.12 are the changes in the deflection characteristics with the suspension length. It is seen that all else kept constant, the stiffness of the structures reduces with increase in suspension length.

The increase in the membrane radius has the effect of increasing the area on which the electrostatic force acts. Less voltage is therefore needed to produce a given deflection with a higher radius. This effect is illustrated in Fig. 3.13.
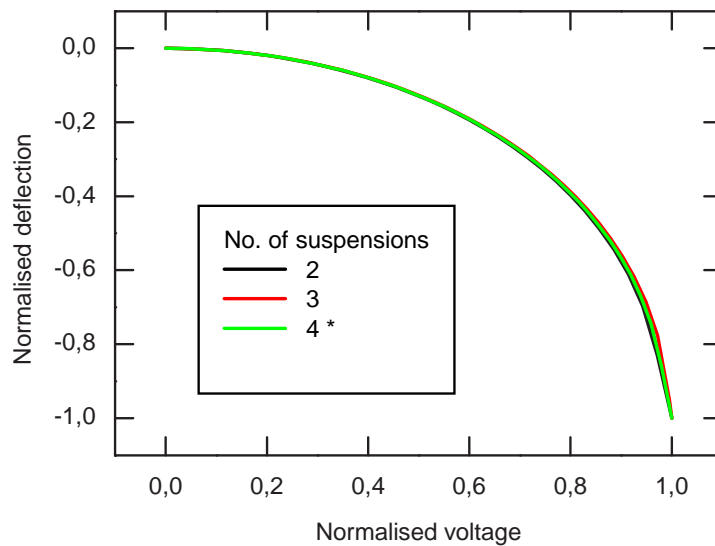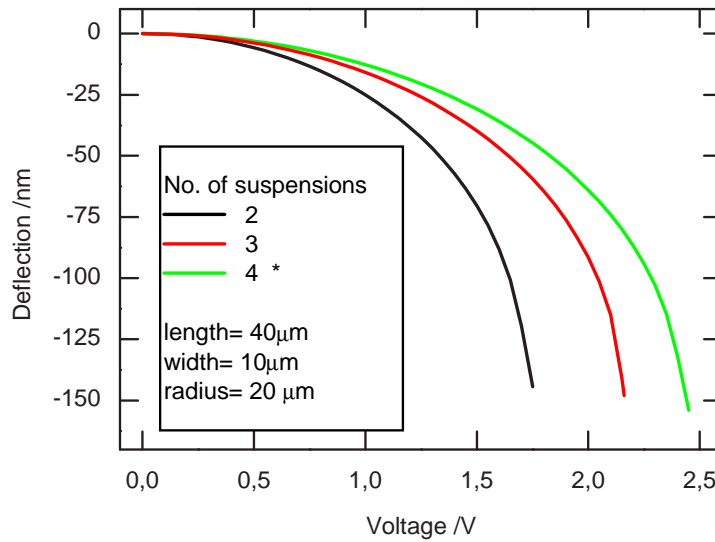
Fig. 3.11: Deflection vs voltage characteristics for structures with different numbers of suspensions. The asterisk marks the 4-suspension structure that is common in all the results in the following three figures. In the bottom plot, each of the three characteristics is normalised to its pull-in deflection and voltage.
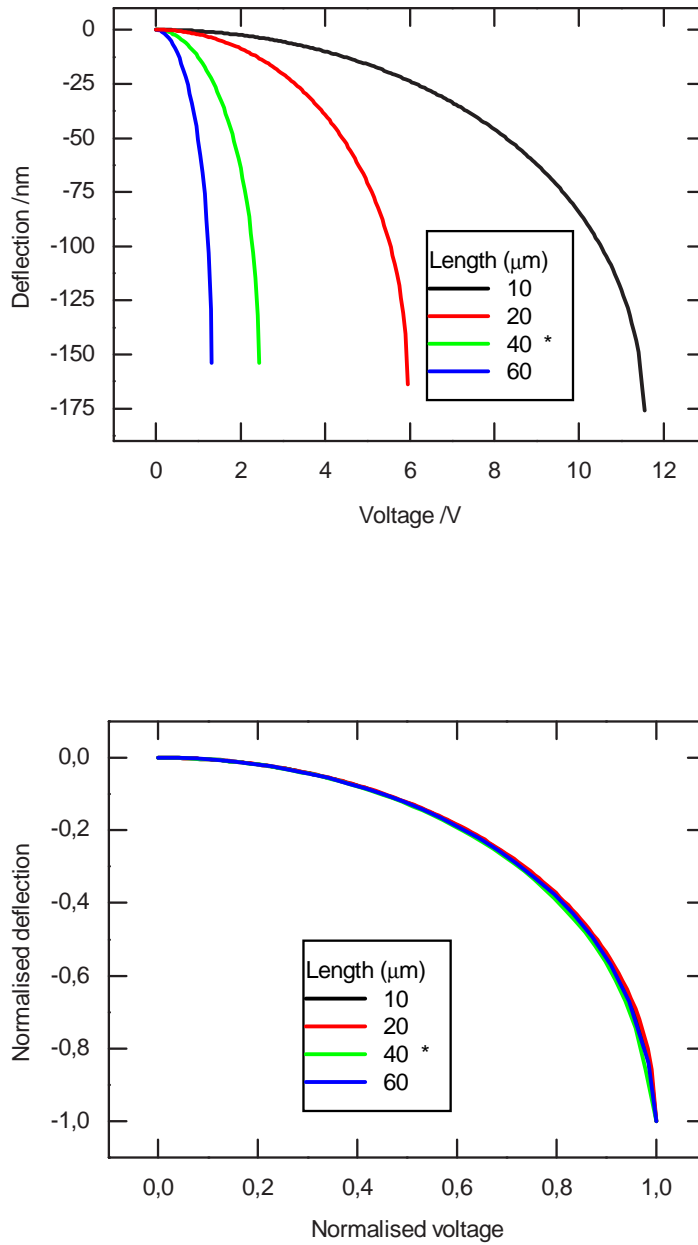
Fig. 3.12: Deflection vs voltage characteristics showing the effect of changing suspension length. The asterisk marks the 4-suspension structure that is common in all the results in this section. In the bottom plot, each of the three characteristics is normalised to its pull-in deflection and voltage.
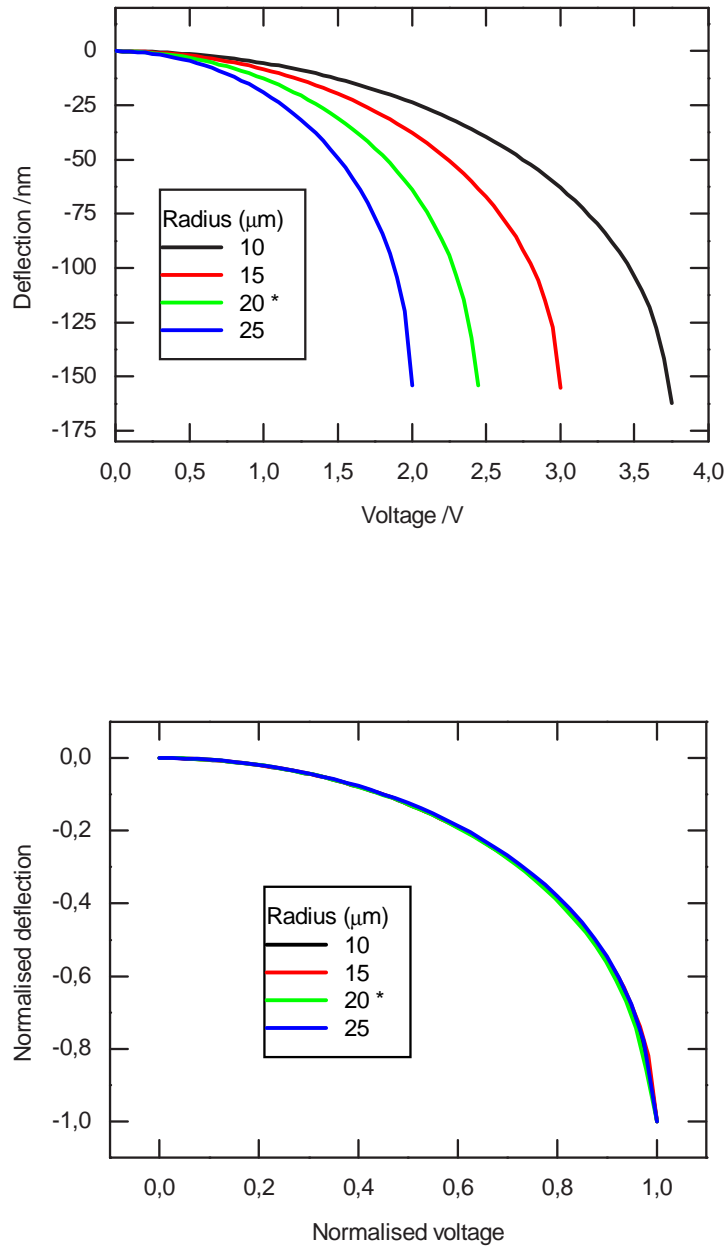
Fig. 3.13: Deflection vs voltage characteristics showing the effect of changing membrane radius. The asterisk marks the 4-suspension structure that is common in all the results in this section. In the bottom plot, each of the three characteristics is normalised to its pull-in deflection and voltage.

Finally, the effect of increasing the suspension width is seen in Fig. 3.14. For the four suspension structure investigated here, the width was increased to the maximum possible value for the membrane radius considered. For a 2 suspension structure, the maximum attainable suspension width is $2r$. For 3 suspensions, $r\sqrt{3}$ and for a four suspension structure it is $r\sqrt{2}$. It is observed in the diagram that the effect of the increase in suspension width is to increase the structure stiffness.

For each of the deflection characteristics above, the last point is the pull-in point. It is observed that as the structures change so does the pull-in point. That is to say that the pull-in point is not the constant predicted by the commonly used relation in Eqn. (3.37). This effect is given further treatment in the next section.

For each of the characteristics a normalised characteristic was plotted. The normalisation was done by dividing the deflection values by the deflection at the pull-in point for each case, and the voltage was normalised to the corresponding pull-in voltage. The results are seen alongside each of the characteristic plots. The structure marked with a star in the plots is the same for all the cases.

A very intriguing observation was made from the normalised plots. This was that regardless of the geometrical configuration and structural size variations, the normalised deflection characteristic has exactly the same form. This has the useful consequence that for any of these structures, the knowledge of the pull-in point deflection and voltage gives all the information that one might need about the deflection characteristic. In the next chapter, an attempt is made to derive a more accurate analytical model for such a purpose. But before that, the pull-in point behaviour follows below.

3.7.2   Pull-in variation with geometry

This section presents the results of the FEM investigation of the effect of the variation of the geometry configuration on the pull-in point. Starting with Fig. 3.15, it is observed that in general, the pull-in point is higher than that predicted by the simple analytical expression of Eqn. (3.37). It is also noted that for shorter suspension lengths, the pull-in point is further from the predicted value than for longer suspensions. A possible explanation for this observation is that the structures exhibit stress stiffening, which means that the effective spring constant increases with the bending. As a result the point of equilibrium of mechanical and electrostatic forces therefore shifts to higher values with increasing deflection. Further, for the same amount of deflection, the shorter length will have a smaller radius of curvature compared to the structure with the longer suspensions. The smaller
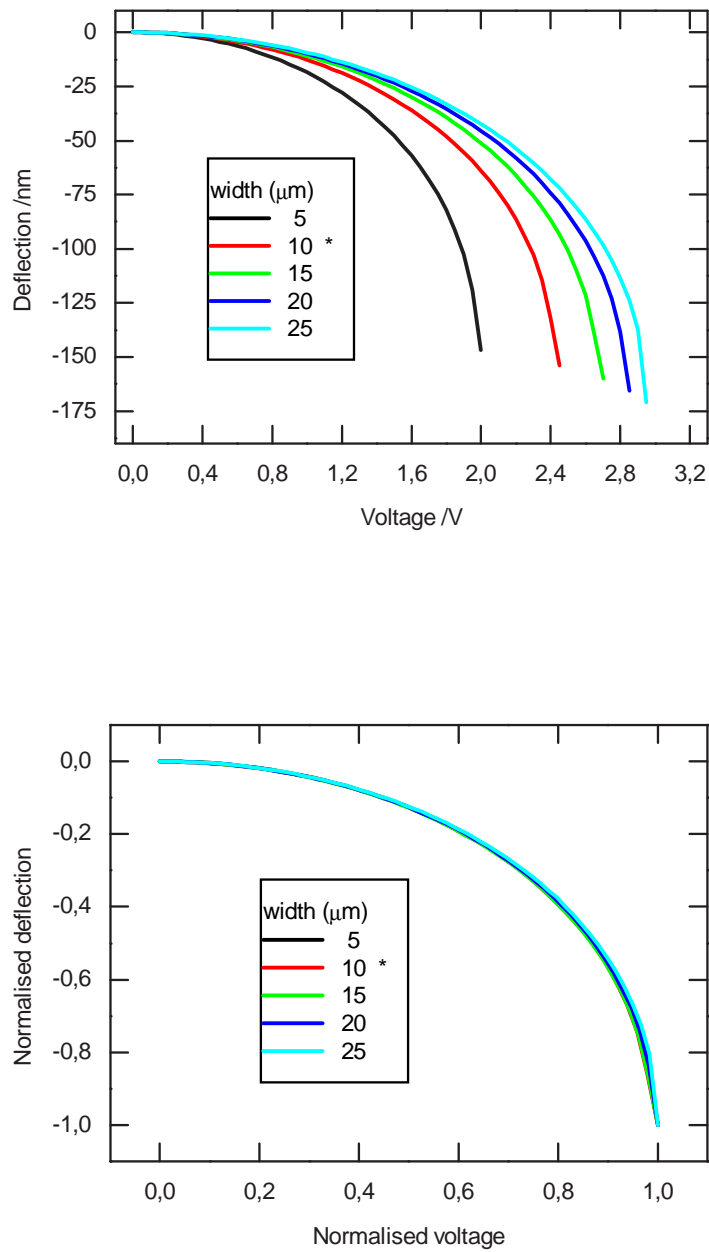
Fig. 3.14: Deflection vs voltage characteristics showing the effect of changing suspension width. The asterisk marks the 4-suspension structure that is common in all the results in this section. In the bottom plot, each of the three characteristics is normalised to its pull-in deflection and voltage.

radius of curvature implies more bending stress, hence relatively more stress stiffening. This explains why the pull-in point for shorter suspension is higher. The inability to obtain smooth plots for the pull-in point was due to the fact that many fine FEM iterations are required to achieve smoothness. This can be extremely time consuming. However, the trends are clearly seen in the plots, the roughness notwithstanding.

The pull-in voltage plots can be explained in a similar way. The longer structures have lower effective spring constants as can be seen in Eqn. (3.30). The shorter structures will on the contrary exhibit higher spring constants which is further enhanced by the stress stiffening effect. Hence, pull-in voltages get higher and higher with reducing length.

Another interesting observation is made in Fig. 3.16. It is noticed that for short suspensions, the stiffness seems to increase with the increase in radius and vice versa for long suspensions. A plausible explanation for this would be as follows: That most of the bending stress occurs in the suspensions. For a given short suspension and small radius, a higher voltage is needed to attain a given deflection, so the bending stress will be relatively high in the circular membrane as well. For the same short suspension and larger circular membrane, a lower voltage is needed to attain the same deflection, and the bending stress is relatively lower in the central membrane. The stress stiffening in the suspensions is therefore relatively higher than in the case before, resulting in a net higher spring constant.

As for the longer suspensions, the stress stiffening effect is not severe as the relative bending of the suspensions is smaller. The effect of increasing membrane radius is therefore more to increase the effective length of the suspension than to cause higher bending stiffness. The total radius of curvature increases with the membrane diameter. This results in a net decrease in stiffness with increasing diameter, which manifests itself as lower pull-in points. A more elaborate investigation of the stress profile that causes the stiffening effect is presented in the next section.

The next investigation involved the variation of pull-in with width of the suspensions. In this case the plots given in Fig. 3.17 are for the variation with relative width. This is presented in this form since the maximum width attainable depends on the radius, r of the membrane as stated in the previous section, that is $2r$ for a 2 suspension structure, $r\sqrt{3}$ for 3 suspensions and $r\sqrt{2}$ for a four suspension structure. The width is therefore normalised with respect to the maximum width attainable.

An average length of 30μm was used for this investigation. It is observed that the stiffness increases with the width as seen in the movement of the pull-in point away from the ideal. The pull-in voltage also increases accordingly. At very small widths, the pull-in
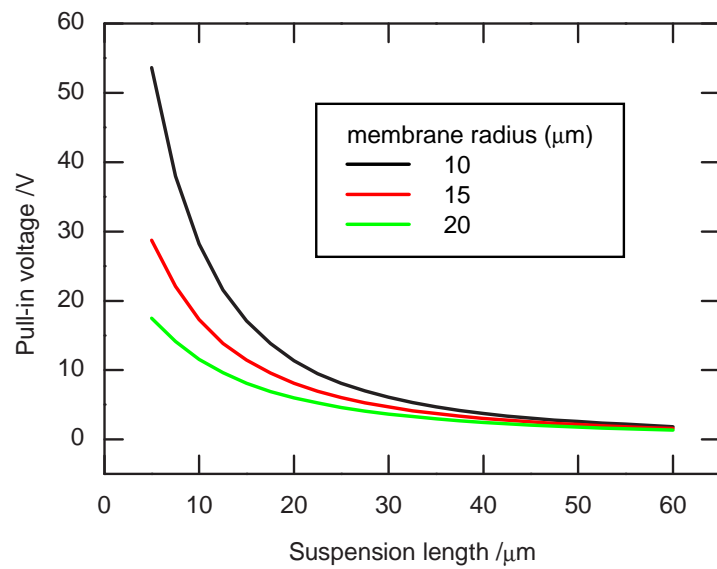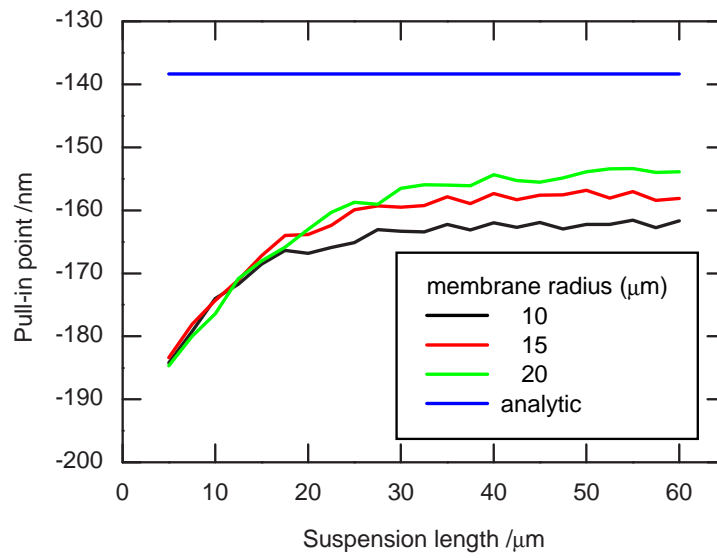
Fig. 3.15: Variation of pull-in deflection (top) and pull-in voltage (bottom) with suspension length calculated using the quasi-3D FEM method.
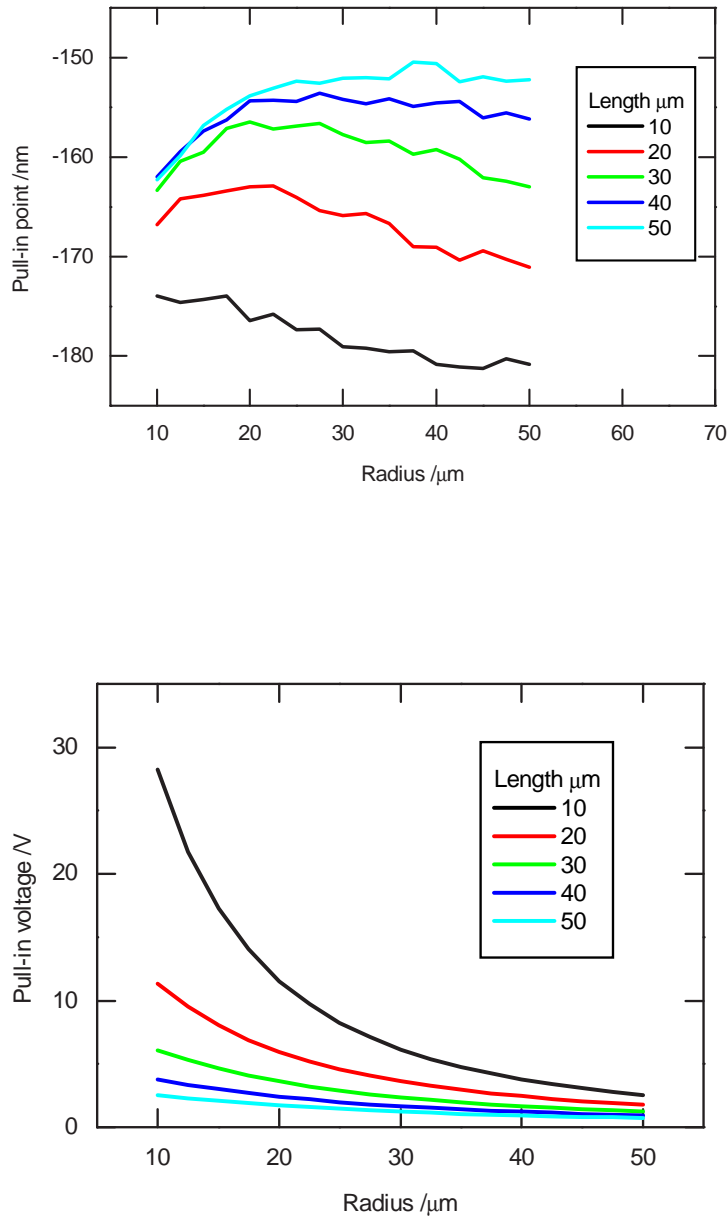
Fig. 3.16: Variation of pull-in deflection (top) and pull-in voltage (bottom) with membrane radius calculated using the quasi-3D FEM method.
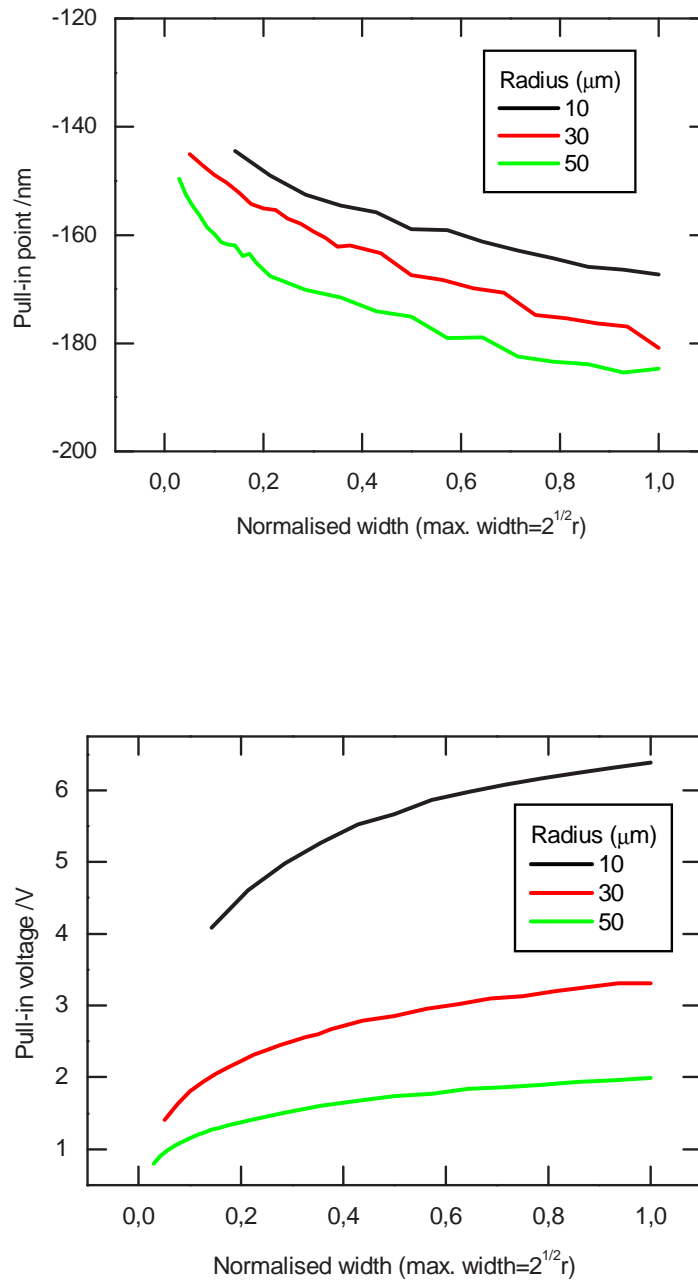
Fig. 3.17: Variation of pull-in deflection (top) and pull-in voltage (bottom) with normalised suspension width using the quasi-3D FEM method.

point is very close to the ideal, reflecting very small amounts of stress stiffening effect.

3.7.3   A closer look at stress distribution and bending profiles

Reference is made above to "stress stiffening effect". The term "stress stiffening" refers to the coupling between membrane stress and the out-of-plane displacement associated with bending [64]. The effective bending stiffness of a membrane is modified by the in-built stress. This stress results from an applied external force, as seen in this chapter, and/or from internal residual stress, as will be presented in the next chapter. Tensile membrane stress has the effect of increasing the effective bending stiffness, and vice versa for compressive stress. When the compressive stress is large enough to reduce the effective bending stiffness to zero, the structure buckles. This is an effect that is commonly observed in thin-walled structures.

An interesting observation has been made above in Fig. 3.16 where the pull-in point was seen to be higher for short suspension length structures than for the longer suspension structures. This was attributed to presence of higher amounts of stress stiffening, which seemed to increase with radius for short suspensions and decrease for long suspensions.

In Fig. 3.18 the variation of the maximum von Mises [1] membrane stress for various structures at pull-in point is presented. This diagram in deed confirms the earlier proposed explanation that the shorter suspensions and smaller radius experience highest stress stiffening. To better understand the nature of this effect, it is important to know the nature of stress distribution as well as the bending profile in the various structures. In Fig. 3.19 to Fig. 3.22 four extreme structures have been chosen. These diagrams show the profiles of stress and the deflection taken from the centre of the membrane to the end of the suspension.

A deeper insight is provided in Fig. 3.23 where the relative stress and deflection profiles are plotted side by side. It is observed that for the structure with short suspension and large radius, the stress in the suspensions is relatively more than in in central membrane as compared to the structure with short suspension and large radius. Therefore, even though the maximum stress decreases with increase in radius, the proportional increase in the

---

[1]von Mises stress is an invariant stress quantity, i.e. it has the same value in any coordinate system. It is defined as

$$\sigma_{vM} = \frac{1}{\sqrt{2}} \left[(\sigma_1 - \sigma_2)^2 + (\sigma_2 - \sigma_3)^2 + (\sigma_3 - \sigma_1)^2 \right]^{1/2}$$

where σ_1, σ_2 and σ_3 are the three principle stresses at the reference point, with σ_1 algebraically the largest and σ_3 the smallest
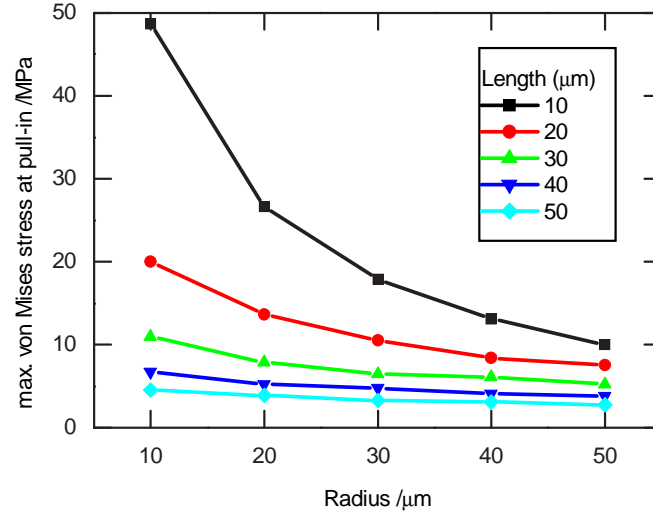
Fig. 3.18: Calculated maximum von Mises stress at pull-in point for various structural configurations. Structures with shorter suspensions and smaller radii exhibit higher stress.

suspensions causes an increase in stress stiffening. For the structures with longer suspensions, this proportional increase is not large, therefore the effect of increase in effective length is dominant, hence a sum reduction in effective stiffness.

As for the membrane deflection profile, Fig. 3.23 shows that if central membrane distortion is to be kept to a minimum, then the best choice would be a structure with long suspensions and small membrane diameter. This structure has a second possible advantage of needing comparatively low actuation voltage. A possible disadvantage would be that the stress stiffening effect is low in this structure, hence the extended range of travel due to stress stiffening is lower than for sort suspensions. The worst choice, as far as membrane distortion is concerned, is the structure with short suspensions and a large central membrane diameter.

3.7.4   Summary

Several important results have been presented in this chapter. First, closed form expressions for the effective membrane stiffness were derived for 2, 3 and 4-suspension structures by fitting data derived from FEM computations. The expressions showed extremely good agreement with FEM results when used to determine the first mode eigen-
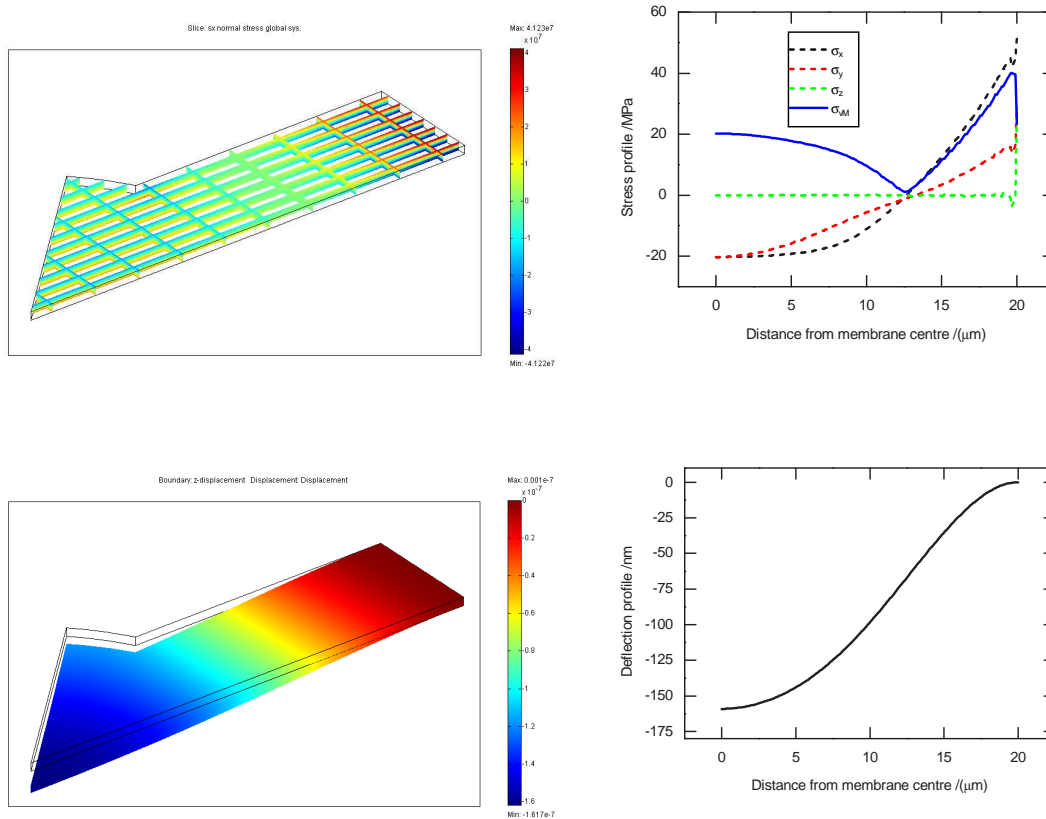
Fig. 3.19: Stress distribution and deflection profile for a structure with $10\mu m$ suspension and $10\mu m$ membrane radius. The 3D FEM output on the left show the one eighth of the 4 suspension structure considered.

frequencies and voltage-deflection characteristics. These can be invaluable tools for providing insight into device behaviour at the beginning of the design phase. A systematic design procedure is proposed, which is to be used in combination with the analytic model.

The normalised deflection-voltage characteristics provided a stunning revelation. That regardless of the structural configuration and geometrical dimensions, the normalised deflection-voltage profile is always the same. This has the important consequence that the tuning characteristic of a given structure is sufficiently defined by the pull-in point deflection and voltage.

Further, a study of the pull-in point reveals an extended range of travel caused by the stress stiffening effect. In addition an analysis of the amount and distribution of the induced stress in the structures at the pull-in point provides a good understanding of the pull-in point variation observed.
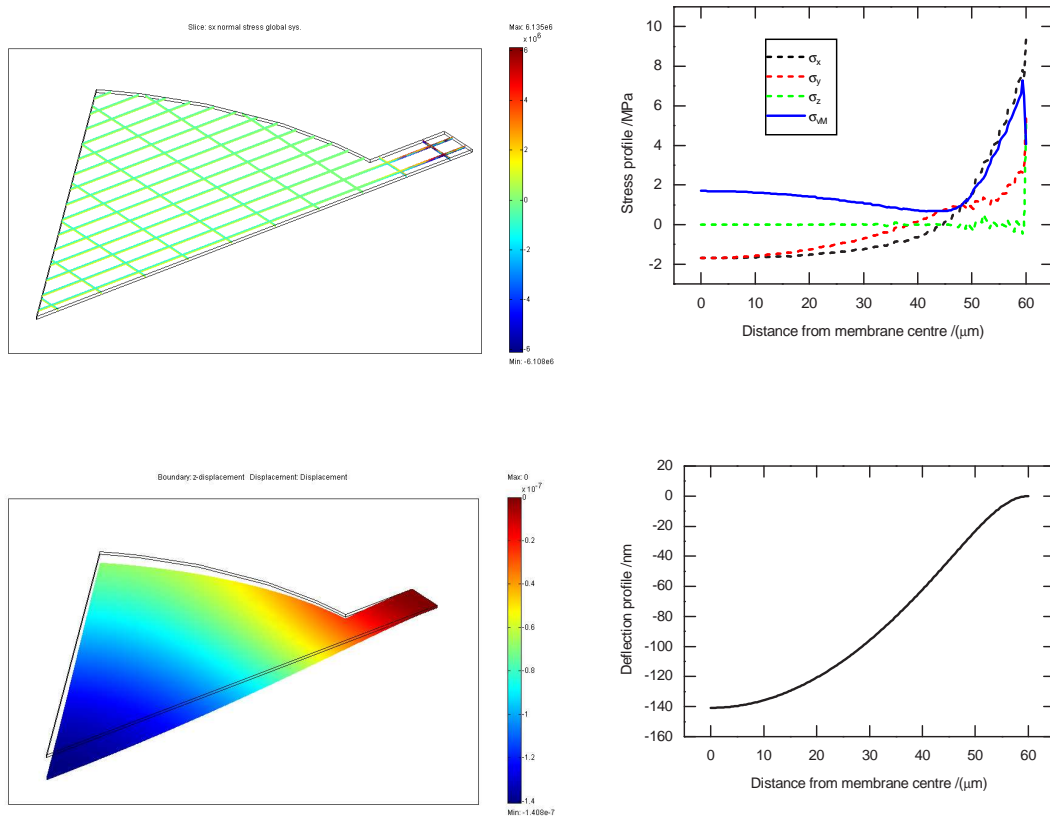
Fig. 3.20: Stress distribution and deflection profile for a structure with 10μm suspension and 50μm membrane radius. The 3D FEM output on the left show the one eighth of the 4 suspension structure considered.

Finally, an analysis of the membrane deflection profiles at the pull-in point shows the effect of the geometrical variations on the central membrane distortion, an effect that is often not desired.

All the above computations exclude effects of uniform and gradient axial residual stress. These results are valid for cases where these effects are minimal i.e. where residual stress is limited to an insignificant amount in the material through suitable technological processes.

However, in the course of the entire project, it was often observed that the residual stress in the membranes of the devices had a profound effect, causing out-of-plane deformations and modifying the mechanical behaviour of the materials. This problem is dealt with in the next chapter.
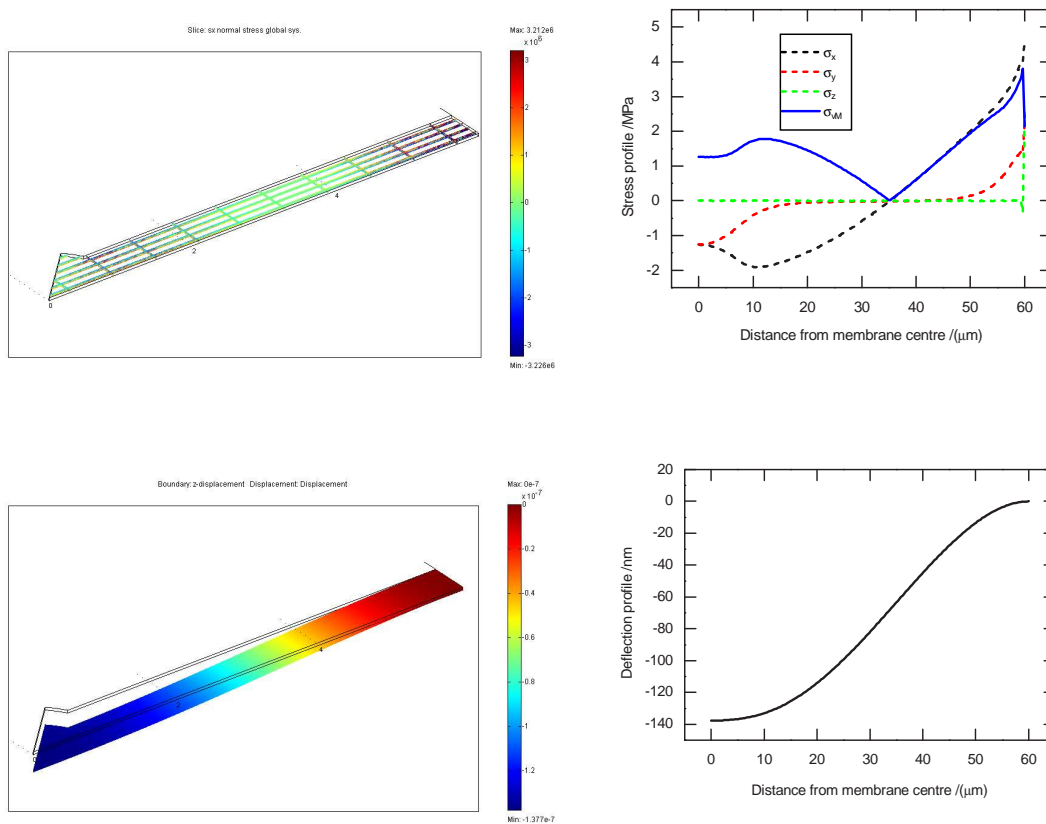
Fig. 3.21: Stress distribution and deflection profile for a structure with 50μm suspension and 10μm membrane radius. The 3D FEM output on the left show the one eighth of the 4 suspension structure considered.
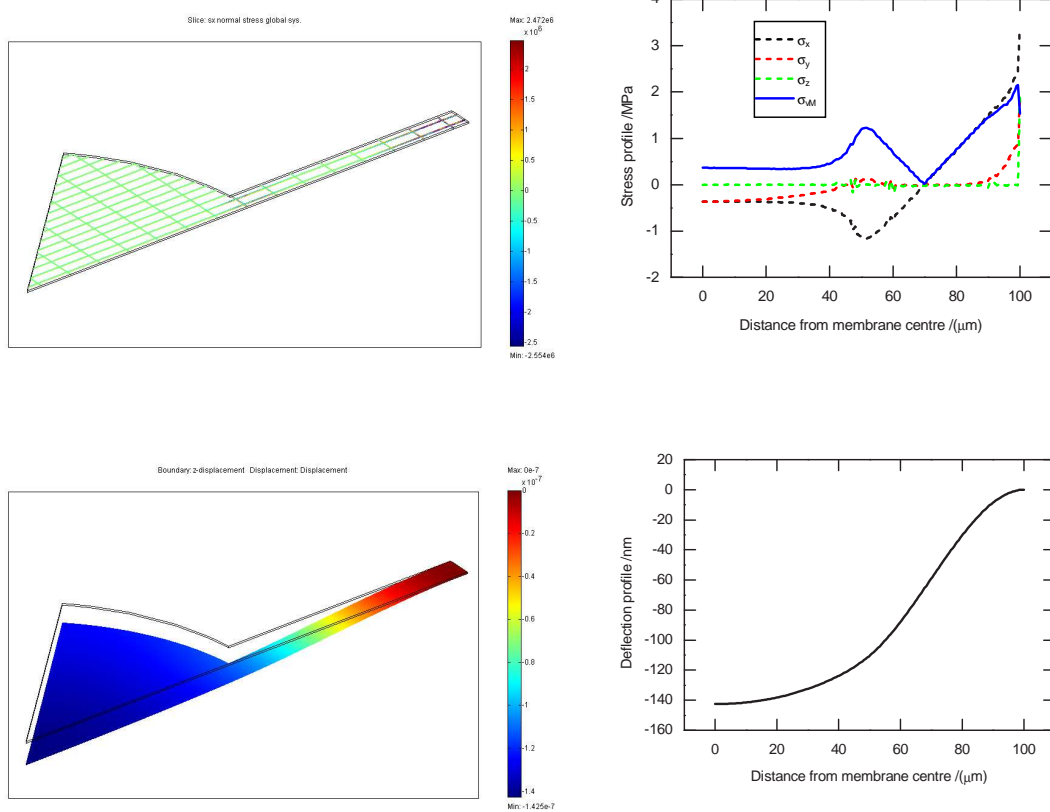
Fig. 3.22: Stress distribution and deflection profile for a structure with 50μm suspension and 50μm membrane radius. The 3D FEM output on the left show the one eighth of the 4 suspension structure considered.
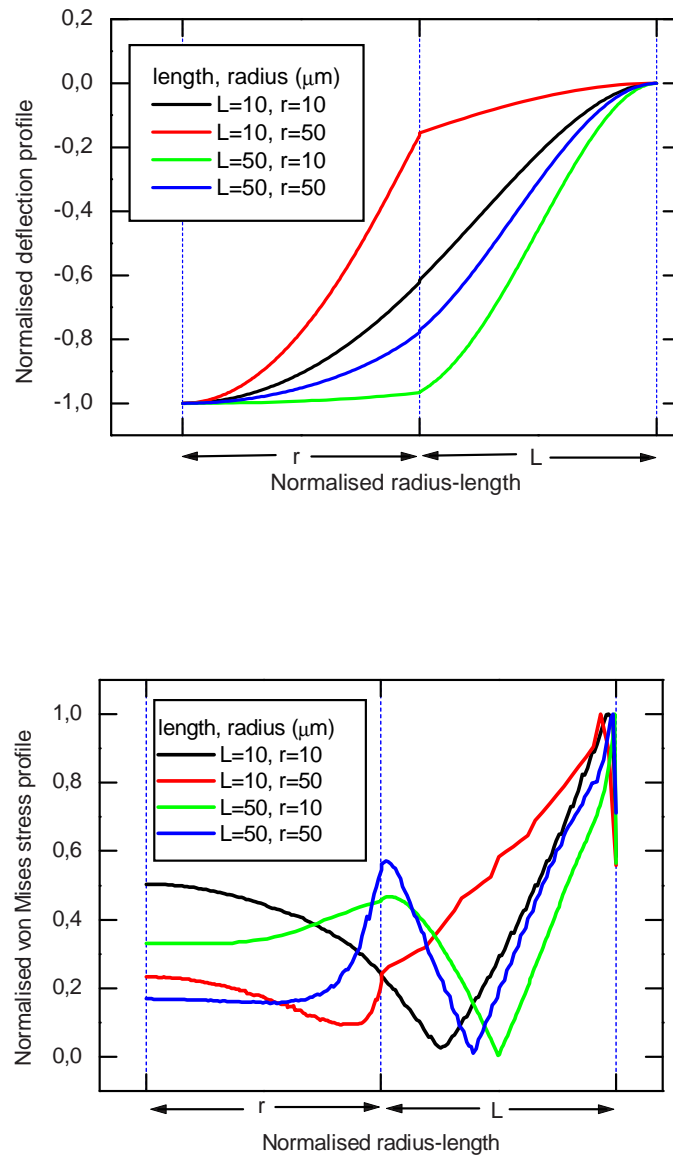
Fig. 3.23: Comparison of normalised deflection versus normalised suspension length and radius (top) and normalised von Mises stress profile versus normalised suspension length and radius (bottom), for various structures. Results extracted from 3D FEM calculations.

Chapter 4

Model calculations including residual stress

4.1 Introduction

In the preceding chapter the results of the electromechanical tuning behaviour of different configurations of the InP/air DBR FP filter were presented. A handy analytical model was derived in addition to the 2D and 3D electromechanical FEM models. All the calculations were carried out with the assumption of negligible residual stress in the structures. This assumption is however often not valid as observed in the structure that were fabricated. The SEM and WLI images of the devices often showed marked out-of-plane deformations as a result of stress in the devices. Figure 4.1 portrays WLI images of such a device.

This chapter presents a modified analytical model that includes the effect of residual stress and non-linear stiffening. The 3D FEM model used in chapter 3 is also modified to include the effect of axial residual stress. These are then used to investigate the effect on the out-of-plane deformation and device tuning. Finally comparison with measurements are made. But first, following immediately is an exploration of the nature of residual stress, the sources as well as an analytical model for the distribution in a membrane.
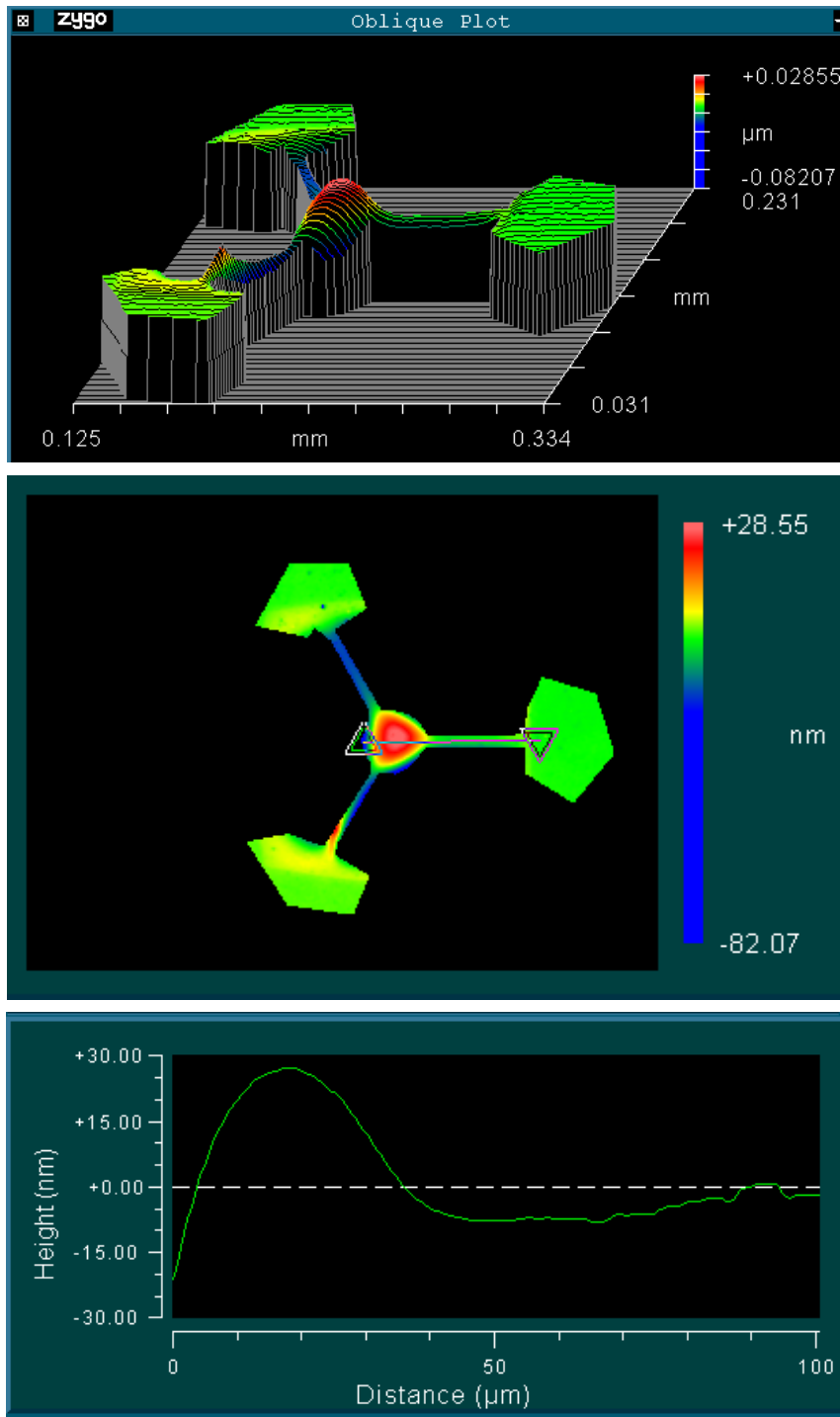
Fig. 4.1: WLI images showing out-of-plane deformation due to residual stress of a 3-suspension filter membrane. At the bottom is the measured profile of the bending.

4.2 Residual stress

4.2.1 Nature of residual stress

Residual stress can be defined as the stress that remains in a body after the technological realisation, or after processing, that occurs in the absence of external forces or thermal influence. Residual stress can be classified into two groups [103]; Macro and micro residual stress. Macro stress within a structure varies within a range that is much larger than the crystal grain size of the material forming the structure. Micro residual stress result from the differences within the microstructure of the material and can further be divided into two types. One type that operates at the grain size level and the other that is generated at the atomic level. Micro residual stress often results from presence of different phases or constituents in a material. It can change sign and/or magnitude over distances comparable to the crystal grain size of the material under consideration [104, 105, 106, 107].

Residual stress is also sometimes classified in terms of the distribution in the material. Thus we have uniform residual stress which can also be referred to as uniform axial stress when the uniformity is along an axial plane, whereas gradient residual stress describes the stress that varies along a given axis with a certain defined gradient. This stress gradient through the thickness of the material produces internal moments which can cause the structure to deform out of plane when a certain critical value is attained, especially for thin-walled structures. This often causes device failure or malfunction due to curling, warping, buckling, or fracture. In micro-mirrors, for instance, residual stress gradients can distort the flatness of the mirror surfaces rendering them unusable or reducing reflective efficiency. But the distortions can also sometimes result in desirable characteristics, for example where concave or convex, instead of flat, mirrors are needed, or in using the curvature of a structure to characterise the stress. However of utmost importance is the predictability and control of this stress.

4.2.2 Sources of residual stress

Residual stresses develop during most manufacturing processes involving material deformation, heat treatment, machining or processing operations that transform the shape or change the properties of a material. They arise from a number of sources and can be present in the unprocessed raw material, introduced during the manufacture or can arise from in-service loading [104]. The residual stresses may be sufficiently large to cause local yielding and plastic deformation, both on a microscopic and macroscopic level, and

can severely affect component performance. For this reason it is vital that some knowledge of the internal stress state can be deduced either from measurements or modelling predictions. Both the magnitude and distribution of the residual stress can be critical to performance and should be considered in the design of a component or device.

In any free standing body stress equilibrium must be maintained, which means that the presence of a tensile residual stress in the component will be balanced by a compressive stress elsewhere in the body. Tensile residual stresses in the surface of a component are generally undesirable since they can contribute to, and are often the major cause of, fatigue failure, quench cracking and stress-corrosion cracking. Compressive residual stresses in the surface layers are usually beneficial since they increase both fatigue strength and resistance to stress-corrosion cracking, and increase the bending strength of some brittle materials.

The origins of residual stresses in a component may be classified as: mechanical, thermal and chemical.

Mechanically generated residual stresses are often a result of manufacturing processes that produce non-uniform plastic deformation. They may develop naturally during processing or treatment, or may be introduced deliberately to develop a particular stress profile in a component [105].

On a macroscopic level, thermally generated residual stresses are often the consequence of non-uniform heating or cooling operations. Coupled with the material constraints in the bulk of a large component this can lead to severe thermal gradients and the development of large internal stresses. Microscopic thermally generated residual stresses can also develop in a material during manufacture and processing as a consequence of the coefficient of thermal expansion mismatch between different phases or constituents.

The chemically generated stresses can develop due to volume changes associated with chemical reactions, precipitation, or phase transformation.

4.2.3 Sources of residual stress in micromachined structures

Two main sources of residual stress in micromachined thin film structures are thermal stress resulting from mismatch in thermal expansion and intrinsic stress resulting from the microstructural set-up of the film. At substrate temperatures less than a quarter of the melting point, intrinsic stress due to incomplete structural ordering dominates [108]. Thermal stress occurs because film depositions are usually made above room temperature. Upon cooling from the deposition temperature to room temperature, the difference in the

thermal expansion coefficients of the substrate and the film cause thermal stress. Intrinsic stress results from the microstructure created in the film as atoms are deposited on the substrate.

Tensile stress results from micro-voids in the thin film, because of the attractive interaction of atoms across the voids. Compressive stress results when heavy ions or energetic particles strike the film during deposition. The impacts are like striking the film with a hammer, packing the atoms more tightly. This mechanism is often referred to as "atomic peening" (atomares Sandstahlen) [108]. Mismatch in the lattice constants where a crystalline material with a slightly different lattice constant is deposited on a substrate is also a major cause of stress.

Both tensile stress and compressive stress can exhibit a stress gradient that results from localised effects such as diffusion of atoms through the thickness of the film, interstitial or substitutional defects (e.g. from doping) and atomic peening [109, 110].
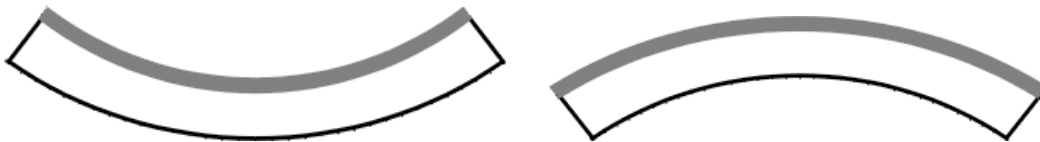
Fig. 4.2: Tensile(left)/compresive(right) stress, conceptual diagram. The top layer wants to be "smaller/larger" than the substrate because it was "stretched/compressed" to fit.

4.2.4 Control of residual stress in micromachining

Stress control in thin films is a very complex and challenging task. Recently, success has been reported in the control of residual stress [111, 112]. Stress control is achieved by varying the degree of energetic particle bombardment during deposition. Compressive stress is usually attributed to atomic peening at low pressures [108, 110]. An increase in pressure increases the frequency of gas phase collisions, reducing the kinetic energy of neutral atoms impinging on the growing film. This reduction in atomic peening reduces compressive stress. The deposition pressure at which a stress reversal from compressive to tensile occurs increases with the atomic mass of the element being deposited [108, 110].

4.2.5 Model for residual stress

In practice, it is difficult to accurately characterise the state of stress in a thin structure as it is known to depend on the fabrication process and often varies through the layer thickness

and span [106, 113, 114, 115, 109].

A general uniaxial residual stress model has been proposed in [109] as follows;

$$\sigma_{total} = \sum_{i=1}^{\infty} \sigma_i \left(\frac{z}{h/2} \right)^i \tag{4.1}$$

where $z \in (-h/2, h/2)$ is the coordinate across the thickness, h with an origin at midplane of layer.

For simplicity the first two parts of Eqn. (4.1) are retained viz.,

$$\sigma_{total} \approx \sigma_0 + \sigma_1 \left(\frac{z}{h/2} \right) \tag{4.2}$$

σ_0 represents the cumulative effect of all symmetrical polynomial terms in Eqn. (4.1), σ_1 represents the influence of gradient stress anti-symmetrical terms.

4.3 Coupling residual stress into the 3D FEM model

In the model considered above, the effect of residual stress is now introduced. The strain can be decomposed into two parts; the elastic strains, ε_e and the strains due to residual stress, ε_r. The total strain is therefore given by;

$$\varepsilon_i = \varepsilon_e + \varepsilon_{ri} \tag{4.3}$$

The residual strain, ε_r results from change from equilibrium in axial stress $\Delta\sigma_{ri}$. Hence, $\varepsilon_r = \Delta\sigma_{ri}/E$, where E, the modulus of elasticity, is assumed constant.

The stress-strain relationships, assuming no shear strains due to residual stress, change to

$$
\begin{aligned}
\varepsilon_x &= \frac{1}{E}[\sigma_x - \nu(\sigma_y + \sigma_z)] + \frac{1}{E}\Delta\sigma_{rx} \\
\varepsilon_y &= \frac{1}{E}[\sigma_y - \nu(\sigma_x + \sigma_z)] + \frac{1}{E}\Delta\sigma_{ry} \\
\varepsilon_z &= \frac{1}{E}[\sigma_z - \nu(\sigma_x + \sigma_y)] + \frac{1}{E}\Delta\sigma_{rz} \\
\varepsilon_{xy} &= \frac{1}{2G}\sigma_{xy} \\
\varepsilon_{yz} &= \frac{1}{2G}\sigma_{yz} \\
\varepsilon_{zx} &= \frac{1}{2G}\sigma_{zx}
\end{aligned}
\tag{4.4}
$$

alternatively,

$$
\begin{aligned}
\sigma_x &= \frac{E}{1+\nu}\left(\varepsilon_x + \frac{\nu}{1-2\nu}\left(\varepsilon_x + \varepsilon_y + \varepsilon_z\right) - \frac{1}{E}\Delta\sigma_{rx} - \frac{1}{E}\frac{\nu}{1-2\nu}(\Delta\sigma_{rx} + \Delta\sigma_{ry} + \Delta\sigma_{rz})\right) \\
\sigma_y &= \frac{E}{1+\nu}\left(\varepsilon_y + \frac{\nu}{1-2\nu}\left(\varepsilon_x + \varepsilon_y + \varepsilon_z\right) - \frac{1}{E}\Delta\sigma_{ry} - \frac{1}{E}\frac{\nu}{1-2\nu}(\Delta\sigma_{rx} + \Delta\sigma_{ry} + \Delta\sigma_{rz})\right) \\
\sigma_z &= \frac{E}{1+\nu}\left(\varepsilon_z + \frac{\nu}{1-2\nu}\left(\varepsilon_x + \varepsilon_y + \varepsilon_z\right) - \frac{1}{E}\Delta\sigma_{rz} - \frac{1}{E}\frac{\nu}{1-2\nu}(\Delta\sigma_{rx} + \Delta\sigma_{ry} + \Delta\sigma_{rz})\right) \\
\tau_{xy} &= G\gamma_{xy} \\
\tau_{yz} &= G\gamma_{yz} \\
\tau_{zx} &= G\gamma_{zx}
\end{aligned} \tag{4.5}
$$

In matrix form

$$
\begin{bmatrix} \sigma_x \\ \sigma_y \\ \sigma_z \\ \tau_{xy} \\ \tau_{yz} \\ \tau_{zx} \end{bmatrix} = \hat{D}\left(\begin{bmatrix} \varepsilon_x \\ \varepsilon_y \\ \varepsilon_z \\ \gamma_{xy} \\ \gamma_{yz} \\ \gamma_{zx} \end{bmatrix} - \frac{1}{E}\begin{bmatrix} \Delta\sigma_{rx} \\ \Delta\sigma_{ry} \\ \Delta\sigma_{rz} \\ 0 \\ 0 \\ 0 \end{bmatrix}\right)
$$

As before, for small deformations and time dependency, the equilibrium conditions are;

$$
\begin{aligned}
\rho\frac{\partial^2 u}{\partial t^2} - \frac{\partial \sigma_x}{\partial x} - \frac{\partial \tau_{xy}}{\partial y} - \frac{\partial \tau_{zx}}{\partial z} &= K_x \\
\rho\frac{\partial^2 v}{\partial t^2} - \frac{\partial \tau_{xy}}{\partial x} - \frac{\partial \sigma_y}{\partial y} - \frac{\partial \tau_{yz}}{\partial z} &= K_y \\
\rho\frac{\partial^2 w}{\partial t^2} - \frac{\partial \tau_{zx}}{\partial x} - \frac{\partial \tau_{yz}}{\partial y} - \frac{\partial \sigma_z}{\partial z} &= K_z
\end{aligned} \tag{4.6}
$$

the corresponding formulation of Navier's equations in this case are;

$$
\rho\frac{\partial^2 u_i}{\partial t^2} - \sum_j\left[\frac{\partial}{\partial x_j}G\left(\frac{\partial u_i}{\partial x_j} + \frac{\partial u_j}{\partial x_i}\right) + \frac{\partial}{\partial x_i}\left(\mu_L\frac{\partial u_j}{\partial x_j} - \frac{2G}{3E}\Delta\sigma_{ri} - \frac{1}{E}\mu_L\Delta\sigma_{rj}\right)\right] = K_i \tag{4.7}
$$

In compact notation

$$
\rho\frac{\partial^2 \mathbf{u}}{\partial t^2} - \nabla\cdot\hat{c}(\nabla\mathbf{u} - \frac{1}{E}\nabla(\Delta\sigma_r)) = \mathbf{K} \tag{4.8}
$$

To solve this PDE using FEM with FEMLAB, it is considered as two coupled PDEs. The first one is the standard 3D structural mechanics formulation

$$\rho \frac{\partial^2 \mathbf{u}}{\partial t^2} - \nabla \cdot \hat{c} \nabla \mathbf{u} = \mathbf{K} \tag{4.9}$$

and the second is the PDE

$$\nabla \cdot \frac{1}{E} \nabla (\Delta \sigma_r) = \mathbf{S} \tag{4.10}$$

With the source term $\mathbf{S}$ set zero, the boundary and the initial conditions can be set to appropriately describe the residual stress profile in the considered material. Solving the coupled system results in 3D elastic deformation calculations that include the effect of residual stress in the structure.

However, residual stress can cause large deformations. Large deformations are said to occur when large strains (more than 1%) exist or when the strains are small but large rotations exist. In such cases, the relation between the strain and displacement requires a different definition other than the engineering strain definition used above. The logarithmic or the Green-Lagrange definition should be used. The Green-Lagrange strain tensor is defined as [116];

$$\varepsilon_{ij} = \frac{1}{2} \left(\frac{\partial u_i}{\partial x_j} + \frac{\partial u_j}{\partial x_i} + \frac{\partial u_k}{\partial x_i} \frac{\partial u_k}{\partial x_j} \right) \tag{4.11}$$

The solution of such a nonlinear problem is more involving. Fortunately some of the available FEM software have in-built algorithms for such purposes.

To verify the accuracy of the method, various beam models duplicating those found in the literature [88, 89] were set up and the performance compared with the published results. They were found to agree very closely.

4.4 Analytical model with residual stress and stress stiffening effects

It was observed in the last chapter from the FEM calculations that the stiffness of the structures in deed varies not just with the structural configuration, but also with the biaxial "membrane stretching". This stretching is a non-linear effect referred to as the non-linear stress stiffening. The third factor that influences the effective stiffness is the residual stress. In order to obtain a more accurate analytical model for the devices, all these effects have

to be accounted for.

The effective stiffness of a fixed-fixed beam, k_{eff} (Nm^{-1}) can be defined as

$$k_{eff} = \frac{pl}{\delta_{max}} \tag{4.12}$$

where p (Nm^{-1}) is a uniformly distributed force over the length l of the beam, and δ_{max} is the maximum deflection at the centre of the beam. This has been shown to have the following form that includes the influence of the material parameters, the dimensions, the residual stress and the stress stiffening effect [89, 117].

$$
\begin{aligned}
k_{eff} &= \frac{pl}{\delta_{max}} \\
&= \frac{2kN}{\frac{kl}{4} - tanh(\frac{kl}{4})}
\end{aligned}
\tag{4.13}
$$

and

$$
\begin{aligned}
N &= (\hat{\sigma}_0 + \sigma_{NL})\text{w}h \\
k &= \sqrt{\frac{12N}{E\text{w}h^3}} \\
\hat{\sigma}_0 &= \sigma_0(1 - \nu) \\
\sigma_{NL} &= \hat{E}\left(\frac{\pi\delta_{max}}{2l}\right)^2
\end{aligned}
$$

where $\hat{\sigma}_0$ is the residual stress contribution, σ_{NL} the estimate of the stress due to non-linear stretching and $\hat{E}$ the effective modulus of elasticity.

For $kl < 1$, the *tanh* in the expression can be expanded in power series and truncated at the second term giving

$$k_{eff} \approx \frac{32E\text{w}h^3}{l^3} + \frac{48N}{5l} \tag{4.14}$$

A more general expression covering a wider range for kl is proposed in [89] as

$$k_{eff} \approx \frac{32E\text{w}h^3}{l^3} + \frac{C3N}{l} \tag{4.15}$$

C3 being a fitting coefficient.

By applying a similar analogy used to determine the stiffness values given in Table 3.1, the effective stiffness for the filter structure that includes the additional effects of

non-linear stress and residual stress is given as

$$k_{eff} \approx C_1 \frac{D\mathrm{w}}{(2l + \mathrm{w}(1 + C_2\xi))^3} + C_3 \frac{N}{(2l + \mathrm{w}(1 + C_2\xi))} \tag{4.16}$$

Again, in a similar way to Table 3.1, the values of C_3 are obtained by fitting values generated from FEM calculations. Similar derivations were carried out for 3- and 4- suspension structures. The results are summarised in Table 4.1

4.5   Influence of stress stiffening on stable range of operation

Now that the new effective spring constants that include the effects of stress stiffening and residual stress have been derived, once more consider the coupled electro-mechanical system in quasi-static equilibrium ($\dot{u} = \ddot{u} = 0$) with a deflection $u = \delta$ and let $k_{eff} = k_1 + k_2\delta^2$.

$$\begin{aligned} f_{mechanical} &= f_{electrostatic} \\ k_{eff}\delta &= \frac{\varepsilon_0 V^2 A}{8(\frac{g_0}{2} - \delta)^2} \end{aligned} \tag{4.17}$$

Substituting for k_{eff} and rearranging this equation results in

$$8(k_1 + k_2\delta^2)\delta(\frac{g_0}{2} - \delta)^2 - \varepsilon_0 V^2 A = 0 \tag{4.18}$$

This is a fifth order polynomial in δ. Using a Matlab program to solve for the only stable value of δ, the plot of Fig. 4.3 is obtained. This is plotted alongside the 3D FEM result in Fig. 3.6 in the previous chapter. It is observed in this plot that the new pull-in point predicted by Eqn. (4.18) agrees almost perfectly with the value obtained from the 3D

No. of Suspensions	k_{eff}
2	$47\frac{D\mathrm{w}}{(2l+\mathrm{w}(1+0.87\xi))^3} + 13\frac{N}{(2l+\mathrm{w}(1+0.87\xi))}$
3	$72\frac{D\mathrm{w}}{(2l+\mathrm{w}(1+0.26\xi))^3} + 13\frac{N}{(2l+\mathrm{w}(1+0.26\xi))}$
4	$108\frac{D\mathrm{w}}{(2l+\mathrm{w}(1+0.67\xi))^3} + 13\frac{N}{(2l+\mathrm{w}(1+0.67\xi))}$

Table 4.1: Effective spring constants for 2- 3- and 4- suspension filter configurations including stress effects.
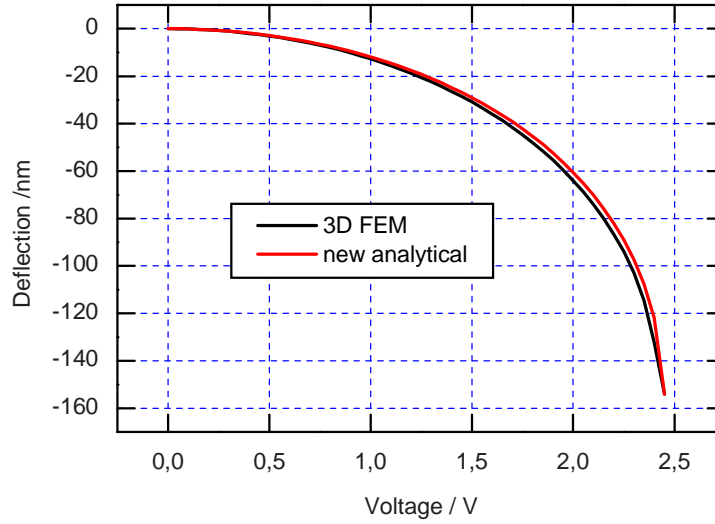
Fig. 4.3: Improved analytical calculation of voltage vs deflection characteristic for a $3\lambda/4$ InP filter membrane with four $40\mu m$ long, $10\mu m$ wide suspensions and a $40\mu m$ diameter membrane. The result is plotted alongside the 3D FEM calculation.

FEM model.

As before electrostatic force increases non-linearly with decreasing gap, but the spring constant force is now a non-linear function of change in gap spacing. The voltage at which the restoring spring force no longer balances the attractive electrostatic force now shifts to a new (pull-in) point. The new plot of the forces versus deflection is given in Fig. 4.4.

In order to determine the new limit of the stable range of operation, i.e. the new pull-in point, the net force is analysed in a similar way to that in chapter 3. The net force is given by

$$f_{net} = k_{eff}\delta - \frac{\varepsilon_0 V^2 A}{8(\frac{g_0}{2} - \delta)^2} \tag{4.19}$$

Again stability requires that $\partial f_{net} < 0$. The edge of the stable region is defined by $f_{net} = 0$ and $\frac{\partial f_{net}}{\partial \delta} = 0$

$$
\begin{aligned}
\partial f_{net} &= \left. \frac{\partial f_{net}}{\partial \delta} \right|_V \partial \delta \\
&= \left(k_{eff} - \frac{\varepsilon_0 V^2 A}{4(\frac{g_0}{2} - \delta)^3} \right) \partial \delta
\end{aligned} \tag{4.20}
$$
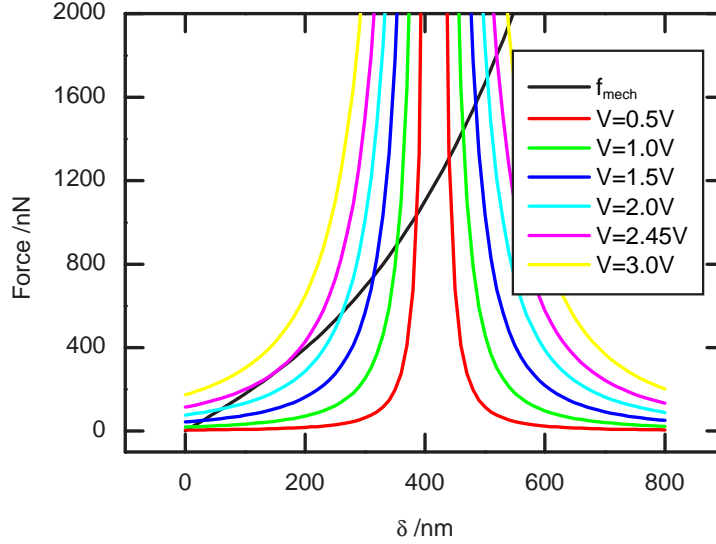
Fig. 4.4: Calculated mechanical and electrostatic forces vs deflection for a $3\lambda/4$ InP filter membrane with four $40\mu m$ long, $10\ \mu m$ wide suspensions and a $40\mu m$ diameter membrane using improved model. Note that the new $V_{PI} = 2.45V$, and that the mechanical force is no longer a linear function of the deflection.

These yield

$$2(k_1 + k_2\delta^2)\delta - (k_1 + 3k_2\delta^2)(\frac{g_0}{2} - \delta) = 0 \qquad (4.21)$$

This is a third order polynomial in δ which implies that the value for the pull in, δ_{PI} is no longer a constant, but a variable determined by the changing spring constant which is in turn a function of the geometry, in-built stress and stress stiffening.

Figures 4.5, 4.6 and 4.7 illustrate the variation of pull-in voltage with suspension length, central membrane radius and suspension width, respectively. These results are plotted alongside those obtained from FEM simulations in the last chapter. The analytical and FEM results agree remarkably well for a large range of structural variations. The pull-in point for all the 4 suspension structures investigated was found to have increased by almost 12 % from that predicted by Eqn. (3.37). The new pull-in voltage is therefore given by;
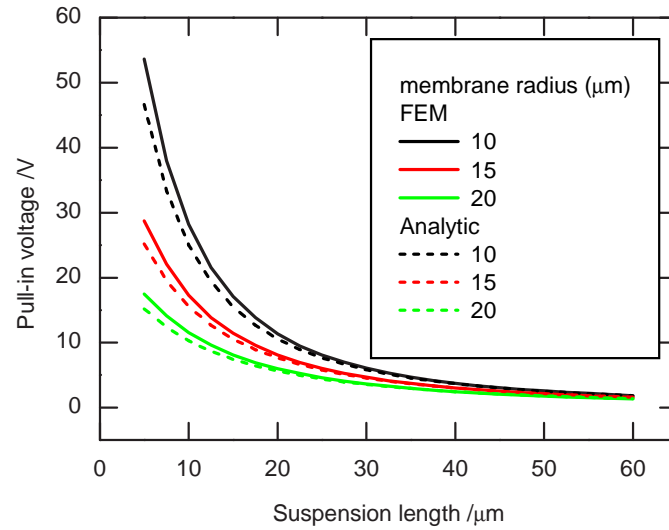
Fig. 4.5: Comparison of analytical prediction with FEM results of the change in the pull-in voltage with suspension length, suspension width=10μm.
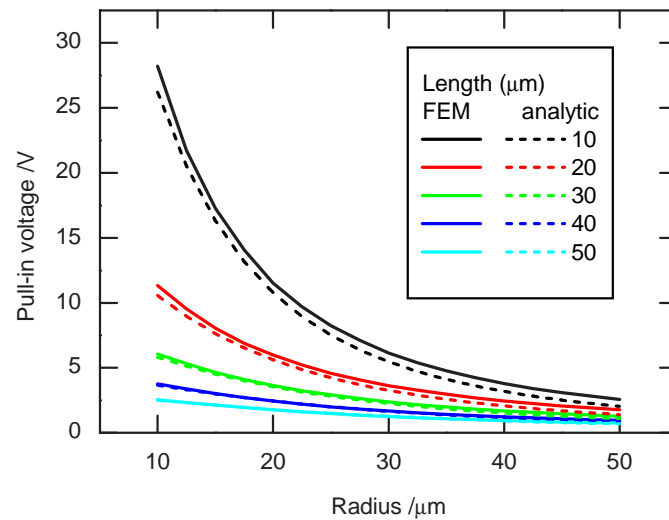
Fig. 4.6: Comparison of analytical prediction with FEM results of the change in the pull-in voltage with membrane radius, suspension width=10μm.
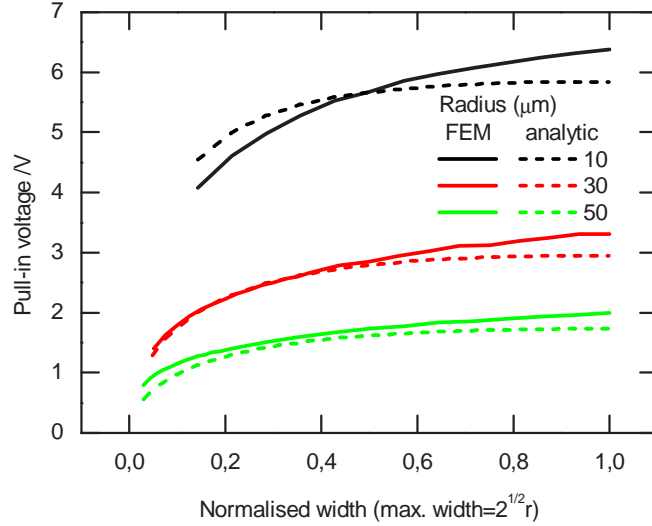
Fig. 4.7: Comparison of analytical prediction with FEM results of the change in the pull-in voltage with suspension width, suspension length=30μm.

$$
\begin{aligned}
V_{PI} &= \left.\sqrt{\frac{8\delta k_{eff}}{A\varepsilon}\left(\frac{g_0}{2} - \delta\right)}\right|_{\delta=g_0/5} \\
&= \frac{3}{25}\sqrt{\frac{2g_0^3(5k_1 + k_2 g_0^2)}{A\varepsilon}}
\end{aligned}
\tag{4.22}
$$

4.6 Influence of residual stress on out-of-plane deformation and tuning

It was stated in the introductory part of this chapter that residual stress has a major influence on the out-of-plane deformation of thin-walled structures, even in the absence of an external force. It was also proposed that residual stress can be considered to compose of mainly the axial stress and gradient stress. In this section, results of the 3D FEM analysis of the effect of stress on a chosen structure with and without the influence of an external (in this case electrostatic) force are presented. A stress profile deduced from the deformation of a filter is extracted and used in the FEM model to calculate the tuning characteristic. This is then compared with the experimentally measured curve.

4.6.1 Effect of gradient stress

Figure 4.8 portrays the membrane deformation caused by gradient residual stress. The bending direction depends on the profile of the stress gradient. If it is such that compressive stress exists on the upper part and tensile stress at the bottom of the membrane, then the bending is towards the upper direction, and conversely for a reversed gradient. This effect is summarised in the plot of Fig. 4.9. The figure shows the amount of out-of-plane deflection produced by various amounts of stress without an external force, as well as the deflection when in addition an external electrostatic force is applied. The fact that the characteristics are not parallel shows that the effective stiffness of the structure is modified by the residual stress gradient.

4.6.2 Effect of biaxial stress

The axial stresses existing in the structures considered were assumed to act uniformly in the planes perpendicular to the plane of the plate, and that the axial stress along the thickness of the plate was negligible. Hence the uniform stress existing in the structures is referred to as biaxial stress. In terms of cartesian coordinates, the uniform stress in the x- and y-directions are equal, and negligible in the z-direction, where the membrane thickness is in the z-direction. The diagram of Fig. 4.10 shows the effect on the membrane deflection of the biaxial stress in the structure. With no external force applied, the membrane tends to show only either expansion (compressive stress) or shrinkage (tensile stress). With an applied force, it is clear from the diagram that compressive stress tends to reduce the effective stiffness and tensile stress increases it. In the diagram, at zero voltage, it appears as if the applied force causes a deflection of the membrane. In reality, this deflection is a movement of the reference point (bottom of centre of membrane) due to expansion from compressive stress (left) or shrinkage from tensile stress (right).

4.6.3 Combined effect of biaxial and gradient stress

The combined effect of biaxial and gradient stress can be approximated as a superposition of the two according to Eqn. (4.2). This implies that by considering the results shown in Fig. 4.9 and Fig. 4.10 together, the combined effect of the biaxial and gradient stress can be deduced. Such an approximation will suffice in most cases where the deformations caused by the stress are not too large. Otherwise it has to be considered that stresses are non-linear effects, in which case superposition does not always apply.
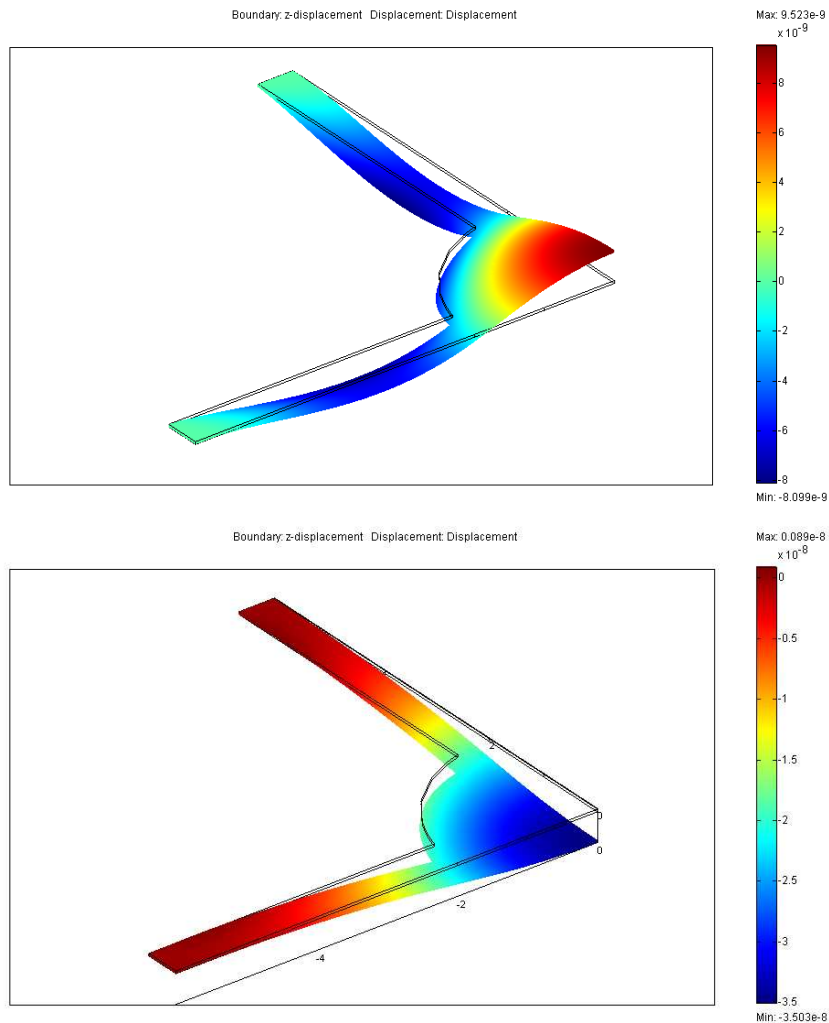
Fig. 4.8: Out-of-plane deformation resulting from gradient stress for a four suspension structure, one quarter of which is shown. The top structure has compressive stress in the top half of the width and tensile stress in the lower half. This is vice versa for bottom structure.

4.6.4   Comparison with measurement

Both biaxial and gradient stress can be extracted from experiment by use of simple cantilever structures. Biaxial stress causes expansion or shrinkage of structures, whereas gradient stress would manifest itself as a curling of the cantilever. By fitting the measured profile to FEM simulations, the values of both stresses in the material can be deduced. If the cantilevers are produced on the same batch as the fabricated devices, the values deduced can be further used to determine the influence of these stresses on the other devices.

In the case of this work, such an extraction was not done. However, it is seen in the preceding sections that the FEM calculations can be used to determine the amount of out-
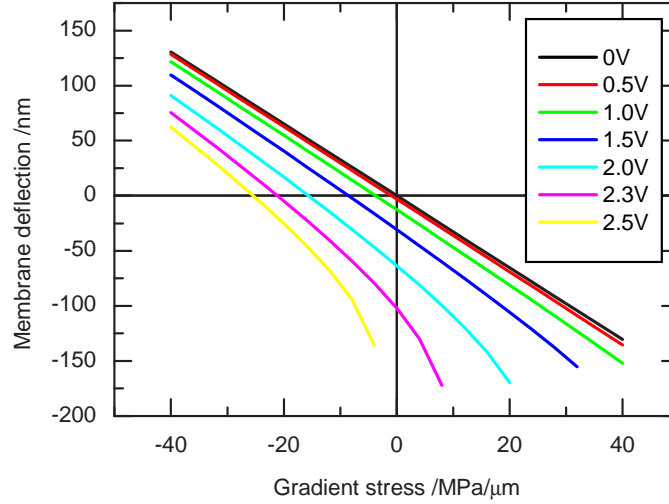
Fig. 4.9: Deflection vs gradient stress characteristics for various values of applied voltage. Negative stress gradient imply compressive stress in the top half of the membrane, tensile stress in the bottom half. The structure with four suspensions of 40μm length and 10μm width with membrane diameter of 40μm is considered.

of-plane deformations for various amounts of stress. It was also seen that the deformation results mostly from the gradient stress.

In the following, one measurement [22] example is analysed. This was for an all air-gap InP filter with four suspensions of 40μm length and 10μm width. The central membrane had a diameter of 40μm. The membranes had a thickness of $\frac{3}{4}$ of the reference wavelength in the material. The filter was characterised by measuring the resonant wavelength for various cavity lengths. The cavity length was changed (reduced) by varying the voltage, starting from zero volts.

The design cavity was 830nm long, but with no actuation voltage applied, the measured wavelength was 1599nm. Using SPECTRAFIT [75], a very sophisticated program for performing one dimensional optical calculations, the tuning efficiency of the filter was calculated to be 0.71. The concept of tuning efficiency was introduced in chapter 2 section 2.4.5. With this value, it is deduced that the actual cavity length at 0V is 830+(1599-1550)/0.71 nm. This gives about 899nm. This increment in cavity length is caused by the residual stress. Assuming the lower and upper membranes are equally deformed in opposite direction creating a concave cavity, the amount of deflection at the centre of each
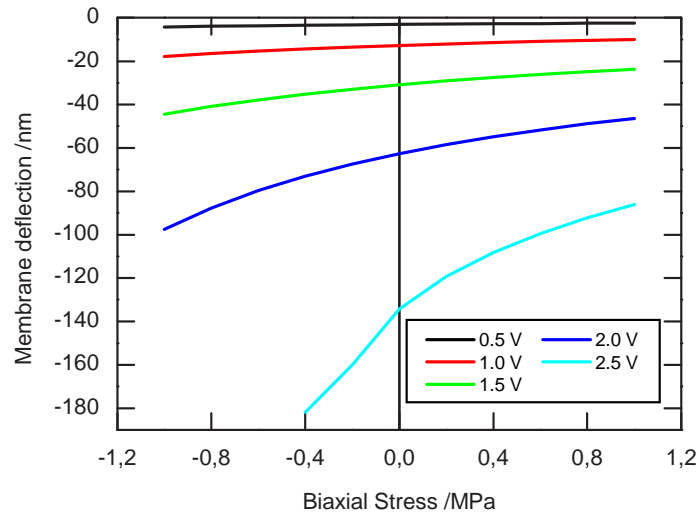
Fig. 4.10: Deflection vs biaxial stress characteristics for various values of applied voltages. Negative stress values imply compressive stress, positive values are tensile. The structure with four suspensions of 40μm length and 10μm width with membrane diameter of 40μm is considered.

membrane is about 34.5nm. The results of Fig. 4.9 are used to extract the value of the gradient stress causing such a deformation. This value is then inserted in the FEM calculations to determine the tuning characteristic that takes gradient stress into account. In this work, no mechanism was in place to estimate the biaxial stress. The results therefore excluded this effect. Two characteristics were determined. The first marked "double" assumed a symmetrical actuation of the membranes. The second one marked "single" assumed that only the one membrane moves in the actuation, the other being hindered somehow. These of course are extreme cases. The results are plotted alongside the measured values in Fig. 4.11. It is interesting to note that although the characteristic with symmetrical actuation shows a divergence from the measured value for large values, the experimentally measured pull-in voltage agrees almost perfectly with the calculated one. It can also be observed that the measured values lie in between the two calculated extremes. The justification of considering these extremes is that so far, no working method has been devised for determining the deformation profiles of the inner membranes in the filter, or knowing exactly what the stress profiles are. It is therefore difficult to characterise the stress in these membranes, besides no estimate of the biaxial stress was used in the calculations. The results presented here demonstrate that the treatment given is to a
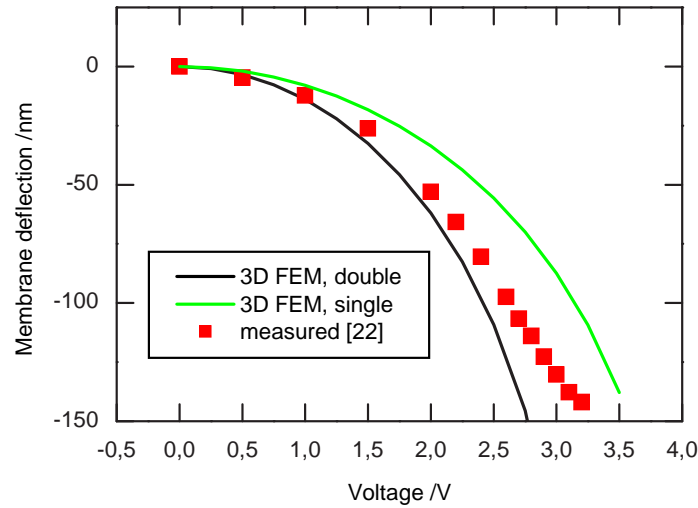
Fig. 4.11: Comparison of FEM simulated and experimentally measured characteristics for a four suspension all air-gap filter with 40μm and 10μm suspension length and width, respectively. The central membrane had a diameter of 40 μm.

large extend very satisfactory.

Another factor that might have affected the outcome of the calculations is the uncertainty in the value of the material parameters, in this case, the modulus of elasticity. In the literature, widely varying values for the modulus of elasticity of InP were encountered. This ranged from 61 GPa [102] to 82 GPa [118], 93GPa [119] and 93.41 GPa [120].

4.6.5 Summary

Residual stress is often an undesirable effect that cannot in many cases be ignored. In this chapter an explanation of the nature and sources of residual stress has been presented. Both the 3D and analytical models of chapter 3 are accordingly modified to include the effect of residual stress. These have been used to determine the influence of stress on the out-of-plane deformation of the unactuated structures as well as on the electromechanical tuning behaviour. Comparison of model output with experimental measurements are presented showing good agreement despite neglecting the effect of biaxial stress.

Chapter 5

Tailored scaling of a photonic device

5.1   Introduction

Some of the major goals in the successful manufacture of photonic devices such as those considered in this work are low cost, high production throughput, high yield, high reliability and high structural and performance stability [19].

Several arguments can be put forward for the physical down-scaling of devices as a means to realizing the above listed goals. First, a smaller device size in the surface micromachining production process results in a higher throughput as more devices are produced per wafer. This would in addition cut down the cost per device. Secondly, as structures are physically scaled down, the actions of physical effects such as gravity and inertia on them add up in such a way as to result in higher structural stability. The higher structural stability result in an improved yield, higher reliability and better performance stability such as in the transient response.

The use of less material per device could also open up room for the cost-effective exploitation of expensive exotic materials that would otherwise not be viable on the basis of high cost. The smaller size also contributes to reducing fatigue of the material, resulting in longer lifetimes [77][78] and makes it easier to integrate with other devices of the same order of magnitude in size and add functionality by incorporating other functions, e.g. logic circuits, in order to realize high performance MEMS [121].

This chapter focuses on the design considerations in the scaling down of a micro-machined DBR that is used in electrostatically tunable vertical cavity optical devices such as vertical cavity optical filters described in the preceding chapters and VCSELs. A device designed for DWDM applications must operate within a certain specified wave-

length bandwidth. In scaling such a device it is important that the resulting device maintains the same operational bandwidth. It might also be desirable to maintain the same cavity-length-change versus voltage characteristic so that the new device is seamlessly exchangeable with the original. The chapter aims to demonstrate that a kind of tailored scaling can be applied in such a way that exactly the same mechanical tuning characteristic is maintained on down- or up-scaling as desired. An even more promising aspect is the demonstration that such tailored down-scaling results in a device structure with a highly improved stability and speed of response.

5.2 Tailored miniaturization

It is indeed intriguing to consider the range of possible designs offered by miniaturization that would otherwise not be realisable in the macro-world. This follows from the way physical effects such as gravity, inertia and electrostatic forces depend on space coordinates. Earlier discussions on scaling [122][123][124] explored advantages, extend and applicability of microsystems in general. In [77][78] it is mentioned that potential exists to optimize mechanical and electronic components if characteristic structure sizes are designed and tailored according to key fundamental physical effects. Herein lies the basic motivation for the investigation presented in this chapter. As an illustration, consider a scaling factor, a_i. Each space dimension, $x_i (i = 1, 2, 3)$ of a three dimensional structure can be scaled by the transformation, $x_i \rightarrow x_i/a_i$. Figure 5.1 illustrates how these effects vary in relative significance from the cosmic scale down to the nano scale. It is observed that gravity and inertia have a much smaller influence, relative to electrostatic force, on miniaturized structures in the micro and nano range as compared to structures in the macro range. This can explain a number of design limitations and occurrences in nature. As an example consider a 3-D structure scaled by the transformation $x_i \rightarrow x_i/a$. The weight of such a structure would change by a factor a^{-3} and the mechanical strength by a^{-2} [124]. The ratio of strength to weight results in $a^{-2}/a^{-3} = a$. This indicates that when $a > 1$ (down-scaling) the influence of mechanical strength becomes dominant over that of weight. This explains the superiority of smaller structures in supporting their own weight in comparison to larger structures, or why some insects (e.g. ants) can easily carry many times their own weight on wiry legs, a feat simply not possible in the macro world. In MEMS and micro-opto-electromechanical systems (MOEMS) such phenomena are exploited to realize novel designs.
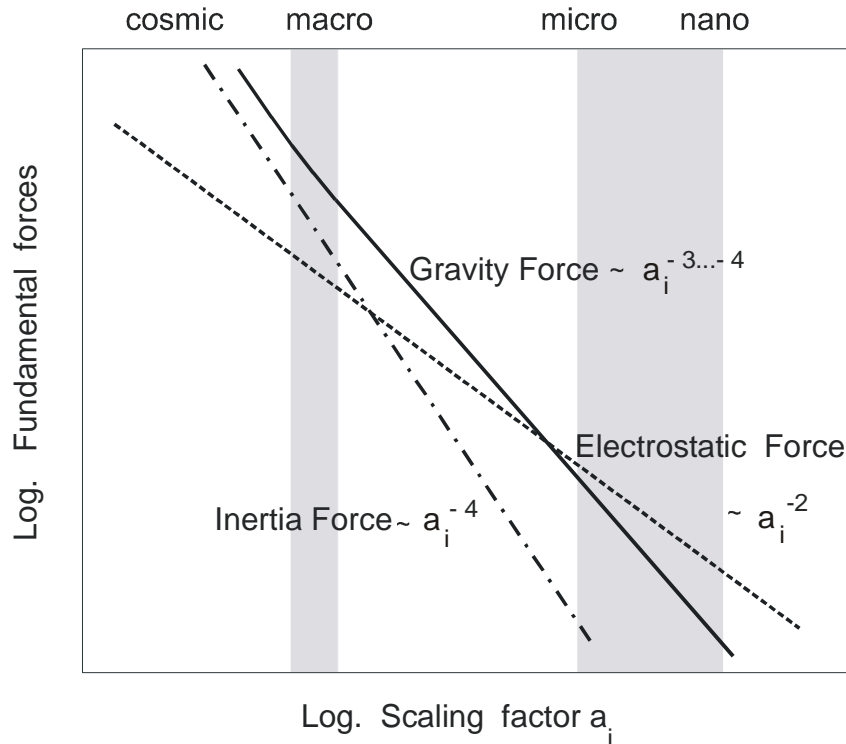
Fig. 5.1: Variation of the relative significance of individual fundamental forces with size in 3D space. [courtesy of Prof. Dr. H. Hillmer].

In the following, the effect of scaling down a Fabry-Perot filter structure with InP/air DBRs on the tuning performance is investigated. The work sets out with a desire to maintain the same optical cavity length as well as the same mechanical tuning characteristic as the original un-scaled structure. In this way, the new device would seamlessly substitute the original one with the added advantages of a scaled down structure. It is demonstrated that simply scaling down all the dimensions of the device by the same factor does not lead to the goal strived for and that a kind of tailored scaling must be applied to achieve this goal. Other analyses done show a structurally, and performance-wise, more stable scaled down structure as gauged in terms of resonant frequency, speed of response and response to a gravitational shock impulse.

5.3 Steps in scaling the filter membrane

The first step in down-scaling is in the reduction in membrane thickness taking into account that the possible optimum optical thickness values have already been set as $m_i \cdot \frac{1}{4}\lambda_{mat}$ ($m_i = 1, 3, \ldots$). The current state of surface micromachining technology ap-

plied in the production of these structures still presents difficulties in the realization of membranes with thickness values around 100nm and below. However, by innovatively combining layers of different thickness (different m_i's), a filter structure can be conceived that is mechanically stable. A DBR structure with three InP/air periods was considered in this investigation. Just one (the inner electrostatically actuated) of the three DBR membranes was scaled by a factor of 3 from $\frac{3}{4}\lambda_{mat}$ to $\frac{1}{4}\lambda_{mat}$. All the other membranes kept the mechanically stronger thickness of $\frac{3}{4}\lambda_{mat}$.

On decreasing the thickness of a membrane by a factor of 3, the bending (flexural) rigidity decreases almost thirty times. This implies that if the same pressure is applied on the scaled membrane as was applied on the original membrane the deflection produced would go up in the same proportion as the decrease in rigidity. The lateral dimensions (diameter of membrane, length and width of the suspensions) must therefore be scaled down appropriately to obtain the same deflection effect as prior to scaling. This is then the next step in scaling. The lateral scaling factor needed to satisfy this requirement is deduced below.

5.4 Results

5.4.1 Tailored lateral scaling factor

To determine the effect of scaling on the deflection produced by an electrostatic pressure, the pressure on the InP membrane was kept constant (by keeping the voltage and the cavity length fixed) as space dimensions were variously scaled by factors between 1 and 3, inclusive. In Fig. 5.2, the effects, depicted as normalized mechanical tuning, (i) of down-scaling the thickness as the lateral dimensions are kept constant (line with diamond symbols), (ii) down-scaling the lateral dimensions as the thickness is kept constant (squares) and (iii) simultaneously down-scaling all dimensions with the same factor (circles) are seen. The circles line reveals that simply simultaneously scaling down all the dimensions of the membrane by the same factor results in a filter structure with a lower tuning performance as gauged by the "mechanical tuning efficiency", $w/\triangle V$. To obtain an un-degraded (same) tuning performance, the thickness and the lateral dimensions must therefore be scaled differently. For the exact relationship an analytic solution for the deflection of the filter structure would be needed. This requires the solution of the classical biharmonic plate equation for the structure. The classical equation of transverse motion
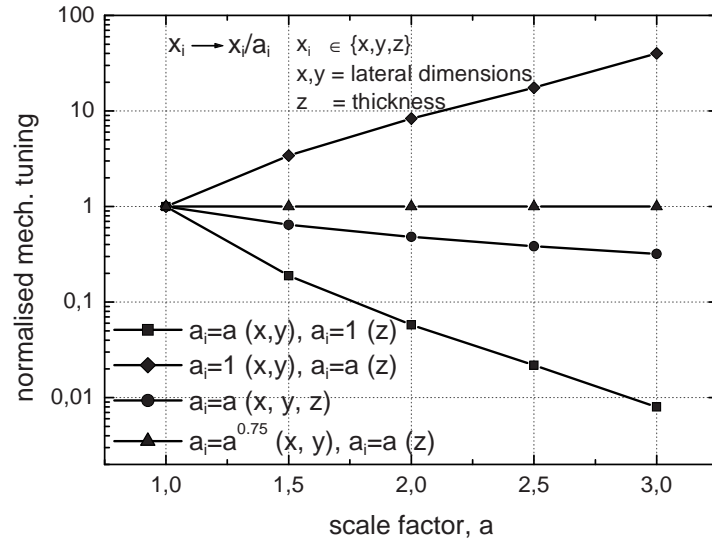
Fig. 5.2: Normalized mechanical tuning for various scaling configurations and factors.

of the homogenous, isotropic elastic plates is [125] [126] [127]

$$D\nabla^4 w + m\frac{\partial^2 w}{\partial t^2} = p(w) \tag{5.1}$$

where the biharmonic differential operator $\nabla^4 = \partial^4/\partial x^4 + \partial^4/\partial x^2\partial y^2 + \partial^4/\partial y^4$ in Cartesian coordinates.

The exact solution for this equation for unusual geometries like the ones considered here is a daunting task. However, solutions abound in literature [124] [126] [127] [128] for the deflection of plates of various shapes, and for various loading and boundary conditions. Based on this knowledge we empirically found for our structures that if their thickness is scaled by a factor k_t, the lateral dimensions would have to be scaled down by a certain factor k_l to maintain the same deflection for the same applied pressure, where

$$k_l^4 = k_t^3 \ or \ k_l = k_t^{\frac{3}{4}} \tag{5.2}$$

This result was put to test in scaling down the structure considered above using scale factors between 1 and 3 as before. The normalized membrane deflection (tuning) obtained is depicted in Fig. 5.2 as the line with the triangle symbols. It shows that the deflection produced by a given constant force per unit area remains practically unchanged on scaling

according to Eqn. (5.2).

Further, the mechanical tuning characteristic was determined before and after application of this "tailored scaling". The tuning characteristic referred to here is that of the membrane deflection versus the applied voltage. For the results presented here a scaling factor of 3 was used. That is to say that the membrane thickness was scaled down to one third and the lateral dimensions to $1/3^{\frac{3}{4}}$ of the original. This was done for the 4 suspension structure above and similarly repeated for 3 and 2 suspension structures, each with original thickness of $\frac{3}{4}\lambda_{mat} = 357$nm, membrane diameter of 35μm and suspension lengths of 35μm.

The comparison of the characteristics for each set of calculations showed an extremely good agreement. Fig. 5.3 summarizes the results of the mechanical tuning for the 2, 3 and 4 suspension structures normalized to the pull-in point. The solid symbols on the
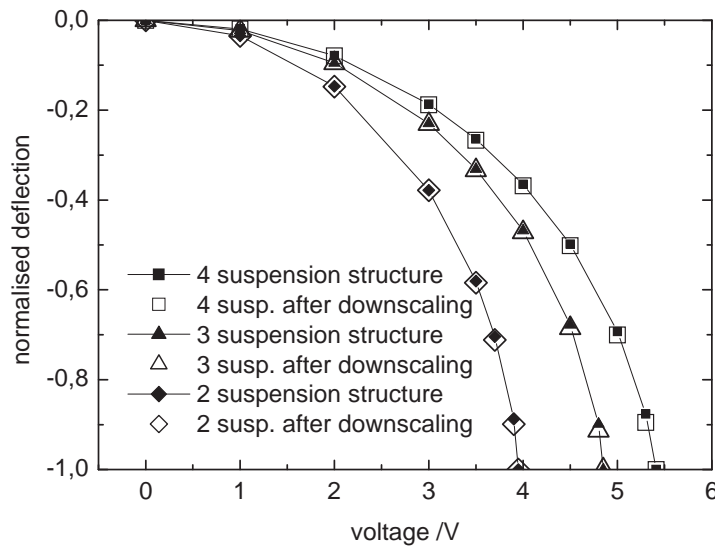
Fig. 5.3: Comparison of deflection characteristics before and after down-scaling of 2, 3 and 4 suspension structures.

continuous lines in the graph represent the tuning characteristic before scaling, whereas the hollow symbols are values calculated after scaling down. This agreement is a confirmation that with this kind of "tailored scaling", one ends up with variously scaled devices that replicate the mechanical tuning efficiency of the original almost exactly. But what does one gain from such tailored scaling? To answer this question, the eigen-frequencies,

suspensions	eigenfrequency(Hz)	freq. after scaling(Hz)
2	121227	210448
3	149128	259144
4	167061	290462

Table 5.1: First mode eigenfrequencies before and after down-scaling by a factor of 3.

the transient response and the response to a gravitational shock impulse were compared.

5.4.2   Comparison of temporal response

The 2D Mindlin plate theory method described in chapter 3 was used to perform modal analysis and to study the transient response of the structures. The results of the first mode eigen-frequencies for the structures before and after down scaling are listed in Table 5.1. The results show an average increase of 73.8 % on tailored down-scaling by a factor of 3. The second mode shape for one of the structures is depicted in the Fig. 5.4. Next were
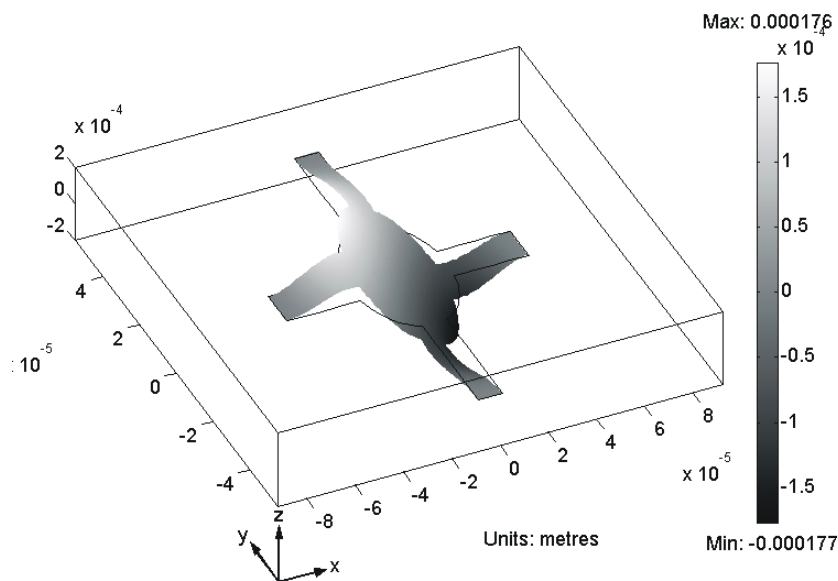
Fig. 5.4: Second order mode shape of a four suspension structure obtained from the quasi-3D FEM program.

the calculations of the transient response due to an applied electrostatic actuation. The diagram in Fig. 5.5 depicts the response to one of the structures and that of its scaled down counterpart in Fig. 5.6 to a 1V step voltage. Two important observations can be made
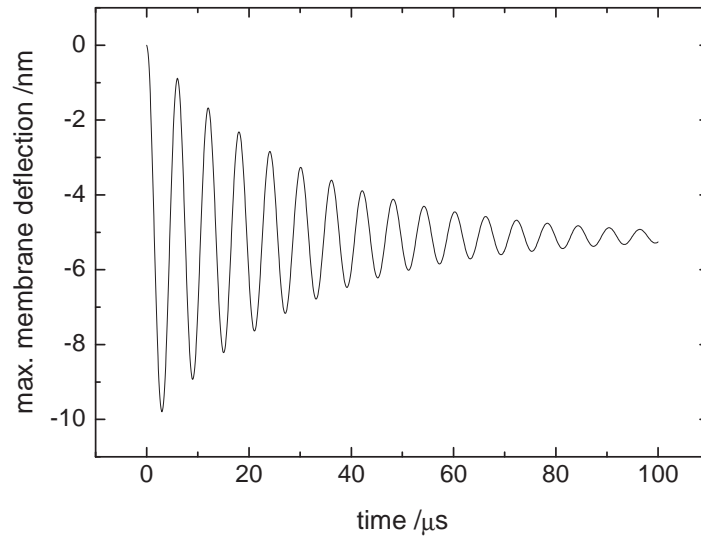
Fig. 5.5: Time response of a four suspension structure to a 1V step voltage before scaling down.
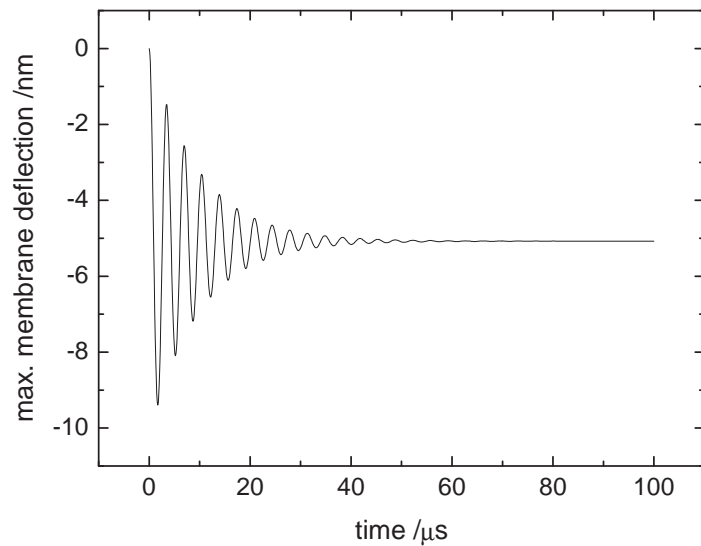
Fig. 5.6: Time response of the four suspension structure in Fig. 5.5 to a 1V step voltage after scaling down.
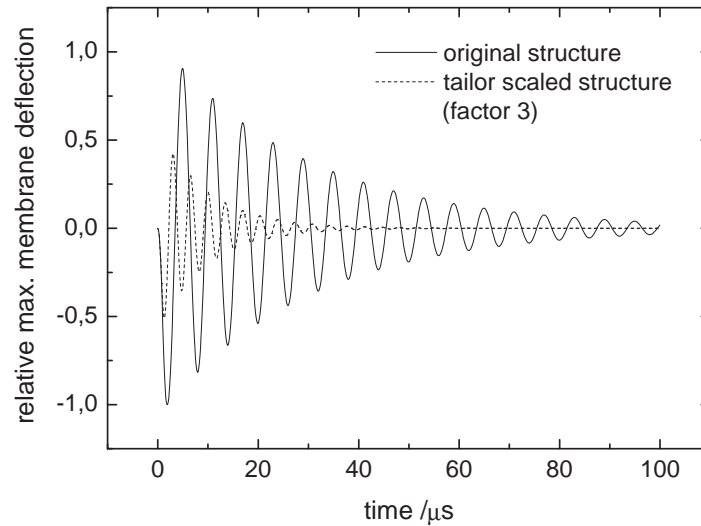
Fig. 5.7: Time response of due to a 1 μs gravitational shock impulse applied on a four suspension structure before and after scaling down.

from these results: (i) There is a (slight) reduction in the peak of the transient amplitude swing of the scaled down membrane, and (ii) the time taken for the peak to reduce to $1/e$ (36.8%) of the original peak, hereby referred to as the tuning delay is reduced by 66%. These point to higher stability and faster response on down-scaling. Air damping further limits this dynamic response in practice. A mechanical impulse applied to a device can cause permanent damage to the device or disruption of the normal function of the device. In Fig. 5.7 is a comparison of the response of the 4 suspension structure and the scaled down equivalent to a gravitational impulse or shock. The scaled down device has a 42.6% smaller initial maximum membrane displacement. This means that for the same impulse the scaled down membrane is less likely to swing and touch the facing membrane, an action that can result in undesirable effects such as short-circuit, adhesion or stiction, in MEMS language, and even breakage. It also takes 66% less time to settle down to an amplitude of $1/e$ of the initial level, after the application of the disturbance, hence the effect of the impulse disruption is overcome faster.

5.5   Summary

This chapter has pointed out the numerous advantages to be gained on scaling down struc-tures in general, and on scaling down vertical micro-cavity devices in particular. These are namely; reduced cost per device (if the same or comparable technological produc-tion process is applied), increased throughput, increased stability that results in increased yield , more reliability and improved performance. The reduced size also results in longer lifetimes due to reduced fatigue and also increases the feasibility of integration with other devices and incorporation of other functions. It has been shown that a kind of tailored scaling can be applied to the devices in question so as to almost exactly replicate the mechanical tuning efficiency resulting in smaller devices with practically the same me-chanical tuning performance, but with improved structural and performance stability as well as speed of response. The improvement in stability is gauged from the changes in eigen-frequencies, the transient response, and the response due a gravitational impulse. The FEM calculations are done with a quasi-3D method that is accurate, faster and re-quires less computing resources than the pure 3-D computations.

Chapter 6

Conclusions and outlook

Several new and useful results are presented in this dissertation. As already elaborated in the previous chapters, numerous electromechanical models are commonly encountered in the published literature, however because mechanical calculations involving non-linear force coupling and deformation get very complex as structures assume arbitrary shapes, the majority of the models deal only with regular geometries such as beams and square or circular membranes. The methods proposed and used in this work are applicable to a wide variety of structures of arbitrary geometries.

The FEM is a relatively old numerical analysis tool that is often shunned due to its huge demand on computer resources especially for calculations that require many degrees of freedom. But as the ordinary desktop computers have rapidly gained in processing powers in the last few years, this considerations has become progressively irrelevant. Finite element modelling software is therefore at the moment an attractive cost-effective choice for the type of work such as presented here. Further, the application of innovative problem simplifications can further alleviate the resource demand problem. One such case is found in chapter 3 where the quasi-3D electromechanical model presented can be applied in general for modelling thin structures by considering them as 2D objects with the third dimension factored in the calculation as a constant or mathematical function of space, time, etc. This drastically reduces the computation time as well as the processor memory required. The performance of the quasi-3D method agreed perfectly with standard benchmarks. In addition, appendix C is given as a testimony to the accuracy of the assumptions made in deriving the electro-mechanical coupling used in this work. The result obtained from a fully coupled, self-consistent electrostatic-mechanical model and that obtained from the model presented in this work differ by less than 1%.

The analytical closed-form models derived from the FEM calculations proved to be very accurate and even faster as they need only to be implemented as simple mathematical formulae and do not need the kind of geometrical structure definition-meshing-calculation procedure in FEM. Such models are useful in providing a quick insight at the beginning of the design phase and in some cases will be sufficient once tried and tested.

This dissertation also presents a systematic design procedure for the determination of the device dimensions based on given specifications. The procedure helps to define some limits based on sound physical and technological considerations and enables the device designer to get the design right the fist time and avoid unnecessary and costly prototyping and testing cycles.

Using the above mentioned methods and models several design optimisation studies were carried out yielding results with far reaching and useful implications. First, mechanical tuning characteristics of deflection versus voltage for various structural configurations and geometrical dimensions were determined for the range between the unactuated point up to the pull-in point. When each of the characteristics were normalised to their pull-in point deflection and voltage, all the resulting curves were practically perfectly identical. This result, that the normalised device deflection-voltage curve has an invariable profile, has the important consequence that the electro-mechanical tuning characteristic of any structure within a given class of devices is sufficiently defined by the pull-in point deflection and voltage. This can help to greatly simplify design work and analysis.

The second observation made was that the mechanical tuning range obtained by FEM model calculations is more than the commonly encountered value of one third of the cavity length determined from simple analytical calculations. The amount of the variation was shown to depend on the device geometry and attributed to the stress stiffening effect. Devices exhibiting more stress stiffening also showed relatively longer tuning ranges. This knowledge of a "bonus" range extension can be exploited in more accurate system design.

The distortion of the membrane plane is an undesirable effect that is inevitable in the designs presented in this work. However, it is shown that the choice of the size of the membrane relative to the suspensions and the structural configuration (i.e. 2, 3 or 4 suspensions) affects the amount by which the membrane will be distorted when actuated. Maintaining optically flat surfaces is important for the correct optical performance of the device, unless out-of-plane bends are desired by design.

The inclusion of the influence of residual axial and gradient stress in the calculations required the modification of the standard implementation of the 3D structural mechanics

computation mode supplied with the FEM software used, in addition to the electrostatic force coupling as before. Because residual stress has the effect of producing relatively large strains in the structures, more accurate results were obtained by using a large deformation model where the strains are considered as Green-Lagrange type rather than engineering strain. The accuracy of the model was validated using simple cantilever and beam models and comparing the results with those found in literature that apply other methods and software. The results obtained from this study demonstrated the huge impact that residual stress has on the tuning characteristics of the devices in question. Comparison of calculated and measured characteristics showed very good agreement. One example of such a comparison is given at the end of chapter 4.

The last set of key results of this work are from the scaling investigations. The aim of this exercise was to find out a scaling method that would produce a scaled device with the same mechanical tuning efficiency as the original and to determine what happens to the device stability with changing degree of scaling. A novel scaling technique was derived and used. The results show that the resulting scaled device replicates the mechanical tuning almost exactly. The advantages of down-scaling were seen in terms of improved switching speed and stability. The improvement in stability were gauged from the changes in eigen-frequencies, the transient response, and the response due a gravitational impulse. Solving the difficulty in realising down-scaled devices with membrane thickness in the sub-100nm range is subject of on going work. When this can be reliably and cost-effectively done, it will be time to reap the benefits of down-scaling such as higher yields from more devices fabricated per production run, stabler devices with longer lifetimes due to less material fatigue, etc.

It is stated above that the normalised tuning curve for the class of devices considered in this work is practically invariable. The investigation considered only one material system in this work and the quasi-3D FEM model used was without residual stress. It would be interesting to see how far this fixed profile rule applies in other material systems and configurations, and more so when residual stress is included. Of course the 3D FEM model with residual stress can be used for this assignment, however, it is relatively tedious and time consuming. The challenge here is to improve the quasi-3D model by including residual stress. An alternative would be to develop more sophisticated analytical closed-form models covering a wider range of designs.

The devices presented in this work have straight, beam-like suspensions that are constrained at both ends. Such a setup is rather sensitive to the effects of residual stress and changes in temperature, which can easily cause out-of-plane deformations. This kind of

deformation was often seen in the WLI images or SEM micrographs of the fabricated devices. Designs more immune to such effects can be tried in the future. Such designs would be, for instance, membranes with S-shaped or zigzag suspensions instead of the straight ones, where technologically possible. Preliminary trials in the course of this work have shown promising results in this regard.

Abbreviations and symbols

ADSL	Asymmetric digital subscriber line
ASG	Apodised sample garting
ATM	Asynchronous transfer mode
AWG	Arrayed waveguide grating
CATV	Cable television
CPU	Central processing unit
CVD	Chemical vapour deposition
DBR	Distributed Bragg reflector
DEMUX	Demultiplexer
DG	Diffraction grating
DWDM	Dense wavelength division multiplexing
EM	Electromagnetic
FBG	Fibre Bragg grating
FEA	Finite element analysis
FEM	Finite element method
FSR	Free spectral range
FTTH	Fibre-to-the-home
FP	Fabry-Pérot
FWHM	Full wave half maximum
IP	Internet protocol
LVF	Linear variable filter
MAN	Metropolitan area network
MBE	Molecular beam epitaxy
MEMS	Micro-electromechanical systems
MOEMS	Micro-opto-electromechanical systems
MUX	Multiplexer
MZI	Mach-Zehnder interferometer

OADM	Optical add-drop multiplexer	
OEO	Optical-electrical-optical	
ODE	Ordinary differential equation	
OXC	Optical cross connector	
OPL	Optical path length	
PDE	Partial differential equation	
PML	Perfectly matched layer	
SDH	Synchronous digital hierarchy	
SONET	Synchronous optical network	
RAM	Random access memeory	
ROADM	Reconfigurable optical add-drop multiplexer	
RCLED	Resonant cavity light emitting diode	
SEM	Scanning electron microscope	
TDM	Time division multiplexing	
TIF	Tilt interference filter	
TPW	Twisted pair copper wire	
VCSEL	Vertical cavity surface emitting laser	
VCSOA	Vertical cavity semiconductor optical amplifier	
VCOD	Vertical cavity optical detector	
WDM	wavelength division multiplexing	
WLI	White-light interferometer	
nD	n-dimensional, ($n \in \{1, 2, 3\}$)	
A	area of membrane	m^2
a	absorption coefficient in PDE	
α_d	normalised power loss	dB
α	absorption coefficient	m^{-1}
$\hat{\alpha}$	conservative flux in PDE	
A_1, A_2	power loss coefficients in etalon	
β	convection coefficient	
c	damping factor	kgs^{-1}
c_{cr}	critical damping factor	kgs^{-1}
c_0	velocity of light in free space	ms^{-1}
$\hat{c}$	diffusion coefficient	
D	flexural rigidity	Nm
d	diameter of mirror	m

d_a	mass transfer coefficient	
δ	membrane deflection from original position	m
$\hat{\delta}$	optical phase in one round trip in etalon	rad
e	Napier's constant	~ 2.71828
E	Young's modulus of elasticity	Nm^{-2}
E_{inc}	incident electric field intensity	Vm^{-1}
E_{ref}	reflected electric field intensity	Vm^{-1}
E_{trans}	transmitted electric field intensity	Vm^{-1}
$\mathbf{E}$	electric field vector	Vm^{-1}
$\mathbf{E_i}$	incident electric field vector	Vm^{-1}
$\mathbf{E_r}$	reflected electric field vector	Vm^{-1}
$\mathbf{E_t}$	transmitted electric field vector	Vm^{-1}
ε_i	mechanical strain ($i \in \{x, y, z\}$)	
ε	permittivity	F/m
ε_0	permittivity of free space	F/m
ε_r	relative permittivity	
F	finesse	
f	frequency	Hz
f_{es}	electrostatic force	N
$\hat{f}$	source term in PDE	
f_0	resonant frequency	Hz
$f(t)$	forcing function	N
G	shear modulus	Nm^{-2}
$\hat{g}$	boundary source	
g	instantaneous separation between the membranes	m
g_0	initial separation between the membranes	m
γ_{ij}	shear strain ($i, j \in \{x, y, z\}$)	
γ	conservative flux term	
h	plate thickness	m
$\mathbf{H}$	magnetic field vector	A/m
K_x, K_y, K_z	mechanical body forces	Nm^{-3}
κ^2	shear correction factor in Mindlin theory	
κ	extinction coefficient	m^{-1}
k_{eff}	effective spring constant	Nm^{-1}
k_t	transverse scaling factor	
k_l	lateral scaling factor	

l	length of suspensions	m
L	separation of reflecting surfaces in etalon	m
λ	wavelength	m
λ_e	eigen-vector	
λ_{mat}	wavelength in material	m
m	mass	kg
μ_L	Lamé constant	Nm^{-2}
$\hat{\mu}$	Lagrange multiplier	
μ	permeability	H/m
μ_0	permeability of free space	H/m
μ_r	relative permeability	
M_x, M_y, M_{xy}	mechanical moments per unit length of a plate	N
n	refractive index	
$\bar{n}$	complex refractive index	
ν	Poisson's ratio	
N_F	Fresnel number	
$\mathbf{n}$	normal vector	
ω	angular frequency	rad/s
ω_0	undamped angular frequency	rad/s
Ω	computational domain	
$\partial\Omega$	computational domain boundary	
p_i	force per unit area in i-direction ($i \in \{x, y, z\}$)	Nm^{-2}
$\Psi = (\psi_x, \psi_y)$	in-plane vector of rotations in 2D Mindlin theory	
φ	initial phase of EM wave	rad
Q	electric charge	C
Q_x, Q_y	shear forces per unit length in a plate	N/m
q	boundary absorption coefficient	
ρ	material density	kgm^{-3}
r	radius of membrane	m
R, R_1, R_2	power reflection coefficients in etalon	
r_1, r_2	complex reflection coefficients in etalon	
σ_i	mechanical stress ($i \in \{x, y, z\}$)	Nm^{-2}
σ	conductivity	Sm^{-1}
τ_{ij}	shear stress ($i, j \in \{x, y, z\}$)	Nm^{-2}
t	time	

T, T_1, T_2	power transmission coefficients in etalon	
t_1, t_2	complex transmission coefficients in etalon	
θ	angle of incidence of wave on etalon surface	rad
u_i	mechanical deformation components ($u_i \in u, v, w$)	m
u	dependent variable in PDE	
$\mathbf{u}$	total displacement in 2D Mindlin theory	m
V	applied voltage	V
V_{PI}	pull-in voltage	V
υ	velocity	ms^{-1}
w	width of suspensions	m
ζ	damping ratio	

List of publications

E. Ataro , C. Prott, F. Römer and H. Hillmer, "Tailored Scaling: A possibility to improve the performance of ultra-wide continuously tunable photonic devices", *Applied Physics B*, **Vol. 79**, pp. 87-93, (2004).

C. Prott, F. Römer, **E. O. Ataro**, J. Daleiden, S. Irmer, A. Tarraf and H. Hillmer, "Modeling of Ultra-Widely Tunable Vertical Cavity Air-Gap Filters and VCSEL's", *IEEE Journal of Selected Topics in Quantum Electronics*, **Vol. 9**, No. 3, pp. 918-928 (2003).

J. Daleiden, A. Tarraf, S. Irmer, F. Römer, C. Prott, **E. Ataro**, M. Strassner and H. Hillmer, "Wide and continuous wavelength tuning of micro-cavity devices for optoelectronic applications", *Journal of Microlithography, Microfabrication and Microsystems*, **Vol. 2**, No. 4, pp. 265-274, (October, 2003).

H. Hillmer, J. Daleiden, C. Prott, F. Römer, S. Irmer, **E. Ataro**, A. Tarraf, D. Gutermuth, I. Kommallein and M. Strassner, "Ultra-wide continuously tunable 1.55μm vertical air-cavity wavelength-selective elements for VCSELs using micromachined electrostatic actuation", *Proceedings of SPIE International Symposium ITCom 2003*, Orlando, Florida USA, **Vol. 5246**, pp. 18-32, ISBN: 0-8194-5140-1, (7-11 September, 2003).

H. Hillmer, J. Daleiden, C. Prott, F. Römer, S. Irmer, A. Tarraf, **E. Ataro** and M. Strassner, "Potential of micromachined photonics: miniaturization, scaling, and applications in continuously tunable vertical air-cavity filters (Invited). "*SPIE Proc. series 4947, Photonics Fabrication Europe*, Brugge/Belgium, **Vol. 4947-24**, pp. 196 - 211, ISBN: 0-8194-4745-5 (2003).

H. Hillmer, J. Daleiden, C. Prott, S. Irmer, F. Römer, **E. Ataro**, A. Tarraf, H. Rühling, M. Maniak and M. Strassner, "Bionics: Precise color tuning by interference in nature and technology - applications in surface-micromachined 1.55μm vertical air-cavity filters",

SPIE Proc. series 4983, Photonics West: Micromachining and Microfabrication, ISBN: 0-8194-4840-0 (2003).

J. Daleiden, S. Irmer, **E. Ataro**, C. Prott, V. Rangelov, F. Römer, M. Strassner, A. Tarraf, and H. Hillmer, "Continuously tunable air-gap micro-cavity devices for optical communication systems (invited)", *Proceedings of the SPIE ITCom 2002*, **Vol. 4871**, pp.145-59, ISBN: 0-8194-4654-8 (2002).

C. Prott, F. Römer, **E. Ataro**, J. Daleiden, S. Irmer, M. Strassner, A. Tarraf and H. Hillmer, "Model calculations of vertical cavity air-gap filters and VCSEL's for ultra-wide continuous tuning", *Proceedings of the International Conference on Numerical Simulation of Semiconductor Optoelectronic Devices*, Swiss Federal Institute of Technology (ETH), Zürich, Switzerland, www.nusod.org, (September 25-27, 2002).

A. Tarraf, J. Daleiden, F. Römer, C. Prott, V. Rangelov, S. Irmer, **E. Ataro** and H. Hillmer, "A novel low-cost tunable dielectric air-gap filter", *Proceedings of the Optical MEMS Conference*, Lugano, Switzerland, ISBN: 0-7803-7595-5, pp. 175, (20-23 August, 2002).

A. Tarraf, J. Daleiden, S. Irmer, V. Rangelov, F. Römer, C. Prott, **E. Ataro**, H. Hillmer, T. Fuhrmann, T. Spehr and J. Salbeck, "A novel low-cost and simple fabrication technology for tunable dielectric active and passive optical air-gap devices", *Proceedings of Photonic Fabrication Europe, 2002*, Brugge Belgium, **Vol. 4945-2**, pp. 9-20 ISBN: 0-8194-4745-5 (2002).

J. Daleiden, A. Tarraf, **E. Ataro**, N. Chitica, S. Irmer, C. Prott, F. Römer, M. Strassner and H. Hillmer, "Micromechanically Tunable Filters for Optical Communication Systems", *Proceedings of the 1st Int. Workshop on Optical MEMS and Integrated Optics, Dortmund, Germany*, pp. 7-10 (11-12 June, 2001).

J. Daleiden, S. Irmer, H. Hohmann, D. Feili, A. Tarraf, **E. Ataro**, F. Römer, C. Prott and H. Hillmer, "Trockenätzen von phosphidischen III-V Halbleitern", Invited talk, *Workshop on dry etching for III-V semiconductors, Ulm, Germany*, (April 26-27, 2001).

H. Hillmer, C. Prott, J. Daleiden, F. Römer, S. Irmer, A. Tarraf, **E. Ataro** and M. Strassner, "142-nm electrostatically actuated tuning using surface micro-machined vertical air-cavity wavelength selective elements for applications in 1.55 μm VCSELs. "*SPIE Proc. series 4994, Photonics West 2003: Integrated Optoelectronic Devices*, **Vol. 4994-7**, pp. 32 - 43, ISBN: 0-8194-4841-9 (2003).

References

[1] Miniwatts International Inc., "World internet usage and population statistics." http://www.internetworldstats.com, September 2004.

[2] J. Stafford, "Nemi highlights areas of growth for optoelectronics in network technology," *Optoelectronics Manufacturing*, vol. **2**, no. 3, 2003.

[3] R. Ramswami, "Optical fiber communication: From transmission to networking," *IEEE Communications Magazine*, vol. **40** , pp. 138–147, 2002.

[4] P. Green, "Progress in optical networking," *IEEE Communications Magazine*, vol. **39**, pp. 54–61, 2001.

[5] J. A. Walker, "The future of MEMS in telecommunications networks," *Journal of Micromechanics and Microengineering*, vol. **10**, pp. R1–R7, 2000.

[6] P. Griffin, "The Photonics Future," *GEC Review*, vol. **14**, no. 1, pp. 3–7, 1990.

[7] Lucent Technologies, "Dense wavelength division multiplexing." www.iec.com, 2004.

[8] C. A. Brackett, "Dense wavelength division multiplexing networks: Principles and applications," *IEEE Journal on Selected Areas in Communications*, vol. **8**, no. 6, pp. 948–64, 1990.

[9] J. Cavazos, "Insight into the metro's future (part 1)," Tech. rep., Frost and Sullivan, www.frost.com, August 2003.

[10] A. H. Gnauck, G. Raybon, S. Chandrasekhar, J. Leuthold, C. Doerr, L. Stulz, A. Agarwal, S. Banerjee, D. Grosz, S. Hunsche, A. Kung, A. Marhelyuk, D. Maywar, M. Movassaghi, X. Liu, C. Xu, , X. Wei, and D. M. Gill, "2.5 TB/s (64x42.7

GB/s) transmission over 40x100 km NZDSF using RZ-DPSK format and all-raman-amplified spans," in *Proceedings of Optical Fiber Communication (OFC) Conference and Exhibit 2002*, pp. FC2/1–3, 2002.

[11] S. Bigo, Y. Frignac, G. Charlet, W. Idler, S. Borne, H. Gross, R. Dischler, W. Poehlmann, P. Tran, C. Simonneau, D. Bayart, G. Veith, A. Jourdan, and J. P. Hamaide, "10.2 TBit/s (256x42.7 GBit/s PDM/WDM) transmission over 100 km teralight^{TM} fiber with 1.28 Bit/s/Hz spectral efficiency," in *Proceedings of Optical Fiber Communication (OFC) Conference and Exhibit 2001*, pp. PD25/1–3, 2001.

[12] K. Fukuchi, T. Kasamatsu, M. Morie, R. Ohhira, T. Ito, K. Sekiya, D. Ogasahara, and T. Ono, "10.92-TB/s (273x40-GB/s) triple-band ultra-dense WDM optical-repeatered transmission experiment," in *Proceedings of Optical Fiber Communication (OFC) Conference and Exhibit 2001*, pp. PD24/1–3, 1991.

[13] Heise online news, "170 GBit/s pro Wellenlängen-Kanal in französischem Glasfasernetz übertragen." Heise Zeitschriften Verlag, www.heise.de/newsticker/meldung/53960, December 2004.

[14] N. Miron, "Optical interference filters," *Fibre Optic Technology*, pp. 40–2, May 2002.

[15] C. Chang-Hasnain, "Tunable VCSELs: Enabling wavelength-on-demand in metro networks," *Compound Semiconductor Magazine*, vol. **7**, June 2001.

[16] J. Sorosiak, "Works to be square: Optical filters and their thin films," *Fibre Optic Technology*, December 2003.

[17] X. Zhang and M. McLean, "Thin film WDM filters: Back to the basics of modularity and scalability," *Fibre Optic Technology*, September 2002.

[18] V. A. Aksyuk, S. Arney, N. R. Basavanhally, D. J. Bishop, C. A. Bolle, C. C. Chang, R. Frahm, A. Gasparyan, J. V. Gates, R. George, C. R. Giles, J. Kim, P. R. Kolodner, T. M. Lee, D. T. Neilson, C. Nijander, C. J. Nuzman, M. Paczkowski, A. R. Papazian, R. Ryf, H. Shea, and M. E. Simon, "238x238 surface micromachined optical crossconnect with 2dB maximum loss," in *Proceedings of Optical Fiber Communication (OFC) Conference and Exhibit 2002*, pp. FB9/1–3, 2002.

[19] A. Neukermans and R. Ramaswami, "MEMS technology for optical networking applications," *IEEE Communications Magazine*, vol. **39**, pp. 62–69, 2001.

[20] M. C. Wu, "Micromachining for optical and optoelectronic systems," *Proceedings of IEEE*, vol. **85**, pp. 1833–56, 1997.

[21] P. Duggan, M. Tremblay, N. Rowhani, and M. Ner, "Tunable filters provide flexibility for agile networks," *WDM Solutions*, vol. **5**, pp. 9–12, 2003.

[22] S. Irmer, J. Daleiden, V. Rangelow, C. Prott, F. Römer, M. Strassner, A. Tarraf, and H. Hillmer, "Ultra-low biased widely continuously tunable Fabry-Pérot filter," *IEEE Photonics technology Letters*, vol. **15**, no. 3, pp. 434–6, 2003.

[23] C. F. R. Mateus, C.-H. Chang, L. Chrotowski, S. Yang, D. Sun, R. Pathak, and C. J. Chang-Hasnain, "Widely tunable tortional optical filter," *IEEE Photonics Technology Letters*, vol. **14** , no. 6, pp. 819–21, 2002.

[24] A. Spisser, R. Ledantec, C. Seassal, J. Leclercq, D. Rondi, T.Benyattou, G. Guillot, R. Blondeau, and P. Viktorovitch, "Highly selective and widely tunable 1.55-μm InP/air-gap micromachined Fabry-Pérot filter for optical communications," *IEEE Photonics Technology Letters*, vol. **10**, pp. 1259–61, 1998.

[25] P. Tayebati, P. Wang, D. Vakhshoori, and R. Sack, "Widely tunable Fabry-Pérot filter using Ga(Al)As-AlO$_x$ deformable mirrors," *IEEE Photonics Technology Letters*, vol. **10**, pp. 394–6, 1998.

[26] J. Peerlings, A. Dehe, A. Vogt, M. Tilsch, C. Hebeler, F. Langenhan, P. Meissner, and H. Hartnagel, "Long resonator micromachined tunable GaAs-AlAs Fabry-Pérot filter," *IEEE Photonics Technology Letters*, vol. **9**, pp. 1235–7, 1997.

[27] E. Vail, M. Wu, G. Eng, L. Li, and C. Chang-Hasnain, "GaAs micromachined widely tunable Fabry-Pérot filters," *Electronics Letters*, vol. **31**, pp. 228–9, 1995.

[28] A. Tarraf, F. Riemenschneider, M. Strassner, J. Daleiden, S. Irmer, H. Halbritter, H. Hillmer, and P. Meissner, "Continuously tunable 1.55 μm VCSEL implemented by precisely curved dielectric top DBR involving tailored stress," *IEEE Photonics Technology Letters*, vol. **16**, pp. 720–2, 2004.

[29] C. Chang-Hasnain, "Tunable VCSEL," *IEEE Journal of Selected Topics in Quantum Electronics*, vol. **6**, pp. 978–87, 2000.

[30] P. Tayebati, P. D. Wang, D. Vakhshoori, C. C. Lu, M. Azimi, and R. N.Sacks, "Half-symmetric cavity tunable microelectromechanical VCSEL with single spatial mode," *IEEE Photonics Technology Letters*, vol. **10**, pp. 1679–81, 1998.

[31] M. C. Larson, A. R. Massengale, and J. S. H. Jr., "Continuously tunable micromachined vertical-cavity surface-emitting laser with 18 nm wavelength range," *Electronics Letters*, vol. **32**, pp. 330–2, 1996.

[32] M. S. Wu, E. C. Vail, G. S. Li, W. Yuen, and C. J. Chang-Hasnain, "Tunable micromachined vertical cavity surface emitting laser," *Electronics Letters*, vol. **31** , pp. 1671–2, 1995.

[33] J. Cheng, J. Zhe, and X. Wu, "Analytical and finite element model pull-in study of rigid and deformable electrostatic microactuators," *Journal of Micromechanics and Microengineering*, vol. **14** , no. 1.

[34] T. Kimura, E. S. Björlin, J. Piprek, and J. E. Bowers, "High-temperature characteristics and tunability of long-wavelength vertical-cavity semi-conductor optical amplifiers," *IEEE Photonics Technology Letters*, vol. **15**, pp. 1501–3, 2003.

[35] R. Lewen, K. Streubel, A. Karlsson, and S. Rapp, "Experimental demonstration of a multifunctional long-wavelength vertical-cavity laser amplifier-detector," *IEEE Photonics Technology Letters*, vol. **10**, pp. 1067–9, 1998.

[36] J. Peerlings, R. Riemenschneider, V. N. Kumar, M. Strassner, V. Scheuer, J. Pfeiffer, K. Mutamba, J. Daleiden, H. Hartnagel, S. Herbst, and P. Meissner, "Two-chip InGaAs-InP Fabry-Pérot p-i-n receiver for WDM systems," *IEEE Photonics Technology Letters*, vol. **11**, pp. 260–2, 1999.

[37] G. L. Christensen, A. T. T. D. Tran, Z. H. Zhu, Y. H. Lo, M. Hong, J. Mannaerts, and R. Bhat, "Long-wavelength resonant vertical-cavity LED/photodetector with a 75-nm tuning range," *IEEE Photonics Technology Letters*, vol. **9**, pp. 725–7, 1997.

[38] P. Bienstman and R. Baets, "The RC^{2}LED: A novel resonant-cavity LED design using a symmetric resonant cavity in the outcoupling reflector," *IEEE Journal of Quantum Electronics*, vol. **36**, no. 6, pp. 669–73, 2000.

[39] E. F. Schubert, Y. H. Wang, A. Y. Cho, L. W. Tu, Y. Cho, and G. J. Zydzik, "Resonant cavity light-emitting diode," *Applied Physics Letters*, vol. **60** , no. 8, pp. 921–3, 1992.

[40] W. S. Rabinovich, T. H. Stievater, N. A. Papanicolaou, D. S. Katzer, and P. G. Goetz, "Demonstration of a microelectromechanical tunable asymmetric Fabry-Pérot quantum well modulator," *Applied Physics Letters*, vol. **83**, no. 10, pp. 1923–5, 2003.

[41] J. Daleiden and H. Hillmer, "Multiple air-gap filters and constricted mesa lasers - material processing meets the front of optical device technology," *Applied Physics B - Lasers and Optics*, vol. **76**, pp. 821–32, 2003.

[42] S. Toyoda, N. Ooba, K. Kitoh, and T. Kurihara, "Wide tuning range and low operating power AWG-based thermo-optic wavelength tunable filter using polymer waveguide," *Electronics Letters*, vol. **37**, no. 18, pp. 1130–2, 2001.

[43] K. O. Hill and G. Meltz, "Fibre Bragg grating technology fundamentals and overview," *Journal of Lightwave Technology*, vol. **15** , pp. 1263–76, 1997.

[44] C. R. Giles, "Lightwave applications of fibre Bragg gratings," *Journal of Lightwave Technology*, vol. **15** , pp. 1391–1404, 1997.

[45] T. Kimura, N. Fujimura, and N. Kanbara, "Wide range tunable filter module based on MEMS tilt mirror," in *Technical Digest of the IEEE/LEOS 2004 conference on Optical MEMS and their applications, Takamatsu, Kagawa, Japan*, pp. 12–3, August 2004.

[46] J. Provine, D. Horsley, and N. Tien, "MEMS-based non-dispersive IR gas detection system utilising a linear variable filter," in *Technical Digest of the IEEE/LEOS 2004 conference on Optical MEMS and their applications, Takamatsu, Kagawa, Japan*, pp. 42–3, August 2004.

[47] S. J. B. Yoo, "Wavelength conversion technologies for WDM network applications," *Journal of Lightwave Technology*, vol. **14**, no. 6, pp. 955–66, 1996.

[48] J. D. Berger and D. Anthon, "Tunable MEMS for optical networks," *Optics and Photonics News*, vol. **14**, pp. 43–9, March 2003.

[49] S. Matsuo, Y. Yoshikuni, T. Segawa, Y. Ohiso, and H. Okamoto, "A widely tunable optical filter using ladder-type structure," *IEEE Photonics Technology Letters*, vol. **15**, no. 8, pp. 1114–6, 2003.

[50] J. Philip, T. Jaykumar, P. Kalyasundaram, and B. Raj, "A tunable optical filter," *Material Science and Technology*, vol. **14**, pp. 1289–94, 2003.

[51] T. Segawa, S. Matsuo, Y. Ohiso, T. Ishii, and H. Suzuki, "Apodised sampled grating using InGaAsP/InP deep ridge waveguide with vertical-groove surface grating," *Electronics Letters*, vol. **40**, no. 13, pp. 804–5, 2004.

[52] W. Moench, J. Dehnert, and H. Zappe, "Tunable polymer Fabry-Pérot-filters," in *Technical Digest of the IEEE/LEOS 2004 conference on Optical MEMS and their applications, Takamatsu, Kagawa, Japan*, pp. 8–9, August 2004.

[53] A. P. K. Madhumita Datta, Marcel W. Pruessner and R. Ghodssi, "Design of MEMS -tunable novel monolithic optical filters in InP with horizontal Bragg mirors," *Solid State electronics*, vol. **48** , pp. 1959–63, 2004.

[54] D. Anderson, "Optical filters fill many roles," *WDM Solutions*, vol. **3**, no. 6, pp. 97–9, 2001.

[55] S. O. Kassap, *Optoelectronics and Photonics*. New Jersey: Prentice Hall, 2001.

[56] W. Vogel and M. Berroth, "Tunable liquid crystal Fabry-Pérot filters," in *Proc. SPIE Vol. 4944: Integrated Optical Devices: Fabrication and Testing* (G. C. Righini, ed.), pp. 293–302, 2003.

[57] Precision Photonics Corporation, "Basic physics and design of etalons." www.precisionphotonics.com, April 2003.

[58] J. F. Mulligan, "Who were Fabry and Pérot?," *American Journal of Physics*, vol. **66**, no. 9, pp. 797–802, 1998.

[59] The Nobel Foundation, *Nobel Lectures in Physics: 1901-1995*. New Jersey, London, Singapore, Hong Kong, Taipei and Bangalore: World Scientific Publishing Company, 1998.

[60] S. F. Yu, *Analysis and design of vertical cavity surface emitting lasers*. New Jersey: Wiley and sons, 2003.

[61] H. Koegelnik and C. V. Shanks, "Coupled wave theory of distributed Bragg reflector lasers," *Journal of Applied Physics*, vol. **43**, no. 5, pp. 2327–35, 1972.

[62] P. Debernadi and G. P. Bava, "Coupled mode theory: A powerful tool for analysing complex VCSELs and designing advanced features," *IEEE Journal of Selected Topics in Quantum Electronics*, vol. **9**, no. 3, pp. 905–17, 2003.

[63] T. E. Sale, "Cavity and reflector design for vertical cavity surface emitting lasers," *IEE Proceedings on Optoelectronics*, vol. **142**, no. 1, pp. 37–43, 1995.

[64] R. D. Cook, *Finite Element Modeling for Stress Analysis*. New York, Chichester, Brisbane, Toronto, Singapore: John Wiley & Sons, Inc., 1995.

[65] Comsol, *FEMLAB user's manual, FEMLAB modelling guide*. Comsol AB, 2004.

[66] M. Born and E. Wolf, *Principles of Optics*. Cambridge university Press, 7th ed., 1999.

[67] H. A. Macleod, *Thin-film Optical filters*. Bristol, Philadelphia: Institute of Physics, 3rd ed., 2001.

[68] J.-P. Berenger, "A perfectly matched layer for the absorption of EM waves," *J. Computational Physics*, vol. **114**, pp. 185–200, October 1994.

[69] J. Jin, *The Finite Element Method in Electromagnetics*. New York: John Wiley & Sons Inc, 1993.

[70] Z. S. Sacks, D. M. Kingslande, R. Lee, and J.-F. Lee, "A perfectly matched anisotropic absorber for use on absorbing boundary conditions," *IEEE Transactions on Antennas and Propagation*, vol. **43**, pp. 1460–3, Dec 1995.

[71] S. D. Gedney, "An anisotropic PML-absorbing medium for the truncation of FDTD lattices," *IEEE Transactions on Antennas and Propagation*, vol. **44**, pp. 1630–9, Dec 1996.

[72] S. A. Cummer, "A simple, nearly perfectly matched layer for general electromagnetic media," *IEEE microwave and wireless components letters*, vol. **13**, pp. 128–30, March 2003.

[73] A. MacLeod, "The early days of optical coatings," *Journal of Optics A: Pure Applied Optics*, vol. **1**, pp. 779–783, 1999.

[74] W. Geffcken, "Interferenzlichtfilter, German patent no.716153," 1939.

[75] F. Römer, *Doktorarbeit*. Universität Kassel, Kassel, Germany, (to be published).

[76] T. E. Sale, *Vertical Cavity Surface Emitting Lasers*. New York, Chichester, Toronto, Brisbane, Singapore: John Wiley & Sons Inc., first ed., 1995.

[77] H. Hillmer, J. Daleiden, C. Prott, F. Römer, S. Irmer, A. Tarraf, E. Ataro, and M. Strassner, "Potential of micromachined photonics: miniaturization, scaling, and applications in continuously tunable vertical air-cavity filters. (invited)," in *Proceedings of SPIE vol. 4947 - Laser Diodes, Optoelectronic Devices, and Heterogenous Integration* (A. Driessen, R. G. Baets, J. G. McInerney, and E. Suhir, eds.), (Brugge/Belgium), pp. 196 – 211, SPIE, March, 2003.

[78] H. Hillmer, J. Daleiden, C. Prott, F. Römer, S. Irmer, V. Rangelov, A. Tarraf, S. Schüler, and M. Strassner, "Potential for micromachined actuation of ultra-wide continuously tunable optoelectronic devices," *Applied Physics B*, vol. **75**, pp. 3–13, 2002.

[79] K. M. Liew, C. M. Wang, Y. Xiang, and S. Kitipornchai, *Vibration of Mindlin Plates*. Amsterdam, Lausanne, New York, Oxford, Shannon, Singapore, Tokyo: Elsevier, 1998.

[80] O. C. Zienkiewicz and R. L. Taylor, *The Finite Element Method: Solid Mechanics*. Oxford: Butterworth-Heinemann, 5th ed., 2002.

[81] P. M. Osterberg and S. D. Senturia, "M-test: A test chip for MEMS material property measurement using electrostatically actuated test structures," *Journal of Microelectromechanical Systems*, vol. **6**, no. 2, pp. 107–18, 1997.

[82] K. F. Graff, *Wave Motion in Elastic Solids*. New York: Dover, 1991.

[83] N. G. Stephen, "Mindlin plate theory: Best shear coefficient and higher spectra validity," *Journal of Sound and Vibration*, vol. **202**, pp. 539–53, 1997.

[84] NAFEMS, *The Standard NAFEMS Benchmarks*. Glasgow, UK: National Agency for Finite Element Methods and Standards, August 1989.

[85] J. Barlow and G. A. O. Davis, *Selected Benchmarks in Structural and Thermal Analysis*. Glasgow, UK: National Agency for Finite Element Methods and Standards, October 1986.

[86] H. C. Nathanson, W. E. Newell, R. A. Wickstrom, and J. R. D. Jr, "The resonant gate transistor," *IEEE Transactions on Electronic devices*, vol. **14**, pp. 117–33, 1967.

[87] K. E. Petersen, "Dynamic micromechanics on Si: Techniques and devices," *IEEE Transactions on Electronic Devices*, vol. **25**, pp. 1241–50, 1978.

[88] H. A. C. Tilmans and R. Legtenberg, "Electrostatically driven vacuum-encapsulated polysilicon resonators: Part II. theory and performance," *Sensors and Actuators A*, vol. **45**, pp. 67–84, 1994.

[89] S. Pamidighantam, R. Puers, and K. Baert, "Pull in voltage analysis of electro-statically actuated beam structures with fixed-fixed and fixed-free end conditions," *Journal of Micromechanics and Microengineering*, vol. **12**, pp. 458–64, 2002.

[90] J. Cheng, J. Zhe, X. Wu, K. Farmer, V. Modi, and L. Frechette, "Analytical and FEM simulation pull-in study on deformable electrostatic micro actuators," in *Technical Proceedings of the 2002 International Conference on Modeling and Simulation of Microsystems, Puerto Rico, U.S.A*, (Boston, Geneva, San Francisco), pp. 298 – 301, 2002 Computational Publications, April 22-25 2002.

[91] J. Zhe, X. Wu, J. Cheng, J. Wang, K. R. Farmer, L. Frechette, and V. Modi, "Analytical pull-in study on non-deformable electrostatic micro actuators," in *Technical Proceedings of the 2002 International Conference on Modeling and Simulation of Microsystems, Puerto Rico, U.S.A*, (Boston, Geneva, San Francisco), pp. 287–290, 2002 Computational Publications, April 22-25 2002.

[92] C. O'Mahony, M. Hill, R. Duane, and A. Mathewson, "Analysis of electromechanical boundary effects on the pull-in of micromachined fixed-fixed beams," *Journal of Micromechanics and Microengineering*, vol. **13**, pp. S75–S80, 2003.

[93] W. E. Newell, "Miniaturisation of tuning forks," *Science*, vol. **161** , pp. 1320–6, 1968.

[94] D. W. Burns, J. D. Zook, R. D. Horning, W. R. Herb, and H. Guckel, "Sealed cavity resonant microbeam pressure sensor," *Sensors and Actuators*, vol. **48** , pp. 179–86, 1995.

[95] D. W. Burns, J. D. Zook, R. D. Horning, W. R. Herb, and H. Guckel, "Sealed cavity resonant accelerometer pressure sensor," *Sensors and Actuators*, vol. **53** , pp. 249–55, 1996.

[96] E. Ataro, C. Prott, F. Römer, and H. Hillmer, "Tailored scaling: A possibility to improve the performance of ultra-wide continously tunable photonic devices," *Applied Physics B - Lasers and Optics*, vol. **79**, pp. 87–93, 2004.

[97] C. F. R. Mateus, C.-H. Chang, S. Yang, D. Sun, R. Pathak, and C. J. Chang-Hasnain, "Tunable micromechanical optical filter using a tortional structure,"

[98] E. S. Huang and S. D. Senturia, "Extending the travel range of analog-tuned electrostatic actuators," *Journal of Microelectromechanical Systems*, vol. **8**, no. 4, pp. 497–505, 1999.

[99] X.-T. Wu, R. A. Brown, S. Mathews, and K. R. Farmer, "Extending the travel range of electrostatic micro-mirrors using insulator coated electrodes," in *Proceedings of the IEEE/LEOS international Conference on Optical MEMS, Kauai, Hawaii*, pp. 151–4, Aug 21-24 2000.

[100] R. Sattler, P. Voigt, H. Pradel, and G. Wachutka, "Innovative design and modelling of a micromechanical relay with electrostatic actuation," *Journal of Micromechanics and Microengineering*, vol. **11**, pp. 428–33, 2001.

[101] T. Lofnes, V. Ziemann, and A. Ferrari, "Analytical design of a confocal resonator," Tech. Rep. TSL-Note-2003-56, European Organisation for Nuclear Research, Cern-AB Division, Geneva, October 14 2003.

[102] S. Adachi, *Physical Properties of III-V Semiconductor Compounds*. New Jersey: John Wiley and Sons, 1992.

[103] I. C. Noyan, "Defining residual stress in thin film structures," *Advances in X-Ray Analysis*, vol. , pp. 461–73, 1995.

[104] F. Kandil, J. Lord, A. T. Fry, and P. V. Grant, "Review of residual stress measurement methods - a guide to technique selection," Tech. Rep. Report MATC(A)04, NPL (National Physical Laboratory), Teddington, Middlesex, UK, Feb 2001.

[105] E. O'Brien, "Residual stress- friend or foe: A civil aircraft perspective," in *Technical Proceedings of the 2002 International Conference on Residual stress, ICRC-6, Oxford, UK*, (Oxford, UK), pp. 13–21, ICRS, 10-12 July 2000.

[106] P. J. Withers and H. K. D. H. Bhadeshia, "Residual stress part 1 - measurement techniques," *Material Science and Technology*, vol. **17** , pp. 355–65, 2001.

[107] P. J. Withers and H. K. D. H. Bhadeshia, "Residual stress part 2 - nature and origins," *Material Science and Technology*, vol. **17** , pp. 366–75, 2001.

[108] K. O'Donnell, J. Kostetsky, and R. S. Post, "Stress control in NiV, Cr and TiW thin films used in UBM and backside metallization," in *Proceedings of IMAPS Flip-chips Conference 2002*, 2002.

[109] W. Fang and J. A. Wicket, "Determining mean and gradient residual stress in thin films using micromachined cantilevers," *Journal of Micromechanics and Microengineering*, vol. **6**, pp. 301–9, 1996.

[110] J. A. Thornton and D. W. Hoffman, "Internal stresses in titanium, nickel, molybdenum, and tantalum films deposited by cylindrical magnetron sputtering," *Journal of Vacuum Science and Technology*, vol. **14** , pp. 164–8, 1977.

[111] A. Taffaf, J. Daleiden, S. Irmer, D. Prasai, and H. Hillmer, "Stress investigation of PECVD dielectric layers for advanced optical MEMS," *Journal of Micromechanics and Microengineering*, vol. **14** , pp. 317–23, 2004.

[112] T. G. Bifano, H. T. Johnson, P. Bierden, and R. K. Mali, "Elimination of stress induced curvature in thin-film structures," *Journal of Microelectromechanical Systems*, vol. **11**, no. 5, pp. 592–7, 2002.

[113] W.-H. Chu and M. Mehregany, "A study of residual stress distribution through the thickness of p+ silicon films," *IEEE Transactions on Electronic devices*, vol. **40**, pp. 1245–50, 1993.

[114] X. Ding, W. H. Ko, and J. M. Mansour, "Residual stress and mechanical properties of boron-doped p+ silicon films," *Sensors and Actuators A*, vol. **21-23**, pp. 866–71, 1990.

[115] L. Kiesewetter, J.-M. Zhang, D. Houdeau, and A. Steckenborn, "Determination of Young's moduli of micromechanical thin films using the resonance method," *Sensors and Actuators A*, vol. **35**, pp. 153–9, 1992.

[116] D. Jung and H. C. Gea, "Toplogy optimization of nonlinear structures," *Finite Elements in Analysis and Design*, vol. **40**, pp. 1417–27, 2004.

[117] R. J. Roak and W. C. Young, *Formulas for Stress and Strain*. New York: McGraw-Hill Inc., 1989.

[118] J. E. Bradby, J. Williams, J. Wong-Leung, M. V. Swain, and P. Munroe, "Mechanical deformation of InP and GaAs by spherical indentation," *Applied Physics Letters*, vol. **78**, no. 21, pp. 3235–7, 2001.

[119] S. Greek, R. Gupta, and K. Hjort, "Mechanical considerations in the design of a micromechanical tuneable InP-based WDM filter," *Journal of Microelectromechanical Systems*, vol. **8**, no. 3, pp. 328–34, 1999.

[120] G. Jacquemod, K. Vuorinen, F. Gaffiot, A. spisser, C. Seassal, J.-L. Leclercq, P. Rojo-Romeo, and P. Viktorovitch, "MOEMS modelling for opto-electro-mechanical co-simulation," *Journal of Modeling and Simulation of Microsystems*, vol. **1**, no. 1, pp. 39–48, 1999.

[121] M. Mehregany, "Overview of micromechanical systems," in *Proceedings of SPIE vol. 1793 - Integrated Optics and Microstructures* (D. L. P. assood Tabib-Azar, ed.), (Boston, MA, USA), pp. 2–11, SPIE, March 1993.

[122] R. P. Feynman, "There's plenty of room at the bottom," *Journal of Microelectromechanical Systems*, vol. **1**, pp. 60–66, 1992.

[123] W. S. N. Trimmer, "Microrobots and micromechanical systems," *Sensors and Actuators*, vol. **19**, pp. 267–287, 1989.

[124] M. Elwenspoek and R. J. Wiegerink, *Mechanical Microsensors*. Berlin, Heidelberg, New York: Springer-Verlag, 2001.

[125] A. W. Leissa, *Vibration of Plates*. Washington, DC: U.S. Government Printing Office (NASA SP -160,1969 reprinted by the Acoustical Society of America, 1993.

[126] S. Timoshenko and S. Woinowsky-Krieger, *Theory of Plates and Shells*. New York, St. Louis, San Francisco, Auckland, Bogota, Caracas, Lisbon, London, Madrid, Mexico City, Milan, Montreal, New Delhi, San Juan, Singapore, Sydney, Tokyo, Toronto: McGraw-Hill Inc., 1987.

[127] J. R. Vinson, *The Behaviour of Thin Walled Structures: Beams, Plates and Shells*. Dordrecht, Boston, London: Kluwer Academic Publishers, 1989.

[128] K. M. Liew, "Response of plates of arbitrary shape subject to static loading," *Journal of Engineering Mechanics*, vol. **118** , no. 9, pp. 1783–94, 1992.

Appendix A

Current internet usage statistics

Region/country	Population (2004 Estimate)	Internet Usage (Sept. 2004)	User Growth (2000-04)(%)	Penetration in pop. (%)
Africa	893,197,200	12,937,100	186.6	1.4
Asia	3,607,499,800	257,898,314	125.6	7.1
Europe	730,894,078	230,886,424	124.0	31.6
Middle East	258,993,600	17,325,900	227.8	6.7
North America	325,246,100	222,165,659	105.5	68.3
Latin America/Caribbean	541,775,800	55,930,974	209.5	10.3
Oceania	32,540,909	15,787,221	107.2	48.5
WORLD TOTAL	6,390,147,487	812,931,592	125.2	12.7
Kenya	33,520,700	400,000	100.0	1.2
Germany	82,633,200	47,182,628	96.6	57.1

Table A.1: Current (September 2004) internet usage statistics in all world regions and in Kenya and Germany [1].

Appendix B

FSR derivation

The following derivation follows from Eqn. (2.9) where FSR is derived as a frequency range. The alternative is in terms of wavelength range as shown here.

$$\hat{\delta} = \frac{2\pi}{\lambda} nL \cos\theta$$

$$\hat{\delta}_m = \frac{2\pi}{\lambda_m} nL \cos\theta$$
$$= m\pi$$
$$\hat{\delta}_{m+1} = m\frac{2\pi}{\lambda_{m+1}} nL \cos\theta$$
$$= (m+1)\pi$$

$$\hat{\delta}_{m+1} - \hat{\delta}_m = \pi = 2\pi nL \cos\theta \left(\frac{1}{\lambda_{m+1}} - \frac{1}{\lambda_m} \right)$$

$$1 = 2 nL \cos\theta \left(\frac{1}{\lambda - \Delta\lambda} - \frac{1}{\lambda + \Delta\lambda} \right)$$
$$1 = 2 nL \cos\theta \left(\frac{2\Delta\lambda}{\lambda^2 - (\Delta\lambda)^2} \right)$$

$$FSR = 2\Delta\lambda \qquad \text{when } \Delta\lambda \ll \lambda$$

$$= \left(\frac{\lambda^2}{2\pi nL \cos\theta} \right)$$

$$\text{where } \lambda = \frac{\lambda_{m+1} + \lambda_m}{2}$$

Appendix C

Comparison with model of higher self-consistency

This appendix seeks to further justify the electro-mechanical coupling used in the models presented in the preceding chapters and to demonstrate that the error resulting from the assumptions made do not result in any significant loss in accuracy. Presented in the following is a 2D fully coupled self-consistent electrostatic-structural-mechanics model. The multiphysics coupling between the electrostatic and structural mechanics in the FEM software used is a fairly straightforward matter. However, for the cases considered in this work, there is a big challenge in this implementation in the form of the non-linear nature of the coupling whereby the state of the prevailing deformation of the structures determine the next deformation state, until an equilibrium of forces is achieved. This challenge is overcome using a method summarised in the algorithm shown in Fig. C.1. The method involves solving for the electric field in the environment surrounding the membranes, the electrostatic forces acting on the boundaries of the structure are then in turn calculated from the field distribution. The resulting forces cause deformation in the structure. This is determined by the structural mechanics part of the algorithm. The deformation is then compared with a given tolerance which determines whether or not to stop the iteration in the calculation. Alternatively, a number of predetermined calculation loops are performed. If the tolerance or the maximum number of steps is not yet achieved, a new structure is calculated from the present deformed mesh and the series of calculations repeated. To illustrate this, the simple structure in the diagram of Fig. C.2 is used in a 2D calculation.
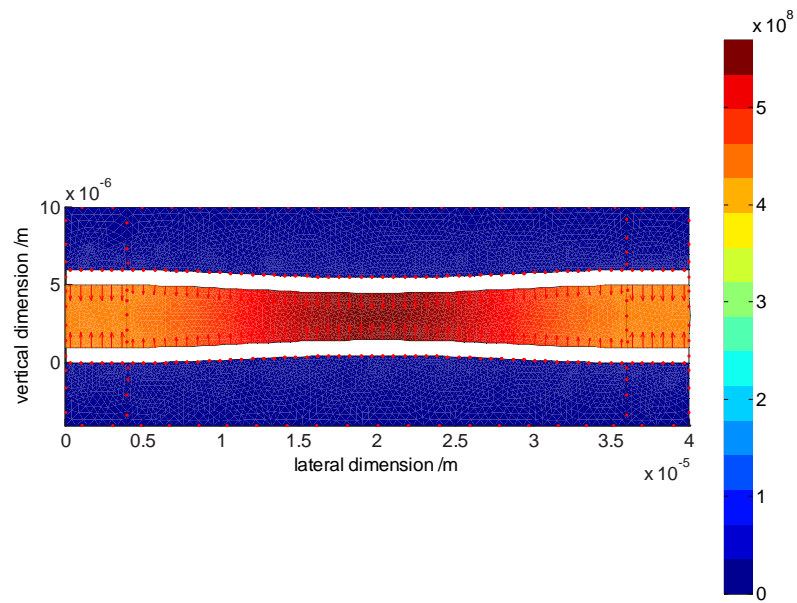
Figure C.3 shows the output of the electrostatic part of the self-consistent model show-

139
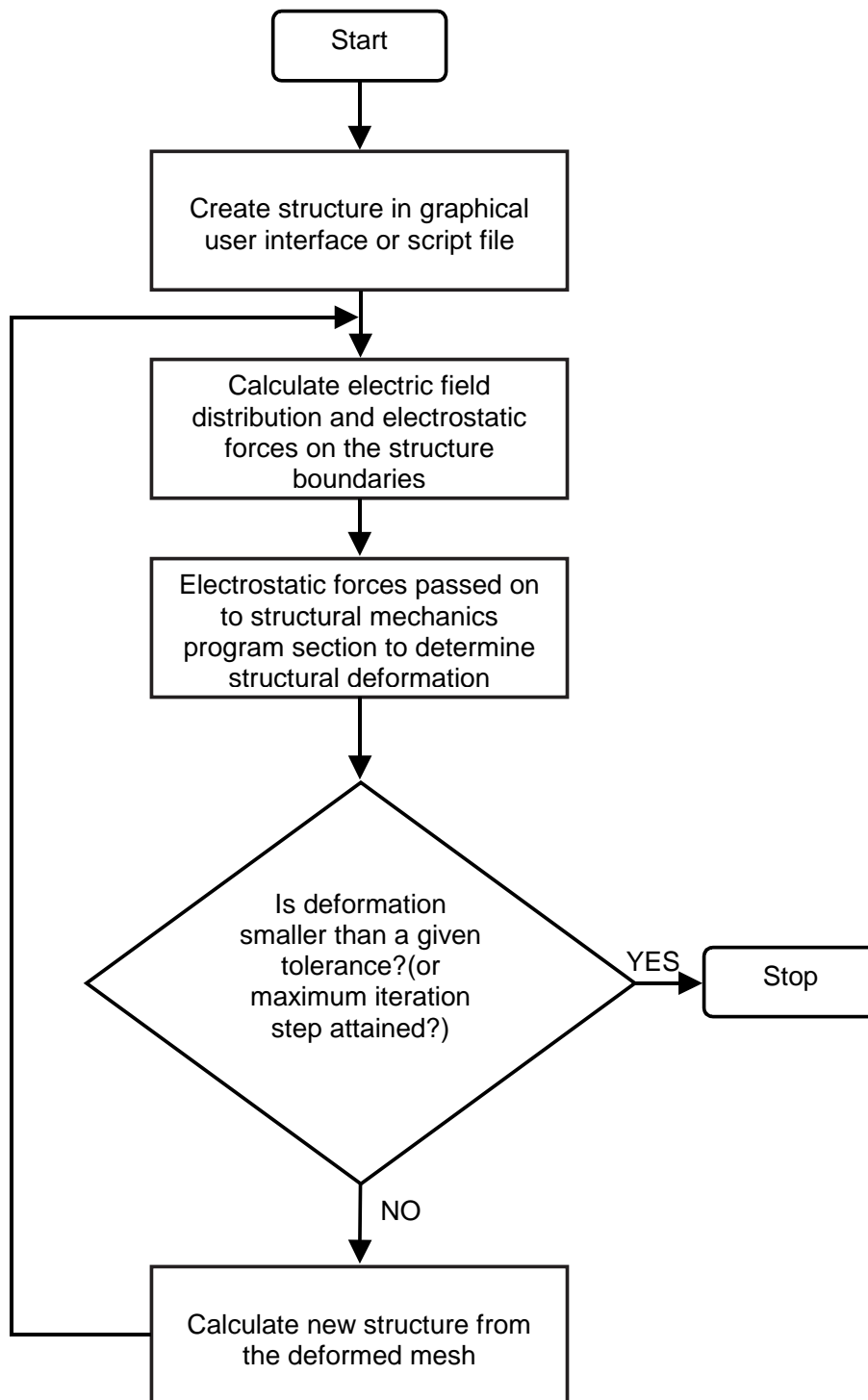
Fig. C.1: Flow diagram of the fully-coupled self-consistent electrostatic-structural-mechanics FEM algorithm.
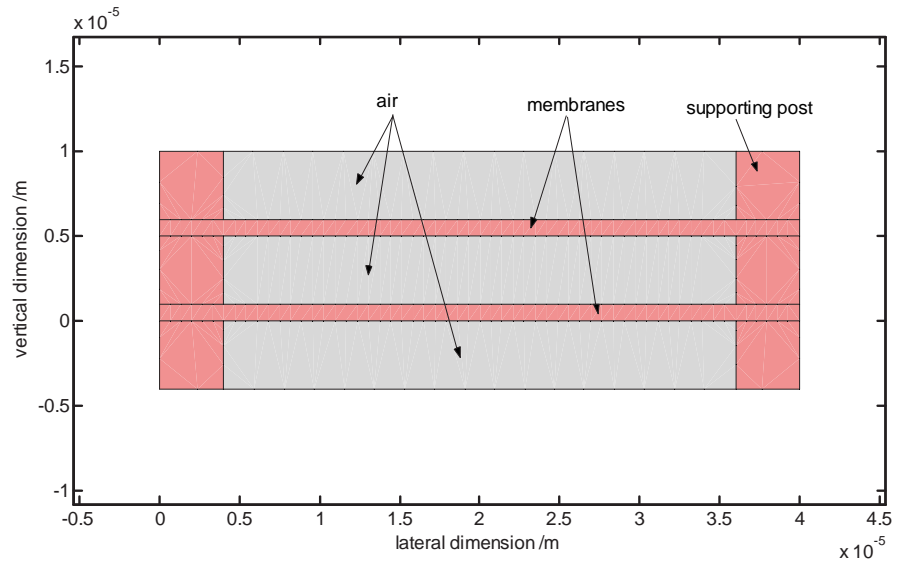
Fig. C.2: Cross-sectional view of the analysed structure with two membranes separated from each other by a small gap.

Fig. C.3: Electric field distribution in the environment of the analysed structure when a potential difference is applied between the membranes.

ing the electric field distribution in the environment of the structure of Fig. C.2. The
governing equation for the electrostatic problem is given by
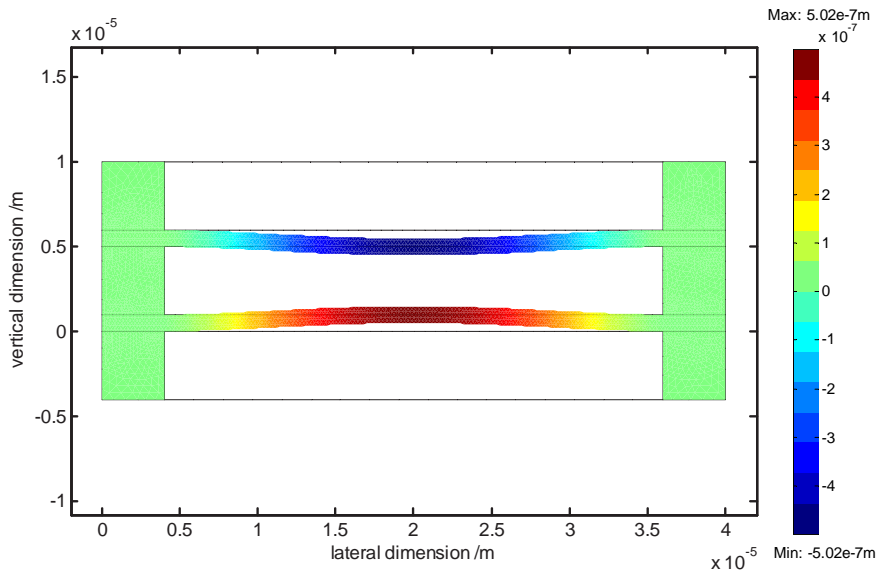
$$-\nabla \cdot (\varepsilon \nabla V) = 0. \tag{C.1}$$

Two types of boundary conditions are defined, the insulation-symmetry defined according
to

$$-\bar{\mathbf{n}} \cdot (\varepsilon \nabla V) = 0 \tag{C.2}$$

and constant potential on boundary, $V = V_0$.

Finally, the force density at the boundaries of the structure is then determined from the
following;

$$f_{es} = \varepsilon \frac{(\nabla V)^2}{2}. \tag{C.3}$$

Fig. C.4: Structural deformation resulting from the applied potential difference between the mem-
branes.

In Fig. C.4 is the corresponding structural mechanics output of the model. Here
the deformation of the membranes resulting from the electrostatic forces is seen. The
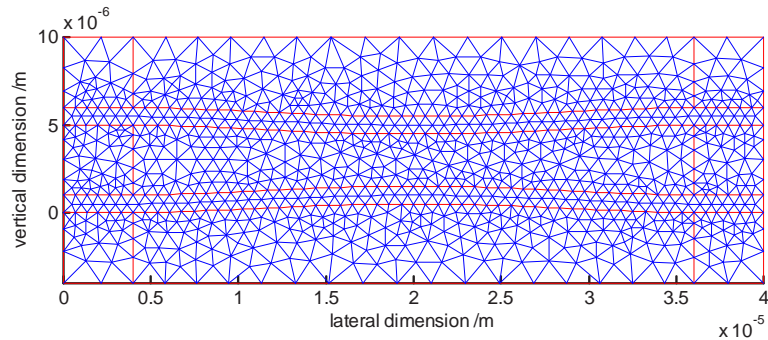
Fig. C.5: Deformed mesh of the analysed structure from which the program generates a new deformed structure for further iterations.

resulting deformed mesh is shown in Fig. C.5.

The governing equation for the structural mechanics part is given by Eqn. 3.10 for the plane stress 2D case. Two types of boundary conditions are used, fixed for the non-moving reference boundaries, and loads on boundaries defined by the electrostatic forces acting in normal direction on the boundaries.

The plot of Fig. C.6 shows the maximum deflection of the top membrane versus the iteration steps. As the number of iterations increase the deflection settles to an equilibrium value.

Figure C.7 portrays the results of the same structure subjected to the simplified electromechanical model defined in the last section.

Comparing the results of maximum deflection obtained from the two methods (4.98e-7 m and 5.02e-7 m), it is quickly verified that the difference is less than 1 %. For the fully coupled self-consistent model of the simple 2D example presented here, a far more intricate implementation compared to the short-cut method is required. Trading off this almost negligible error for the simplicity of the model used in this work is in deed a justifiable price to pay.
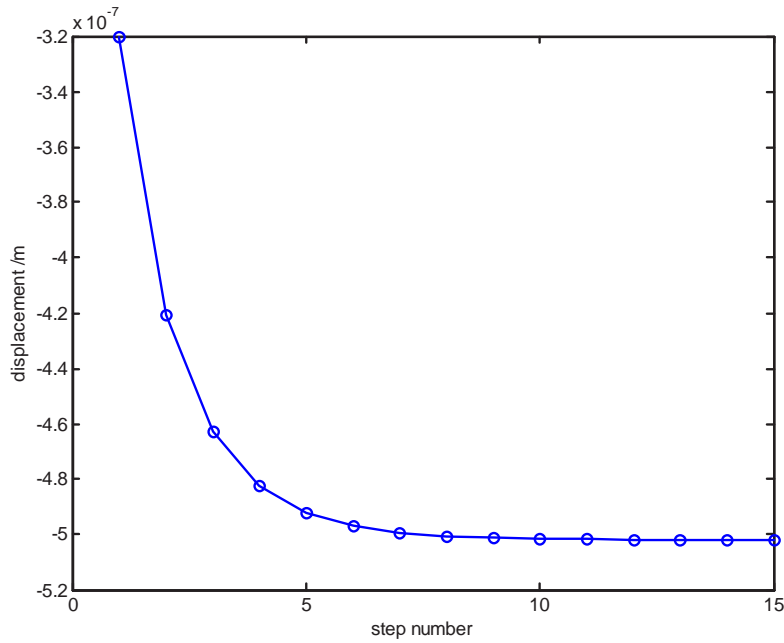
Fig. C.6: Plot of maximum deflection of top membrane seen converging to an equilibrium value as the iteration steps increase.
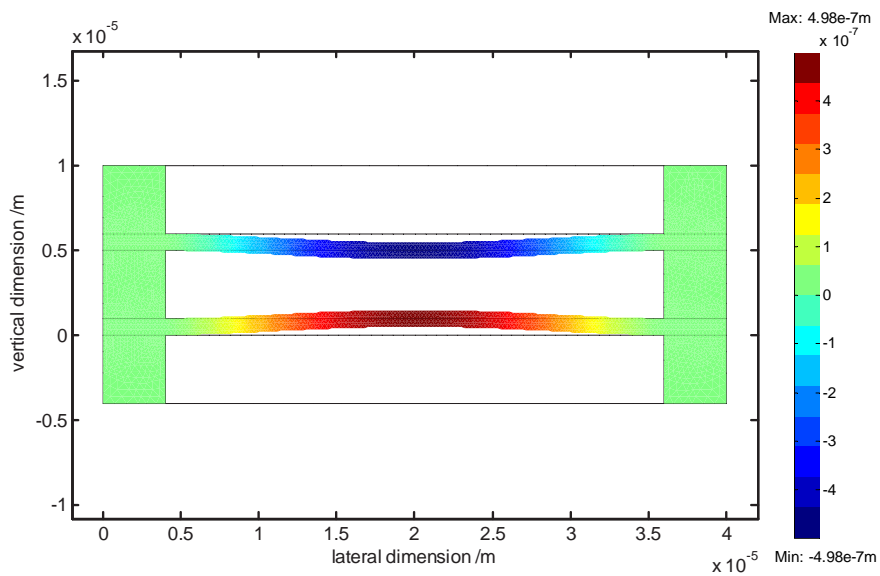
Fig. C.7: Structural deformation resulting from the applied potential difference between the membranes of the analysed structure using the simpler method applied in this dissertation.